

ANALYSIS OF LIGHTWEIGHT GASES BY
QUADRUPOLE ION TRAP MASS SPECTROMETERY
FOR THE SAFETY OF THE AMERICAN
SPACE SHUTTLE PROGRAM

By

ANDREW KEITH OTTENS

A DISSERTATION PRESENTED TO THE GRADUATE SCHOOL
OF THE UNIVERSITY OF FLORIDA IN PARTIAL FULFILLMENT
OF THE REQUIREMENTS FOR THE DEGREE OF
DOCTOR OF PHILOSOPHY

UNIVERSITY OF FLORIDA

2003

To Tamara, to my parents, and to my brother for always providing love and support.

ACKNOWLEDGMENTS

I express my utmost thanks to my parents, Paul and Ann Ottens, for supporting me through all that I have done – always remember their advise to stay in school as long as I can, and to stand back-up whenever life knocks me down. I thank my brother Richard whose dedicated interest in NASA inspired my research. I thank my entire family for their continued love and support.

I sincerely thank my fiancée Tamara Blagojević for her dedicated support and help in writing this document. Her unconditional love brightens my life. For all the little things that seemingly went unnoticed, I am forever grateful.

Special thanks go to my good friends Kevin McHale and Josh Coon. Kevin's open kindness to me as a stranger helped bring me to the University of Florida. He was always available to lend a hand or to debate a topic; I too will remember the pint-o-Killians talks. Josh's friendship made the laboratory bearable, despite the awful noise of his ever-expanding mass spectrometer. From countless lunch runs to exhaustive conversations, his comradeship kept me on track. I also acknowledge my past and present group members for their support over the years.

I express my gratitude to Drs. Richard A. Yost, David H. Powell, and Jodie V. Johnson who have been helpful in their understanding of mass spectrometry throughout the years. I also thank the staff of the business office, the electronics shop, the IT shop, and the machine shop. These people make the chemistry department run. I give special

thanks to Steve Miles who on many occasions dropped what he was doing to help me resolve complex electronics issues

At the Kennedy Space Center, I sincerely thank Drs. Timothy P. Griffin and C. Richard Arkin for their professional support and friendship. Tim was my mentor through much of my graduate school career – to him I am utterly grateful. Richard as a fellow chemist brought a sense of sanity to the engineering world of the space center. Tim and Richard are truly great people.

I would also like to thank the people of Dynacs Engineering for their support of my research: specifically, Guy Naylor, Bill Haskell, Charles Curly, and David Floyd of the HGDL lab were an immense help during my time at the space center. I wish to acknowledge those from NASA (William R. Helms, Fredric W. Adams, and Duke W. Follistein) who helped provide project support and make my KSC experience enjoyable.

Many thanks go to Scott Quarmby and Brody Guckenberger of ThermoFinnigan who have been immensely helpful with technical issues and in contributing hardware, software, and documentation for the QITMS instrumentation used in this research.

Finally, I extend my sincere gratitude to my research advisor Dr. W. W. Harrison, who despite our late introduction was an immense help in the successful completion of my doctoral studies. He has served as a steady guide, and as a role model with his professional prowess.

TABLE OF CONTENTS

	<u>page</u>
ACKNOWLEDGMENTS	iii
LIST OF TABLES	ix
LIST OF FIGURES	xi
ABSTRACT	xvi
 CHAPTER	
1 INTRODUCTION	1
Theory of Ion Motion within Quadrupole Devices.....	2
Quadrupole Electric Field	2
Ion Motion in Quadrupole Devices.....	3
Deriving the Mathieu Equation.....	7
Stability Diagram	10
Pseudopotential Well Theory.....	18
Modes of Quadrupole Ion Trap Operation.....	22
Mass-Selective Detection.....	23
Mass-Selective Storage	25
Mass-Selective Ejection	27
Collision Gas.....	28
Multi-Purpose Auxiliary Waveforms.....	28
Overview of Dissertation	31
 2 MONITORING LIGHTWEIGHT GASES FOR SPACE SHUTTLE SAFETY	 32
Introduction.....	32
Present Day Gas Detection.....	35
Advanced Hazardous Gas Detection Project	38
AHGD Leak Detection System Requirements.....	38
Experimental Methodology and Equipment	40
AHGD Test Procedure	40
Analytical Procedures	44
Two-point calibration.....	44
Calculated detection limit	44
Accuracy of quantification.....	44
Precision of quantification	45

Response time	45
Recovery time	45
Gas Delivery Assembly.....	45
Evaluated Mass Analyzers	47
Linear quadrupole	47
Quadrupole array	48
Time-of-flight	48
Cycloidal focus	49
Results of the Examination	49
Detection Limits.....	50
Accuracy	55
Precision.....	57
Response and Recovery Time.....	57
Conclusions and Consideration for Future Work	57
 3. LIGHTWEIGHT GAS MONITORING BY QITMS	 65
Introduction.....	65
History of QIT with Hydrogen and Helium Ions.....	65
Modern QITMS.....	66
Instrumentation and Equipment for Lightweight Mass Analysis	69
University of Florida Custom QITMS (UF-IT)	69
Mass analyzer, source, and optics.....	69
Vacuum system.....	71
Control, source, optics, detector, and acquisition electronics.....	76
Drive circuitry.....	80
Chassis and power supplies	84
Customized software.....	84
Commercial QITMS (PolarisQ).....	85
Hardware differences between QITMS systems.....	85
Drive circuitry.....	89
Custom Software.....	94
Tuning the RF Circuit	96
Gas Dilution System (GDS).....	99
Instrument Development Discussion	101
GDS Evaluation	101
Results of UF-IT Assembly	106
Changing the drive frequency.....	109
Pump difficulty with hydrogen	114
Exploring the PolarisQ.....	116
Collision gas and external ionization.....	116
Injection waveforms.....	118
Resonant ejection	121
PolarisQ modified for lightweight gas analysis	123
Detecting hydrogen ions with the PolarisQ	123
Conclusions.....	125

4 ION-MOLECULE REACTIONS: A LIMITATION OF QITMS	128
Introduction.....	128
Types of Ion-Molecule Reactions	129
Charge-exchange reactions	130
Proton transfer reactions	130
Hydrogen-atom transfer	132
Kinetics of Ion-Molecule Reactions.....	132
Thermodynamics of Ion-Molecule Reactions	135
Equipment and Methods	136
Gas Delivery Setup	136
Number Density Determination	137
Custom Scan Functions.....	139
Ion-Molecule Reaction Results.....	143
He ⁺ Reactions	143
H ₂ ⁺ Self-Protonation and Other Reactions	151
N ₂ ⁺ Reacting with H ₂ O	155
Ar ⁺ Reactions.....	157
Thermodynamics of O ₂ ⁺ and H ₃ O ⁺	158
Conclusions.....	161
5 OPTIMIZING QITMS FOR LIGHTWEIGHT GAS ANALYSIS	164
Introduction.....	164
Conditions for Ionization	164
Electron energy	164
Time and pressure	165
Low-mass cutoff	165
Space charge effects.....	167
Ion Storage in the QIT.....	168
Ion Ejection from the QIT	168
Ejection by nonlinear resonance	169
Mass resolution controlled by ejection rate	174
Specialized scan routines	174
Experimental Details.....	175
Sample Gas	175
Instrumentation	176
Software	176
Results and Discussion of QITMS Optimization.....	177
Ionization of the QITMS	177
Electron optics	177
Ion trap pressure versus ionization time	178
The optimal q_z for ionization	183
Intermediary Scan Function Activity	186
Ion Ejection and Acquisition.....	188
Post scan activity.....	190
Nonlinear resonance.....	190

High-resolution	194
Conclusions.....	198
6 PERFORMANCE EVALUATION OF QITMS	202
Introduction.....	202
Experimental	203
Analytical Methodology.....	203
Sample Delivery.....	204
Instrumentation	206
Results and Discussion of QITMS Performance	206
Custom Built QITMS.....	207
Modified Commercial QITMS.....	208
Performance Comparison.....	211
Conclusions.....	218
7 CONCLUSIONS AND FUTURE DIRECTIONS	220
APPENDIX	
A CODE FOR MASS CALIBRATION	229
B CODE FOR REAL-TIME DATA PLOT.....	232
C CODE FOR POLARISQ AHGD SCAN	235
D CODE FOR AHGD OPTIMIZED UF-IT SCAN MATRIX	244
E LIST OF ACRONYMS AND ABBREVIATIONS	250
LIST OF REFERENCES.....	253
BIOGRAPHICAL SKETCH.....	264

LIST OF TABLES

<u>Table</u>	<u>page</u>
2-1. The AHGD project analytical performance requirements.....	39
2-2. The AHGD project system specifications.....	39
2-3. Linear quadrupole analytical performance	50
2-4. Quadrupole array analytical performance.....	50
2-5. Time-of-flight analytical performance.....	50
2.6. Cycloidal focus analytical performance.....	50
3-1. Change in peak width with and without using resonant ejection.....	123
4-1. Recombination energies (RE) for ions of interest.....	131
4-2. Ionization energies (IE) for atoms and molecules of interest	131
4-3. Proton affinities for molecules of interest.....	131
4-4. Correction factors for partial pressure measurements	139
4-5. Repetitive ion-molecule reaction experiments between He^+ and N_2	146
4-6. Ion-molecule reactions at different He pressures between He^+ and N_2	150
4-7. Ion-molecule reaction at different N_2 pressures between He^+ and N_2	150
4-8. Ion-molecule reaction with reversed gas lines between He^+ and N_2	151
4-9. Self-protonation reaction results for hydrogen	154
4-10. Hydrogen ion-molecule reaction at different N_2 pressures.....	155
4-11. Determination of water vapor pressure via reaction with N_2^+	157
4-12. Ion-molecule reaction between argon ions and water.....	158
5-1. Observed nonlinear resonance ejection using a slow scanrate	195

6-1.	Custom built (UF-IT) QITMS analytical performance.....	208
6-2.	Modified commercial (PolarisQ) QITMS analytical performance.....	210

LIST OF FIGURES

<u>Figure</u>	<u>page</u>
1-1. Electrode arrangement for a linear quadrupole.....	4
1-2. Cross-sectional view of a QIT	5
1-3. Mathieu stability diagram in one dimension.....	11
1-4. Linear quadrupole stability diagrams.....	13
1-5. Quadrupole ion trap stability diagrams.....	14
1-6. Ion motion within quadrupole ion trap depicted in two and three dimensions.....	17
1-7. Parabolic pseudopotential wells in the r and z dimensions.....	20
1-8. Plot of ion motion relative to the RF phase angle.....	21
1-9. Mass-selective detection methods used for in-situ detection.....	24
1-10. Plot of a basic QITMS scan function.....	29
2-1. The fully assembled Space Shuttle (Atlantis).....	33
2-2. Space Shuttle main engines (SSMEs).....	34
2-3. Hazardous gas detection system (HGDS).....	36
2-4. Map of transport lines used for delivering sampled gas to the HGDS	37
2-5. Stanford Research System model RGA-100 linear quadrupole mass analyzer	41
2-6. Ferran Scientific model POD-01 quadrupole array mass spectrometer.....	41
2-7. IonWerks time-of-flight mass spectrometer	42
2-8. Monitor Group MG2100 cycloidal focus mass spectrometer.....	43
2-9. The AHGD gas delivery system	46
2-10. Detection limits for the evaluated mass spectrometers.....	52

2-11. Update Rates for four evaluated mass spectrometers	53
2-12. Quadrupole array data.....	54
2-13. Accuracy of the four evaluated mass spectrometers.....	56
2-14. Precision of the four evaluated mass spectrometers	58
2-15. Response time of the four evaluated mass spectrometers.....	59
2-16. Recovery time of the four evaluated mass spectrometers.....	60
2-17. TOF data	61
2-18. Ferran Scientific miniature quadrupole array	64
3-1. Location of hydrogen and helium ions on the stability diagram	67
3-2. The ion trap assembly of a Finnigan ITS-40 used in the UF-IT	70
3-3. Electron optics of an ITS-40 used on the UF-IT.....	72
3-4. Open-configuration on the UF-IT ion trap.....	73
3-5. The vacuum manifold, turbo-drag pump and chassis of the UF-IT	74
3-6. The UF-IT transfer line.....	75
3-7. Backing pumps used with the UF-IT	77
3-8. The main system board (MSB) of the UF-IT.....	78
3-9. The electrometer board, RF control board, and RF amplifier of the UF-IT	79
3-10. The RF drive circuit diagram of the UF-IT	81
3-11. RF coils used on the UF-IT.....	82
3-12. Power supplies of the UF-IT	83
3-13. UF-IT mass calibration software	86
3-14. New UF-IT real-time graphical display	87
3-15. PolarisQ external ion source and ion trap assembly	88
3-16. The new RF coil of the PolarisQ.....	90
3-17. The low-pass filter board (LPF) board of the PolarisQ	92

3-18.	The RF amplifier of the PolarisQ.....	93
3-19.	The AHGD scan software written for the PolarisQ.....	95
3-20.	Method for determining the resonant frequency of an RLC network.....	98
3-21.	Devised gas mixing and delivery system (GDS).....	100
3-22.	Gas Dilution System (GDS) control software	102
3-23.	The experiment schedule function of the GDS software	103
3-24.	Performance comparison of the NASA discrete bottle method and the Gas Dilution System (GDS).....	105
3-25.	First UF-IT mass spectrum taken of room air.....	107
3-26.	The use of a collision gas with the UF-IT.....	108
3-27.	UF-IT ion signal improvement after regulating the emission current	111
3-28.	Mass Spectrum of 1.25% each analyte in nitrogen acquired on the UF-IT at a drive frequency of 2.76 MHz.....	113
3-29.	Difficulty with pumping hydrogen	115
3-30.	Removing the collision gas from the PolarisQ	117
3-31.	Oscilloscope plots of electrometer signal (red) as the RF amplitude was ramped (blue) during mass analysis.....	119
3-32.	Effect of injection waveforms on analyte ion signals.....	120
3-33.	Mass spectra illustrating the effects of using resonant ejection.....	122
3-34.	Mass spectra with the PolarisQ tuned to 2.82 MHz.....	124
3-35.	Hydrogen as the collision gas in the PolarisQ at 2.82MHz.....	126
3-36.	Use of a hydrogen collision gas when monitoring the AHGD-analyte ions while changing from pure nitrogen to 5000-ppm of each in nitrogen	127
4-1.	Diagram of the UF-IT vacuum chamber.....	138
4-2.	Nitrogen correction factor plot.....	140
4-3.	Hydrogen correction factor plots	141
4-4.	Argon correction factor plot.....	142

4-5.	QITMS scan functions for low-mass ions	144
4-6.	QITMS scan function for higher mass ions	145
4-7.	Ion intensities versus reaction time for reaction of He^{++} and background gases	147
4-8.	Plot of the change in helium ion signal versus reaction time	148
4-9.	Ion intensity versus reaction time for self-protonation reaction of H_2	152
4-10.	Plot of the change in hydrogen ion signal versus reaction time	153
4-11.	Five plots of the change in hydrogen ion signal versus reaction time	156
4-12.	Ion intensities versus reaction time for reaction of Ar^{++} with background gas	159
4-13.	Plot of the change in argon ion signal versus reaction time	160
4-14.	Monitored ion signals of background gases.....	162
5-1.	Distribution of electron energies of an internal ionization QITMS	166
5-2.	Lines of nonlinear resonance within the stability diagram	170
5-3.	Three-dimensional representation of black canyons.....	172
5-4.	Distortion of the pseudo-potential well caused by a +4% octopole field	173
5-5.	Hydrogen ion signal response with changing ionization conditions	179
5-6.	Helium ion signal response with changing ionization conditions	180
5-7.	Oxygen ion signal response with changing ionization conditions.....	181
5-8.	Argon ion signal response with changing ionization conditions	182
5-9.	Plot of H_2^{++} and He^{++} ion signals versus RF amplitude during ionization.	184
5-10.	Plot of O_2^{++} and Ar^{++} ion signals versus RF amplitude during ionization.....	185
5-11.	Oscilloscope display of post-ionization activity	187
5-12.	Oscilloscope display of H_2^{++} and He^{++} ion peaks using different scan rates	189
5-13.	Oscilloscope display of delayed acquisition.....	191
5-14.	Mass spectrum taken of pure nitrogen at a scan rate of 0.06 ms/Da	192
5-15.	Mass spectrum taken while sampling pure nitrogen at a scan rate of 1 ms/Da	193

5-16.	Mass spectra of the isobars, nitrogen and ethylene.....	197
5-17.	Optimized UF-IT scan function.....	199
5-18.	Optimized PolarisQ scan function	201
6-1.	Revised diagram of gas dilution system (GDS).....	205
6-2.	Plot of UF-IT response over the concentration range from 0 to 25,000 ppm (2.5%) for each AHGD analyte in nitrogen	209
6-3.	Plot of detection limits for six mass analyzers.....	212
6-4.	Plot of quantification error for six mass analyzers	213
6-5.	Plot of precision for six mass analyzers.....	214
6-6.	Plot of response times for six mass analyzers.....	215
6-7.	Plot of recovery times for six mass analyzers.....	216
6-8.	Plot of the update periods for six mass analyzers	217
6-9.	Plot of high-mass cutoffs for six mass analyzers.....	219
7-1.	Plot of system volume for six mass spectrometer systems	224
7-2.	Plot of system weight for six mass spectrometer systems	225
7-3.	Sectioned image of the UF-IT QITMS instrument	227

Abstract of Dissertation Presented to the Graduate School
of the University of Florida in Partial Fulfillment of the
Requirements for the Degree of Doctor of Philosophy

ANALYSIS OF LIGHTWEIGHT GASES BY
QUADRUPOLE ION TRAP MASS SPECTROMETRY
FOR THE SAFETY OF THE AMERICAN
SPACE SHUTTLE PROGRAM

By

Andrew Keith Ottens

May 2003

Chair: Dr. W. W. Harrison
Department: Chemistry

The quadrupole ion trap mass spectrometer (QITMS) was patented nearly 50 years ago, when it was proposed for trace analysis of lightweight gas mixtures. Though a commercial success, QITMS has been used with analytes of ever-increasing size. We evaluated QITMS for quantifying lightweight gas mixtures with the performance compared to other mass analyzer technologies.

The National Aeronautics and Space Administration (NASA) uses mass spectrometers to monitor the amount of hydrogen, helium, oxygen, and argon in the nitrogen-purged Space Shuttle. The explosive hazard of the cryogenic hydrogen and oxygen used to propel the Space Shuttle makes leak detection imperative. The two present-day leak detectors are remotely located because of their large size and sensitivity to vibration. Analysis is delayed by up to 45 s, and only two samples can be monitored simultaneously. In 2000, NASA initiated the Advanced Hazardous Gas Detection project

to develop a compact, rugged, and fast mass spectrometer to be placed in multiple locations next to the Space Shuttle to provide real-time analysis with increased redundancy.

The QITMS instrumentation was modified specifically for this application. The RF drive frequency was increased to 2.5 MHz to adequately trap lightweight hydrogen and helium ions. Internal ionization was preferred for use without a collision gas, along with an open source configuration that provided rapid sample replacement. The modern electronics incorporated were controlled by customized software.

Analytes were found to react rapidly with abundant background gases. The QITMS operating conditions were optimized to minimize negative effects of ion-molecule reactions while maximizing analytical performance. A custom segmented scan function was developed with a total scan time of 14 ms, averaging 70 scans per data point at the required 1 Hz update rate.

The QITMS met requirements for detection limits, accuracy, precision, response time, and recovery time. The linear quadrupole was the only other instrument to perform similarly, but was six times slower than the QITMS. Thus, QITMS was the preferred analyzer technology for the application, which NASA will further develop to improve the safety of Space Shuttle program for years to come.

CHAPTER I INTRODUCTION

Wolfgang Paul introduced the quadrupole ion trap (QIT) in 1953,¹ but he did not know then that the device, later to be named after him, would become a great achievement in mass spectrometry.^{2,3} In the same patent, Paul introduced the linear quadrupole, which also became a leading choice of mass spectrometrists.⁴ Both are quadrupole devices; essentially, the QIT is a 360° rotation of a linear quadrupole forming a central ring flanked by two endcaps.⁵ Both devices operate by manipulating ion motion in a periodic electric field. Despite their similarities, the two devices have evolved along entirely different paths, which has led to a divergence in the applications they are used for.³⁻⁷ The linear quadrupole was quickly adopted as a compact, simple, mass analyzer used for trace analysis of gas mixtures – a residual gas analyzer (RGA).⁴ In contrast, for three decades the QIT remained a relatively unknown device because of its poor performance as a mass spectrometer.^{6,7}

This changed in 1983 with the introduction of the Ion Trap Detector (ITD[®]) by Finnigan MAT Corporation (San Jose, CA). Commercial success was made possible with the use of a new mass analysis method (mass-selective ejection) that was further enhanced using a helium collision gas.^{8,9} Finnigan marketed the ITD as a simple, inexpensive detector for gas chromatographs (GC), beginning nearly 20 years of innovation by numerous manufacturers.

Today's quadrupole ion trap mass spectrometer (QITMS), coupled with chromatography, can analyze complex mixtures, with femtomole detection limits and a

10^6 dynamic range. It has become widely used in biological, pharmaceutical, and environmental industries,^{2,3} with a focus on high-mass analytes. With the success in these areas, little attention has been paid to Paul's intended use of the QIT as a tool for trace analysis of lightweight gases¹⁰ – the focus of our study.

This chapter provides a background of QITMS fundamentals, operation, and history. The theory of ion motion in a quadrupole field is discussed in some detail, because of its importance for understanding the instrumental modification and results of this work. Most equations are provided in a general context to explain behavior inside a quadrupole device, thus units are provided only for essential terms used in calculations, and the reader is referred to the literature for further explanation. The three modes of QITMS operation are reviewed in historical order. The advantages of the mode selected for this research are emphasized in contrast to the other two modes. Mentioned next are recent advances in QITMS technology, some of which are evaluated in later chapters for possible performance enhancements. The chapter concludes with an overview of the dissertation.

Theory of Ion Motion within Quadrupole Devices

Quadrupole Electric Field

A mass spectrometer uses electric and/or magnetic fields to influence an ion's trajectory in such a way as to distinguish its mass-to-charge (m/z) ratio.¹¹ The electric field in an ideal quadrupole device will have a potential, ϕ , that is a quadratic function relative to the Cartesian coordinates x , y , z as in the equation:

$$\phi_{(x,y,z)} = \alpha x^2 + \beta y^2 - \gamma z^2 \quad (1-1)$$

where α , β , and γ are multiplicative constants.^{7,10,12-14} The potential is applied to the electrodes of the device, four rods in a two dimensional array for the linear quadrupole (Figure 1-1), and a three dimensional configuration of a ring with two endcaps for the QIT (Figure 1-2). The emanating electric fields are geometrically related by the constants α , β , and γ . For both devices Laplace's equation must be satisfied, $\nabla^2\phi = 0$. This condition requires that $\alpha + \beta + \gamma = 0$. For the linear quadrupole $\gamma = 0$, since there is no field in the z direction. This requires then for $\alpha = 1$ that $\beta = -1$ to give $\alpha + \beta = 0$. Thus, the potential ϕ is applied to the x-set of rods, while $-\phi$ is applied to the y-set of rods (Figure 1-1). Ions entering the device are confined in the x and y directions by opposing fields and travel lengthwise along the unconfined axial dimension. This differs from the QIT that has an effective field along all three axes. The fields in the x and y directions are identical in the 3D structure of the QIT, thus for $\alpha = 1$ then $\beta = 1$, and to satisfy Laplace's equation, $\gamma = -2$. This was originally accomplished by applying $+\phi$ to the ring and $-\phi$ to the two endcaps (a factor of -2 when taken together). More recently it was found to be easier to ground the endcaps and apply the potential ϕ to the ring. This has the effect of halving the field strength, thus an ion at the center of the trap experiences $+\phi/2$ from the ring while each endcaps appears as $-\phi/2$ (the one-half factor is later accounted for in the equations of ion motion). In the QIT, fields in three dimensions confine ion motion, trapping ions for as long as necessary.

Ion Motion in Quadrupole Devices

The influence of a quadrupole electric field on an ion's motion can be expressed mathematically, derived from the applied potential equation:

$$\phi(\rho, \theta, \phi) = \sum_{n=0}^{\infty} A_n \rho^n P_n(\cos \theta) \quad (1-2)$$

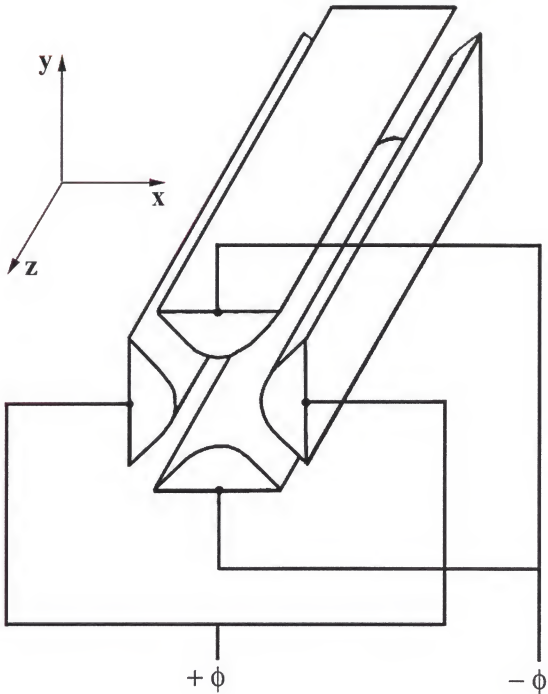


Figure 1-1. Electrode arrangement for a linear quadrupole. Four hyperbolic rods are arrayed in the x - y plane. An inscribed circle of radius r_0 describes the rod spacing. Potentials $+\phi$ and $-\phi$ are applied to alternate rod pairs. (Adapted from Ghosh, P. K. *Ion Traps*; Oxford University: New York, 1995; Figure 2-1, p. 8.)

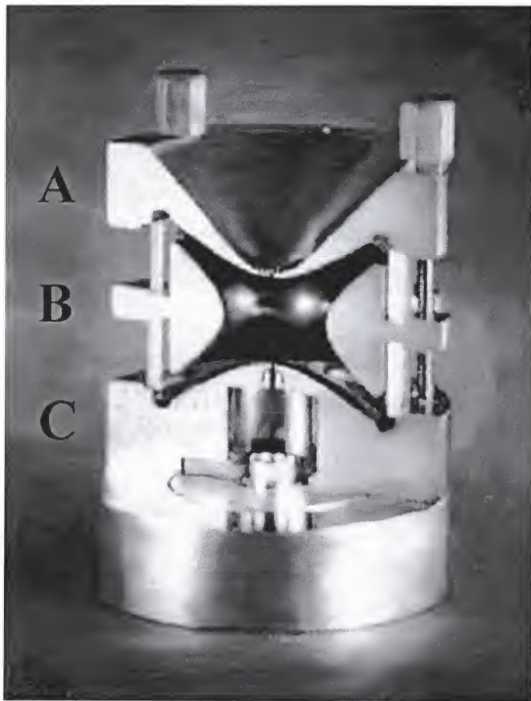


Figure 1-2. Cross-sectional view of a QIT: a) the exit endcap – allows ions to exit and strike a detector; b) the ring electrode – together with the endcaps, it defines the volume and field within which ions are trapped; c) the entrance endcap – allows either electrons or ions to enter the QIT. (Adapted from March, R. E. in Encyclopedia of Analytical Chemistry; Meyers, R. A., Ed.; John Wiley & Sons: Chichester, UK, 2000; Vol 13; Figure 2-9, p. 11850.)

which is expressed differentially here using Laplace's equation in spherical polar coordinates, where A_n^0 are arbitrary coefficients and $P_n(\cos\theta)$ are Legendre polynomials.¹⁴ Equation 1-2 can be expanded and rewritten in Cartesian coordinates as

$$\varphi_{(r,z)} = A_0^0 + A_1^0 z + A_2^0 \left(\frac{1}{2} r^2 - z^2\right) + A_3^0 z \left(\frac{3}{2} r^2 - z^2\right) + \dots \quad (1-3)$$

where $r = \sqrt{x^2 + y^2}$. The parts $n = 0, 1, 2, 3, \dots$ represent discrete components of the field (monopole, dipole, quadrupole, hexapole, etc.), but in the ideal quadrupole device, only monopole and quadrupole components are present, which is assumed hereafter.

Assigning the coefficients $A_0^0 = B$ and $A_2^0 = 2A$, Equation 1-3 becomes

$$\varphi_{(r,z)} = A(r^2 - 2z^2) + B \quad (1-4)$$

which can be used to determine A and B. This is accomplished using the boundary conditions $\varphi_0^E = 0$ at the grounded endcaps, and $\varphi_0^R = \varphi_0$ at the ring electrode. The radial boundary potential at the edge of the ring electrode ($r_0, 0$) is

$$\varphi_{(r_0,0)} = A(r_0^2) + B = \varphi_0 \quad (1-5)$$

and the axial boundary potential at the edge of the endcaps ($0, z_0$) is

$$\varphi_{(0,z_0)} = A(-2z_0^2) + B = 0 \quad (1-6)$$

thus the values for A and B are

$$A = \left(\frac{\varphi_0}{r_0^2 + 2z_0^2} \right) \quad B = \left(\frac{2z_0^2 \varphi_0}{r_0^2 + 2z_0^2} \right) \quad (1-7)$$

which provides the potential equation:

$$\varphi_{(r,z)} = \frac{\varphi_0(r^2 - 2z^2)}{(r_0^2 + 2z_0^2)} + \frac{\varphi_0 2z_0^2}{(r_0^2 + 2z_0^2)} \quad (1-8)$$

This expresses the potential experienced by an ion at any point (r, z) inside the ion trap.

Deriving the Mathieu Equation

The potential described in Equation 1-8 exerts a force on an ion in each direction controlling its motion. The force on an ion increases linearly as it is displaced from the center of the ion trap,¹⁵ which can be expressed independently in the r and z directions as

$$F_r = m \frac{d^2 r}{dt^2} = -e \frac{d\varphi}{dr} \quad (1-9)$$

$$F_z = m \frac{d^2 z}{dt^2} = -e \frac{d\varphi}{dz} \quad (1-10)$$

where $\frac{d\varphi}{dr}$ and $\frac{d\varphi}{dz}$ are the derivatives of Equation 1-8, which for each dimension are

$$\frac{d\varphi}{dr} = \frac{\varphi_0}{(r_0^2 + 2z_0^2)} 2r \quad (1-11)$$

$$\frac{d\varphi}{dz} = -\frac{\varphi_0}{(r_0^2 + 2z_0^2)} 4z \quad (1-12)$$

and when substituted into Equations 1-9 and 1-10 with the relationship

$$\xi = \Omega t / 2 \quad \text{thus} \quad \frac{d^2}{dt^2} = \left(\frac{\Omega}{2} \right)^2 \frac{d^2}{d\xi^2} \quad (1-13)$$

produces the following equations of ion motion:

$$\frac{d^2 r}{d\xi^2} + \frac{8re\varphi_0}{m(r_0^2 + 2z_0^2)\Omega^2} = 0 \quad (1-14)$$

$$\frac{d^2 z}{d\xi^2} - \frac{16ze\varphi_0}{m(r_0^2 + 2z_0^2)\Omega^2} = 0 \quad (1-15)$$

of a form similar to the *equation of motion* of a simple harmonic oscillator:

$$\frac{d^2u}{dt^2} + \frac{k}{m}u = 0 \quad (1-16)$$

where the force constant, k , relates to the driving quadratic field, with each of three axes of motion being treated as separate harmonic oscillations with respect to time.

The applied potential can be expressed as a combination direct current (DC) component U and radio frequency (RF) component $V\cos(\Omega t)$ as in $\varphi_0 = U - V\cos(\Omega t)$, which when substituted into Equations 1-14 or 1-15 forms the second-order differential equation:

$$\frac{d^2u}{d\xi^2} + [a_u - 2q_u \cos(2\xi)]u = 0 \quad (1-17)$$

which is the conical form of the Mathieu equation, used originally to describe the motion of vibrating membranes,¹⁶ and here illustrating the motion of ions within a quadrupole device. This general form can be used for any quadrupole device, and in any direction where u can represent x , y , r , or z . The dimensionless variables, a_u and q_u , are dependent on instrumental parameters as expressed below specifically for a QIT with grounded endcaps and the potential φ_0 applied to the ring electrode:

$$a_r = \frac{8eU}{m(r_0^2 + 2z_0^2)\Omega^2} \quad (1-18)$$

$$a_z = \frac{-16eU}{m(r_0^2 + 2z_0^2)\Omega^2} \quad (1-19)$$

$$q_r = \frac{-4eV}{m(r_0^2 + 2z_0^2)\Omega^2} \quad (1-20)$$

$$q_z = \frac{8eV}{m(r_0^2 + 2z_0^2)\Omega^2} \quad (1-21)$$

where m is the mass of the ion in kg, r_0 and z_0 are the dimensions of the ion trap in m, U and V are the respective DC and RF potentials in V, Ω is the angular frequency in rads/s, and e is a unit of charge in C.

The movement of an ion can be determined as a combination of separate harmonic motions in each direction. With u representing any dimension in Equation 1-17, the function $u(\xi)$ specifies the position (displacement from the trap center) of an ion in each direction. The derivative $u'(\xi)$ provides the velocity of the ion at a given ξ . A complete solution to $u(\xi)$ is composed of two independent parts, which using Floquet's theorem is stated as

$$u(\xi) = Ae^{\mu\xi}\psi(\xi) + Be^{-\mu\xi}\psi(-\xi) \quad (1-22)$$

where μ is a complex constant, $\mu = \alpha + i\beta$, and the function ψ is periodic. From Fourier's theorem a periodic function can be written as

$$\psi(\xi) = \sum_{n=-\infty}^{\infty} C_{2n} e^{(2ni\xi)} \quad (1-23)$$

Thus Equation 1-22 can be expressed in the form:

$$u(\xi) = Ae^{\mu\xi} \sum_{n=-\infty}^{\infty} C_{2n} e^{2ni\xi} + Be^{-\mu\xi} \sum_{n=-\infty}^{\infty} C_{2n} e^{-2ni\xi} \quad (1-24)$$

It is only under specific conditions of the constant μ that the solution of $u(\xi)$ will remain finite as the phase (ξ) goes to infinity. The ion is considered stable within the ion trap when it has a finite position and velocity. This occurs when μ is purely imaginary, thus α always equals zero, leaving $\mu = \pm i\beta$ that must also remain imaginary. In the specific case where β is an integer (i.e., 0, 1, 2, ...), μ is still imaginary, but ion motion is unstable; these are the boundary points between stable and unstable trajectories.

Therefore, it is of interest to determine the β values of the trapped ions. Often β is better expressed in terms of the dimensionless values a_u and q_u , since Equations 1-18 through 1-21 relate them to known ion trap parameters. The values are interconnected using the continued fraction:

$$\begin{aligned} \beta_u^2 = a_u + & \frac{q_u^2}{(\beta_u + 2)^2 - a_u - \frac{q_u^2}{(\beta_u + 4)^2 - a_u - \frac{q_u^2}{(\beta_u + 6)^2 - a_u - \dots}}} \\ & + \frac{q_u^2}{(\beta_u - 2)^2 - a_u - \frac{q_u^3}{(\beta_u - 4)^2 - a_u - \frac{q_u^2}{(\beta_u - 6)^2 - a_u - \dots}}} \end{aligned} \quad (1-25)$$

which requires an initial β estimation derived from the Dehmelt approximation:

$$\beta_u^2 = a_u + \frac{q_u^2}{2} \quad (1-26)$$

that is reasonably accurate for values of $q_z \leq 0.4$.

Stability Diagram

To better visualize solutions of the Mathieu equation, the function $u(\xi)$ can be plotted in a_u , q_u values, referred to as the stability diagram.^{19,20} This is done by first writing Equation 1-24 as

$$u(\xi) = (A+B) \sum_{n=-\infty}^{\infty} C_{2n} \cos(2n \pm \beta_u) \xi + (A-B) \sum_{n=-\infty}^{\infty} C_{2n} \sin(2n \pm \beta) \xi \quad (1-27)$$

using the relationship $e^{i\alpha} = \cos(\alpha) + i\sin(\alpha)$ to convert into trigonometric terms. The sine type functions are then plotted in a_u , q_u coordinates as shown in Figure 1-3. The formed pattern is identical in all directions u (e.g., x , y , r , z). To determine an ion's complete trajectory, motion in all directions must be considered at the same time. It happens that

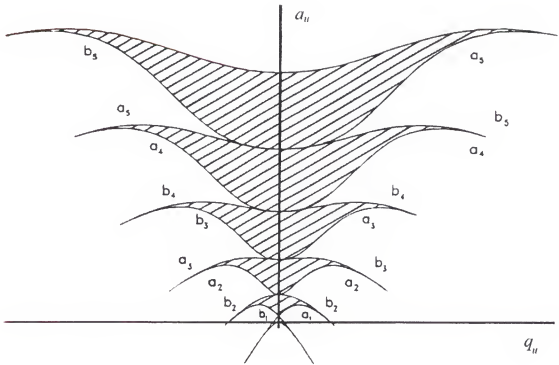


Figure 1-3. Mathieu stability diagram in one dimension. Ion trajectories that map within the shaded regions are stable. The lines marked a_n and b_n are respectively derived from cosine and sine functions of order n . These lines represent the boundary points between stability and instability at integral values of β . (March, R. E.; Londry, F. A. Chapter 2 in *Practical Aspects of Ion Trap Mass Spectrometry*; March, R. E., Todd, J. F. J., Eds.; CRC Press: Boca Raton, FL, 1995; Vol 1, Figure 3, p. 38.)

for both devices, only two-dimensional coordinates need be considered. For the linear quadrupole, only the x and y dimensions are plotted, since no field is exerted in the z direction. For the QIT, the x and y fields are identical because of rotational symmetry, thus motion is plotted in dimensions r and z .

To create a 2-D stability diagram, two plots (each of a different dimension) are superimposed using a common coordinate system. For the linear quadrupole, the x and y dimensional plots are inverted relative to each other (in satisfying LaPlace's equation, $\alpha = 1$ and $\beta = -1$). This is illustrated in Figure 1-4a where two identical plots are reflected across the q -axis; therefore, the plot looks the same whether given in a_x, q_x or a_y, q_y values (only the right half of the diagram is usually shown, because $+q_u$ and $-q_u$ values are indistinguishable). Shaded areas indicate regions of stability in one dimension. Areas of overlap are where ions have stable trajectories in both dimensions. Linear quadrupoles are operated in the region marked as A in Figure 1-4a, because ions can be manipulated in this region with the lowest electric potentials. This is known as the first stability region, shown in an expanded view in Figure 1-4b.

The QIT stability diagram is formed by superimposing plots of the r and z dimensions. Recalling the QIT solution for LaPlace's equation, $\alpha = \beta = 1$ and $\gamma = -2$, the r and z stability regions will differ in magnitude by a factor of -2 . Figure 1-5a shows the QIT stability diagram in a_z, q_z coordinates, with the first stability region expanded in Figure 1-5b. The r stability region is inverted and is twice that of the z , resulting in a lack of symmetry across the q -axis, which differs from that of the linear quadrupole. Ions that have a_w, q_u coordinates that coincide with the first stability region shown in Figure 1-5b will be trapped inside the QIT.

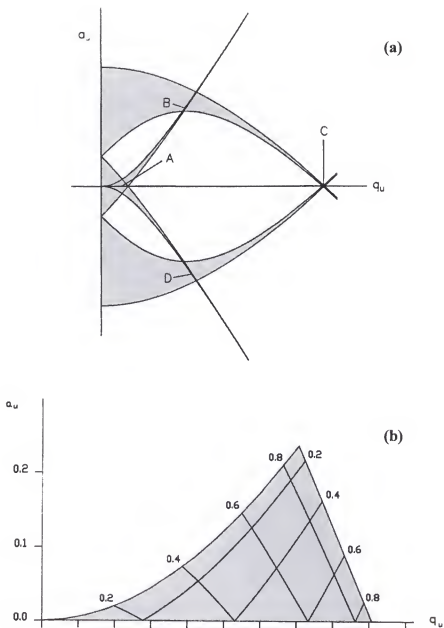


Figure 1-4. Linear quadrupole stability diagrams: a) stability diagrams in two dimensions of a_u , q_u space. Regions of simultaneous stability are marked A through D; b) Enlarged plot of the first stability region, shown for only positive a_u values (symmetrical across the q_u axis). (Adapted from March, R. E.; Hughes, R. J.; Todd, J. F. J. *Quadrupole Storage Mass Spectrometry*; Wiley-Interscience: New York, NY, 1989; Figures 2-7 and 2-8, pp. 46-47.)

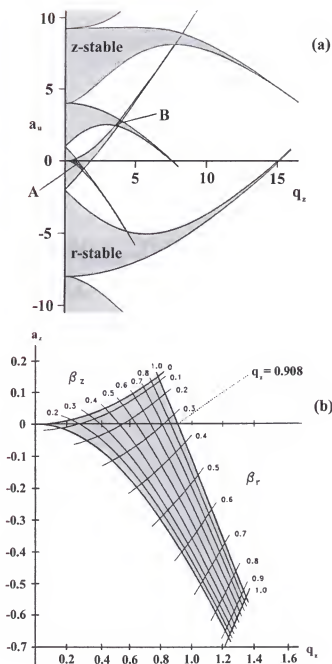


Figure 1-5. Quadrupole ion trap stability diagrams: a) overlapping plot of the r and z stability diagrams; simultaneous regions are marked A and B; b) enlarged diagram of the first stability region, section A. (Adapted from March, R. E.; Londry, F. A. Chapter 2 in *Practical Aspects of Ion Trap Mass Spectrometry*; March, R. E., Todd, J. F. J., Eds.; CRC Press: Boca Raton, FL, 1995; Vol 1, Figures 5 and 6, pp. 40-41.)

Ion trajectories are oscillatory; having angular frequency components related to the β_u values where the ions are stored and the RF drive frequency (Ω) by Equation 1-28.

$$\omega_{u,n} = (2n \pm \beta) \frac{\Omega}{2} \quad (1-28)$$

The primary component, known as the fundamental secular frequency,^{7,14} is of order $n = 0$, expressed as

$$\omega_{u,0} = \frac{\beta\Omega}{2} \quad (1-29)$$

which at the stability boundaries of $\beta_u = 0$ and $\beta_u = 1$ is $\omega_{u,0} = 0$ and $\omega_{u,0} = \Omega/2$ respectively. At these points, the secular frequency of an ion comes into resonance with Ω , suddenly increasing the amplitude of the ion motion by forced oscillation of the harmonic motion. A forced harmonic oscillator must take into account both the natural oscillation forces and the applied force. This is expressed by adapting Equation 1-16 into the form of Equation 1-30 where $F_m \cos \Omega t$ is the applied field. The general solution to Equation 1-30 is shown in Equation 1-31 where the displacement value u increases as the natural resonance frequency (ω) approaches the applied frequency (ω'') and is *in resonance* as G goes to 0.

$$\frac{d^2 u}{dt^2} + \frac{k}{m} u - \frac{F_m}{m} \cos \omega'' t = 0 \quad (1-30)$$

$$u = \frac{F_m}{G} \sin(\omega'' t - \phi)$$

$$G = \sqrt{m^2 (\omega''^2 - \omega^2)^2} \quad (1-31)$$

Superimposed on this motion are the higher-order frequency components of $n > 0$, otherwise known as micromotions. This ion motion at specific β_r, β_z values is illustrated

in Figure 1-6. The amplitude of the ion motion is determined by the C_{2n} coefficient of Equation 1-27, which is based on the a_u , q_u values and the order n . Only the secular frequency and the higher-order frequencies of $n = \pm 1, \pm 2$ are of significance, because C_{2n} diminishes rapidly as n increases.¹⁴ In summary, the terms C_{2n} and β_u respectively determine the amplitude and frequency of an ion's oscillation at specific a_u , q_u values that are based on the m/z of an ion and the other instrumental parameters used in Equations 1-18 through 1-21.

Until now the above theory has dealt with the motion of a single ion within an ideal quadrupole field. This of course is not an exact measure of true ion motion in a real QIT where more than one ion is trapped. Once two or more ions are confined within the quadrupole field, the repulsion of the like charges will affect the field experienced for each ion. Such a condition is known as space charge and must be considered when describing true trajectories.

Space charge is of particular importance when discussing ion behavior within a QIT, since the ions are confined in a finite volume for extended periods (ions have been trapped for days⁷). Various mathematical methods have been deduced to explain the motion of multiple ions within the trap,²¹⁻²⁶ which can then be simulated on computers.²¹ One such method known as the pseudopotential well approach estimates ion motion based on secular oscillation. The approach was first described by Major and Dehmelt^{22,23} and later developed by Todd et al.^{24,25} to quickly determine average ion velocity, energy, and ion cloud density at the space charge limit (the maximum ion capacity).

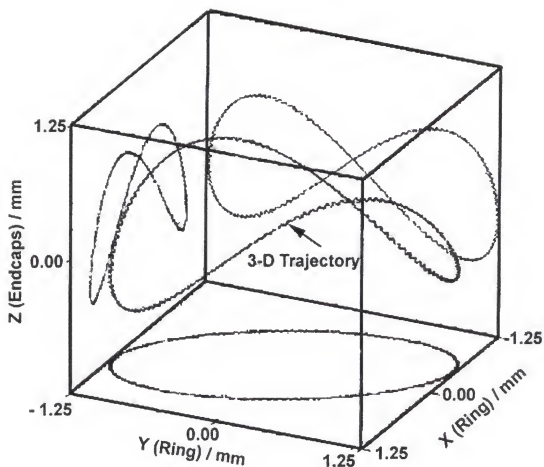


Figure 1-6. Ion motion within quadrupole ion trap depicted in two and three dimensions. (Forbes, M. W.; Sharifi, M.; Croley, T.; Lausevic, Z.; March, R. E. *J. Mass Spectrom.* Vol. 34, 1999; Plate 1, p. 1221.)

Pseudopotential Well Theory

In deriving the pseudopotential well model, ion motion is first considered as a combination of low frequency macromotion and high frequency micromotion components, U and δ , respectively where

$$u = U + \delta \quad (1-32)$$

Then with the assumptions that $\delta \ll U$ and that $d\delta/dt \gg dU/dt$, the Mathieu equation (Equation 1-17) becomes

$$\frac{d^2\delta}{d\xi^2} = -[a_u - 2q_u \cos(2\xi)]U \quad (1-33)$$

Integration over one RF period results in an equation for δ , and using Equation 1-32, the δ term can be removed altogether from the ion motion function (converted into units of time) giving the equation:

$$\frac{d^2U}{dt^2} = -\left(a_z + \frac{q_u^2}{2}\right)\frac{\Omega^2}{4}U \quad (1-34)$$

which describes ion secular motion as simple harmonic motion, which can also be written as

$$\frac{d^2U}{dt^2} - \omega_{u,0}^2 U \quad (1-35)$$

using the Dehmelt approximation (Equation 1-26) and Equation 1-29.

For the condition $a_u = 0$ (no applied DC potential), and by substituting for q_u using Equations 1-20 or 1-21, Equation 1-34 becomes

$$\frac{d^2U}{dt^2} = -\left(\frac{e^2 V_p'^2}{2m^2 u_0^2 \Omega^2}\right)U \quad (1-36)$$

Using the force equation relation:

$$m \frac{d^2 U}{dt^2} = -e \frac{d\bar{D}_u}{dU} \quad (1-37)$$

the estimated potential becomes

$$\frac{d\bar{D}_u}{dU} = \left(\frac{eV_p^2}{2mu_0^2\Omega^2} \right) U \quad (1-38)$$

which when integrated from $U=0$ to $U=u_0$ results in

$$\bar{D}_u = \frac{eV_p^2}{4mu_0^2\Omega^2} \quad (1-39)$$

Equation 1-39 is the pseudopotential equation for any dimension u , with the same units as used in Equations 1-18 through 1-21. Equation 1-39 can also be expressed in terms of q_u values using Equation 1-20 or 1-21.

The model describes the motion of ions as harmonic oscillators, precessing at their secular frequency within the pseudopotential well, which being parabolic (as illustrated in Figure 1-7) acts to confine the ions. A deeper well will confine more ions, thus increases in m , β , and Ω will result in greater storing capacity. This runs contrary to a decrease in storage volume during ionization as either β or m is increased.²⁴

This model is only one approximation of the complete solution to the Mathieu equation. The estimation is fairly accurate for $q_u < 0.4$, but deviates significantly at higher values because of the increased significance of the ignored micromotion. Figure 1-8 compares the pseudopotential well approximation with the complete solution and the smoothed general solution (SGS) that tracks the mean of the macro and micro motions together, accounting for some displacement from the micromotion.

The pseudopotential well model was devised to determine the space charge limit of an ion trap given as

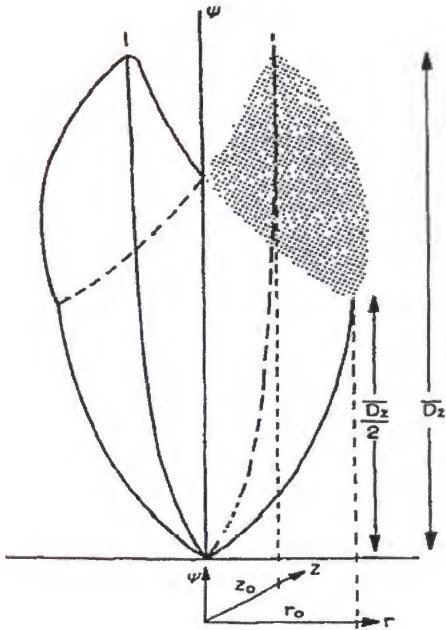


Figure 1-7. Parabolic pseudopotential wells in the r and z dimensions. The relationship of $\bar{D}_z = 2\bar{D}_r$ is based on the assumption that $r_0^2 = 2z_0^2$. (Ghosh, P. K. *Ion Traps*; Oxford University: New York, NY, 1995; Figure 2-9, p. 23.)

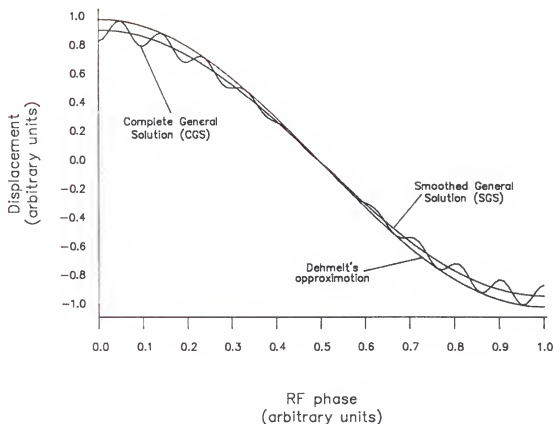


Figure 1-8. Plot of ion motion relative to the RF phase angle. The relationship between the complete solution to the Mathieu equation and two approximations, Dehmelt's pseudopotential well model and the smoothed general solution, is illustrated. The plot is shown for $\beta=0.1$, where the micromotion amplitude is minimal. (March, R. E.; Hughes, R. J.; Todd, J. F. J. *Quadrupole Storage Mass Spectrometry*; Wiley-Interscience: New York, NY, 1989; Figure 2-16, p. 75.)

$$N_{\max} = \frac{3\overline{D}_u}{4\pi u_0^2} = \frac{3V_0^2}{16\pi m u_0^4 \Omega^2} \quad (1-40)$$

Other important approximations using this model are the average velocity and kinetic energy:

$$\langle \dot{u} \rangle = \frac{2u_0\omega_{u,0}}{\pi} \quad (1-41)$$

$$\frac{1}{2} m \langle \dot{u} \rangle^2 = \frac{2m u_0^2 \omega_{u,0}^2}{\pi^2} = \frac{4}{\pi^2} e \overline{D}_u \quad (1-42)$$

which are derived using the equation for harmonic motion $u = u_0 \sin \omega_{u,0} t$, with an amplitude of u_0 and a frequency $\omega_{u,0}$.

The theory presented in this chapter provides a means of explaining the behavior of ions within the QITMS, and serves as a starting point for understanding basic principles behind this work. The next section reviews how the QIT has been used over the course of QITMS development, which divides into three periods each characterized by a different mode of mass analysis.

Modes of Quadrupole Ion Trap Operation

The quadrupole ion trap, like other mass spectrometers, separates ions based on their mass-to-charge ratios. This is accomplished by varying an electrical field to affect an ion's trajectory. Three distinct mass analysis methods have been employed with the QIT: mass-selective ion detection, mass-selective storage, and mass-selective ejection.^{4-6,27,28} Though the first two have been around longer, it wasn't until the introduction of mass-selective ejection in the early 1980's that the QIT became commercially available. Presented is a summary of each method.

Mass-Selective Detection

Mass-selective detection was the analysis method first presented by Paul.^{1,10} Two versions of this method were further developed by Fischer²⁹ and Rettinghaus,³⁰ each based on sensing ions inside the ion trap without having to remove them. This is accomplished by applying a low amplitude auxiliary field across the endcap electrodes at a frequency corresponding to a selected β_z value (a set fraction of the drive frequency). Ion motion is manipulated in a_z , q_z space by ramping either the amplitude of the DC (Fischer's method) or the RF (Rettinghaus' method) potential applied to the ring electrode, as illustrated in Figures 1-9a and 1-9b, respectively. In either case, as the secular frequency of ions at a specific m/z comes into resonance, the applied field will become attenuated and phase shifted, the degree of which is proportional to the number of ions at that particular m/z . Ions of different m/z values are sequentially brought into resonance with the applied auxiliary field to produce a mass spectrum.

Both the Fischer and the Rettinghaus methods suffered from the same problems. Large ion populations or long detection periods were required because of the low sensitivity with tuned circuit detection. Space charge effects were a prominent problem with the high ion densities of the QIT, causing the secular frequency distribution of the ion packet to spread out, broadening the detected signal. Space charge further complicated matters, because ions of differing m/z values experienced different ionic environments. An ion at resonance is influenced by ions of higher m/z values since both are stable within the trap at the same time, but this is not the case vice-versa, leading to nonlinear mass spectra.

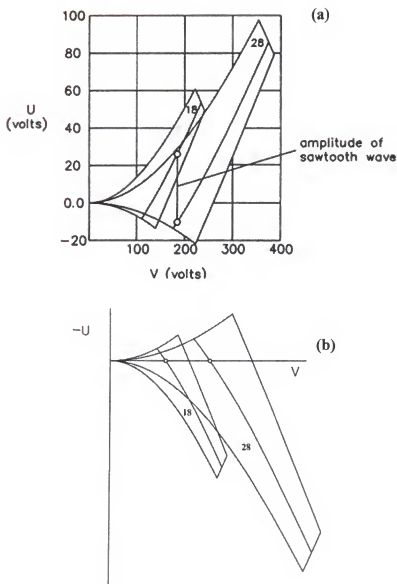


Figure 1-9. Mass-selective detection methods used for in-situ detection: a) the Fischer method using a DC ramp to shift ions of different m/z values sequentially into resonance at a specified β_z value; b) the Rettinghaus method using an RF ramp to shift the q_z value of ions along the $a_z = 0$ line and into resonance at a specific β_z value. (March, R. E.; Hughes, R. J.; Todd, J. F. J. *Quadrupole Storage Mass Spectrometry*; Wiley-Interscience: New York, NY, 1989; Figures 3-1 and 3-2, pp. 113-114.)

To minimize space charge interference, an ion signal can be averaged over longer periods with a lower ion density; however, signal intensity may be affected (enhanced or diminished) by ion-molecule reactions. Maintaining a low ion trap pressure reduces the number of collisions, thus lessening such reactions, as demonstrated by Rettinghaus, who reports detecting a minimum of four ions with the QIT. This suggests that, under specific conditions, the sensitivity of this mode is quite good, but complications from space charge and ion molecule reactions have caused the technique to remain in obscurity. More recently, Fourier transform spectrum analysis was used to improve detection, but unit mass resolution still was not achieved because of problems with space charge.³¹

Mass-Selective Storage

To avoid the complications of mass-selective detection, Dawson et al. opted for a mass analysis method akin to the operation of a linear quadrupoles.^{32,33} Called mass-selective storage, this mode operates by ramping both DC and RF potentials at a fixed ratio (U/V) such that ions of sequential m/z are placed at either apex of the QIT stability diagram. By selecting an appropriate U/V ratio, ions of a single m/z value are stable at any given time, while all other ions fall beyond the $\beta_u = 0$ or 1 stability boundaries. Ions are ejected through holes in the endcaps to impinge on an external detector. This method of mass analysis has the benefit of avoiding ion-ion interactions between different species, and of providing improved mass resolution because of the selective storage approach. However, this method, like mass analysis with a linear quadrupole, has a much lower duty cycle. Ions of differing m/z values are stored separately, requiring more time to produce a full mass spectrum. Under conditions where the gas sample is available only for a short period of time (such as with gas chromatography), the prolonged duty cycle becomes a critical limitation.

Mass-selective storage also requires more electronics to control the ramping of DC and RF potentials at a fixed ratio. Though such electronics are common (used on linear quadrupoles), they add cost, complexity, and size/weight. The addition of endcap holes for ion ejection is another area of concern. Their presence disturbs the quadrupole field, causing further deviation from ideal conditions (truncation of electrodes and machining tolerances are other imperfections), resulting in nonlinear behavior of the QIT. These effects will be considered in more detail in Chapter 5.

Mass-selective storage for QIT mass analysis turned out to be unpopular.^{6,7} The technique provided little improvement over the well developed linear quadrupole technology of the day. The QIT did achieve some popularity at this time after Todd et al. demonstrated that it could be used as a chemical ionization source. Called a quadrupole ion store, or QUISTOR,³⁴ a QIT would replace the normal ionization source of another mass spectrometer (e.g., linear quadrupole, sector, time-of-flight). The QUISTOR was particularly useful for studying ion-molecule reactions, having been developed to examine the decay rates of metastable ions.³⁵

The QIT as a QUISTOR now stood out as a gas-phase ion test-tube.^{6,7,28} Ions could be confined at low pressure and monitored over specified time intervals. This provided better control of gas-phase chemistry where pressure and time are key factors. The low-pressure environment allowed reactions to reach equilibrium slowly, so that reactant loss and product formation could be monitored for kinetics studies. QIT devices were used to determine rate constants, proton affinities, and recombination energies for charge-transfer processes. Reactions at thermodynamic equilibrium could also be examined by simply extending the reaction period. Ions have been reacted with neutral molecules, other ions,

and photons inside the QIT, with complementary experimental results to other techniques,³⁶ most notably those of ion cyclotron resonance, another ion trapping technology that grew in popularity at the same time.³⁷⁻³⁹

Mass-Selective Ejection

Until the late 1970's QIT instruments were rare and all home-built. This was about to change with the advent of another mass analysis method, mass-selective ejection.^{8,9} This method allowed ions of differing m/z values to be trapped simultaneously and then ejected one m/z at a time to an external detector. This provided a greater duty cycle for most applications than with the use of mass-selective storage for the QIT or with a linear quadrupole. Additionally, mass-selective ejection was performed with only an RF ramp, thus hardware was simpler and cheaper. These two advantages made the QIT more competitive with the linear quadrupole, thus commercially viable.⁴

The first mass-selective ejection instruments were simple to operate. A single RF potential would be applied to the ring electrode with the endcaps grounded. Without a DC potential $a_z = 0$, and only the q component of ion motion changes. All ions with q_z values lower than 0.90805 would have stable trajectories, thus the widest mass range is collected at a low RF amplitude. Electrons are injected into the QIT through holes in the endcaps for internal electron impact (EI) ionization. The electron beam is stopped once enough ions have been collected, allowing ions with stable trajectories to settle inside the ion trap. Mass analysis occurs by ramping the RF potential rendering ions of increasing m/z values axially unstable at the $\beta_z = 1$ boundary, and ejecting them through the endcaps into a detector. These steps taken together form a scan function. Figure 1-10 depicts a typical scan function showing the changes in the RF, electron gate lens, and electron multiplier voltages for each step, all of which can be optimized for a specific application.

Collision Gas

Commercialization spurred many advances in QITMS technology. One of the earliest was the incorporation of a lightweight gas inside the ion trap at a high pressure of 1 mtorr, which significantly improved both mass resolution and sensitivity.^{6-9,12,40} These effects were noticed early on;²⁴ a background gas of considerably lower mass than an analyte ion would dampen motion by viscous drag (essentially a dampened harmonic oscillator). This buffering effect collapsed the trapped ion cloud into the center of the device, lowering the displacement and the energy of the ions. The collisionally cooled ions of the same m/z value absorb energy uniformly, and eject together forming narrow peaks. Improvements are most pronounced with the collision gas (B) being considerably less massive than the analyte (A^+) (i.e., $B \ll A^+$). For the opposite case, $B > A^+$, a significant amount of energy is transferred, resulting in the heating of the ion cloud and elastic scattering of the ions, which are lost as their displacement and velocity increase.

Helium was preferred as the collision gas because of its low mass, and high ionization energy ($IE = 24.1$ eV; most analytes are well below 20 eV). It provided a large mass difference with most analytes, and promoted charge-exchange reaction to produce – not neutralize – analyte ions. A collision gas was also important for use with external ionization techniques. Ions enter the ion trap with a large displacement and are subjected to a high RF field strength. Collisional cooling reduces the energy of the ions so that they do not collide with the electrodes.^{6,41,42}

Multi-Purpose Auxiliary Waveforms

Supplemental waveforms applied across the endcap electrodes are used with the advanced functions of today's QITMS instruments. These functions operate on the

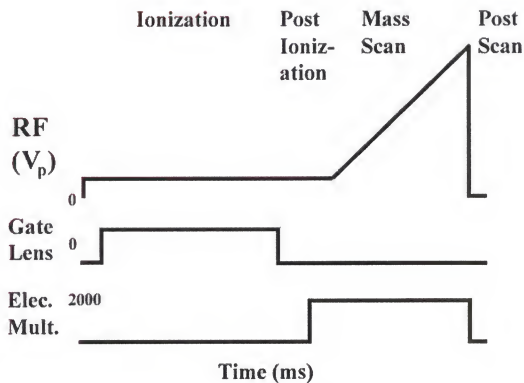


Figure 1-10. Plot of a basic QITMS scan function. The scan is subdivided into discrete steps for ionization, post-ionization, mass analysis, and post-scan activities, with the electric fields changing as needed between each step.

principle that an ion in resonance with an auxiliary field will quickly absorb energy, to increase its velocity and displacement. Broadband waveforms are used during ionization to minimize the storage of unwanted ions. Frequencies of desired ions are left out of the broadband waveform, which keeps their energy low while all other ions are excited and removed.

A single frequency can be used to isolate desired ions. The RF drive amplitude is first ramped to eject all lower m/z ions. Then the higher m/z ions are sequentially ejected as they come into resonance with the auxiliary field, which has a frequency just below the secular frequency of the desired ions. Once isolated, the ions of interest can be collisionally fragmented by application of another auxiliary waveform. This process can be repeated, allowing the QITMS to perform multiple stages of mass spectrometry (MS^n) for improved selectivity.

Supplemental waveforms can also be used to enhance detection. An auxiliary field is applied with a frequency corresponding to a q_z value that is typically just inside the $\beta_z = 1$ boundary (i.e., $q_z \sim 0.9$). The main RF is ramped in the normal manner, but ions are ejected by resonating with the auxiliary field before they reach the $\beta_z = 1$ stability boundary. The process is known as resonant ejection in which ions absorb energy more uniformly to produce tighter ion packets, increasing mass resolution and sensitivity. The resonant ejection frequency can also be decreased to eject ions at lower q_z values for extending the mass range of the instrument.

The enhanced functionality provided on today's commercial QITMS make it a popular choice for many applications.⁴³ The QITMS has found wide acceptance in biological, pharmaceutical, and environmental industries as a versatile, sensitive,

instrument with the power of multiple-stage mass spectrometry - an economical alternative to comparable instrumentation. In this work, however, Paul's intended use of the QIT is explored - to perform trace analysis of lightweight permanent gases - an application typically performed by linear quadrupole RGA mass spectrometers.

Overview of Dissertation

The next chapter discusses the needs of the National Aeronautics and Space Administration (NASA) for a small rugged mass analyzer for monitoring lightweight permanent gases. Four mass analyzer technologies, other than QITMS, are evaluated with a discussion of their performance and suitability for the NASA application. The results provide a comparison basis for evaluating the performance of the developed QITMS instrumentation. Chapter 3 begins with a historical perspective on the use of QIT with lightweight gases. Next, the details of the QITMS instrumentation developed for this application are presented. One QITMS was custom built, incorporating specific features that were found ideal for lightweight gas monitoring. Another QITMS was a modified commercial instrument that offered advanced functionality. In Chapter 4 we examine ion-molecule reactions found to be a significant limitation of QITMS for the analysis of permanent gases. Chapter 5 presents a parametric study of the QITMS, and the development of a custom scan function to minimize ion-molecule reaction effects while maximizing quantitative performance. In Chapter 6 QITMS performance is examined and compared with other analyzer technologies evaluated in Chapter 2. Chapter 7 draws together final determinations from the presented work with consideration for future development of QITMS instrumentation for this application.

CHAPTER 2 MONITORING LIGHTWEIGHT GASES FOR SPACE SHUTTLE SAFETY

Introduction

Since 1981, the Space Shuttle has been the only NASA operated vehicle capable of carrying man into space. As the primary transport to the International Space Station,⁴⁴ the Shuttle is expected to continue operation well into the 21st century. A fully assembled Space Shuttle consists of three major components (Figure 2-1): 1) two solid rocket boosters (SRBs), used in the first 2 minutes of flight; 2) the external tank (ET) containing the cryogenic fuel and oxidizer needed for the Space Shuttle main engines (SSMEs); and 3) the Orbiter with crew compartments, a payload bay, and the SSMEs (Figure 2-2) used during the entire eight minute flight into space. Together the Space Shuttle weighs 2 million kilograms, nearly half of which is amassed by the 1.8 million liters of liquid hydrogen and 0.7 million liters of liquid oxygen held in the ET.^{44,45} Because of the immense volume of explosive cryogenics, leak monitoring is required and in light of the long-term future for Space Shuttle operation, NASA is exploring new technology for improved leak detection.

Mass spectrometers have been the analytical tool of choice for cryogenic fuel leak monitoring since the start of the Space Shuttle program.⁴⁶ They provided low detection limits, stable readings, and fast analyses. The effectiveness of leak detection was proven in 1985 with STS-6 and later in 1989 with STS-35 and STS-38 when during the cryogenic fueling process leaks were discovered, stopping the fueling process and

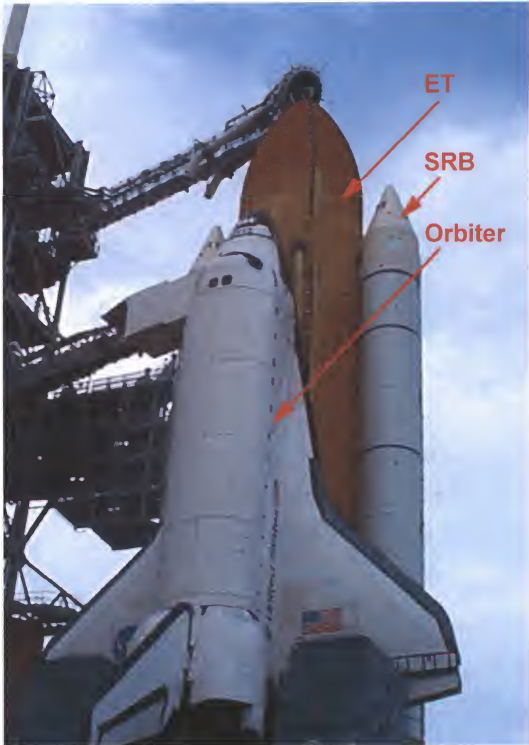


Figure 2-1. The fully assembled Space Shuttle (Atlantis). At launch the Space Shuttle comprises three major parts: the solid rocket boosters (SRBs); the external tank (ET); and the orbiter.



Figure 2-2. Space Shuttle main engines (SSMEs). Three SSMEs are located in the aft end of the orbiter. Cryogenic hydrogen and oxygen are combusted to produce 2 million Newtons of thrust from each SSME. The SSMEs together with the solid rocket boosters place the Space Shuttle into orbit in only eight minutes.

avoiding a potential accident.^{46,47} Recently with STS-93, limitations of these systems became apparent when the rupture of three coolant lines on a SSME was inconclusively detected because it could not be confirmed because of a lack of multiple detectors around the space shuttle.⁴⁸⁻⁵⁰

Present Day Gas Detection

Upon inquiry, NASA determined that the remote location and size of the detection systems were limiting factors. The antiquated rack-sized systems (Figure 2-3) were placed beneath the Space Shuttle in an environmentally controlled room of the mobile launch platform (MLP) (Figure 2-4) where air conditioning and shock absorbing floors helped minimize the impact on the sensitive and costly equipment of the violent launch.⁵¹ Gas sampled from the Space Shuttle therefore was transported over long distances to the remotely located mass spectrometers, causing long delays from sample extraction to analysis. Another limitation was that only two mass spectrometer systems could fit into the MLP because of their large size. Just two of the five available gas lines could be monitored simultaneously, though often both mass spectrometers were used to monitor a single line for redundancy. Switching between gas lines imposed additional delays as the gas load inside the line was replaced.

NASA begins monitoring the Space Shuttle two days prior to liftoff. First the cryogen plumbing is pressurized with helium to trace for leaks. While sampling the nitrogen purged compartments of the Space Shuttle, launch controllers look for helium elevations, but too few sampling lines are available and so pin-pointing a leak is done by hand, a time consuming process. The following day at 8 hours prior to liftoff mass spectrometers are used again while the Space Shuttle is filled with liquid hydrogen and

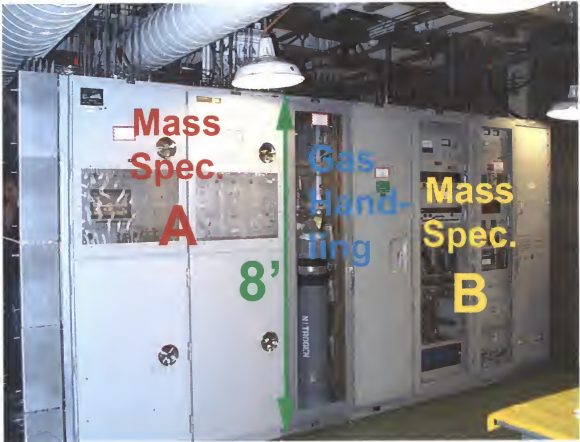


Figure 2-3. Hazardous gas detection system (HGDS). Large rack-sized systems are used to detect leaks within the Space Shuttle. The original HGDS was built in the late 1970s and was upgraded recently (2001) with new technology. The HGDS' large size and sensitivity to launch vibration required it to be placed remotely in an environmentally controlled room with shock absorbing floors. The HGDS used two mass spectrometers (A and B) to provide redundancy.

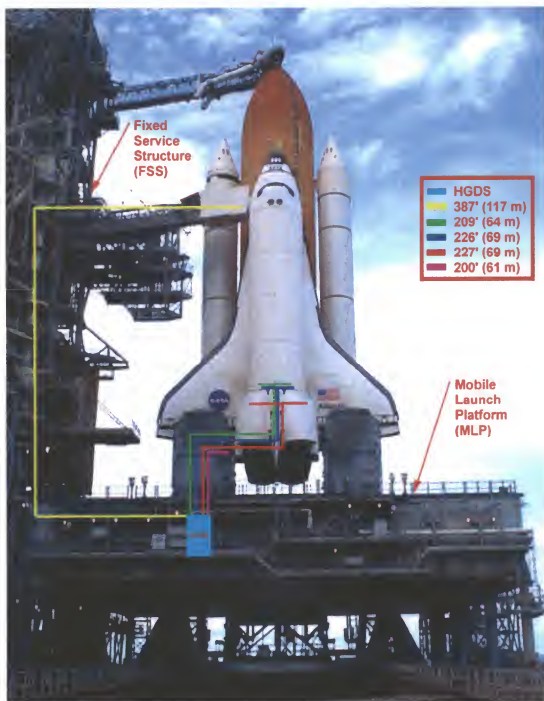


Figure 2-4. Map of transport lines used for delivering sampled gas to the HGDS. With the HGDS remotely located inside the mobile launch platform (MLP), gas from the Space Shuttle had to be transported through transfer lines for analysis. The long length of the transfer lines, between 61 m and 117 m, caused a time delay from 25 s to 50 s between sampling and analysis.

liquid oxygen. Monitoring continues until liftoff, but transport delays prevent analysis of the final critical seconds when a lot of events occur such as checks of the gimble actuators and SSME startup.

Advanced Hazardous Gas Detection Project

Noting the rapid advancement in mass spectrometer technology, NASA was poised to develop a new leak detection system that would resolve present day limitations. In 2000 the aptly named Advanced Hazardous Gas Detection (AHGD) project was contracted to Dynacs Engineering Company at Kennedy Space Center. The recent flurry of work published on miniature mass spectrometers⁵² substantiated the possibility of developing a miniaturized, rugged mass spectrometer unit for leak detection. The unit, about the size of a toaster oven, would be placed up next to the Space Shuttle, thereby reducing transport delay. The small footprint would allow many of these units to be placed around and possibly within the Space Shuttle, providing launch controllers with a continuous stream of data from an entire network of detectors. The added redundancy would also minimize launch cancellations currently caused when an anomalous reading is observed on one mass spectrometer, but cannot be confirmed with the other. The AHGD unit will be of simple design, which lowers costs and allows quick hot swapping of defective units to minimize downtime.

AHGD Leak Detection System Requirements

The analytical performance required of the AHGD prototype, detailed in Table 2-1, is much the same as that required of the original mass spectrometer detection systems,^{53,54} but the speed and size of the new system are significantly different as outlined in Table 2-2.⁵⁵ The AHGD system is required to report ion signals for all four analytes every second. This is considerably faster than the 30-s update period required of the current

system. The new 35,000 cm³, 10 kg sized AHGD system must also perform all the same functions as the current 1.25 million cm³, 450 kg system.

Table 2-1. The AHGD project analytical performance requirements

Requirement	Hydrogen	Helium	Oxygen	Argon
Detection limit (ppm)	25	100	25	10
Accuracy (% error)	< ±10	< ±10	< ±10	< ±10
Precision (% deviation)	< ±5	< ±5	< ±5	< ±5
Response time (s)	< 10	< 10	< 10	< 10
Recovery time (s)	< 30	< 30	< 30	< 30
Mid-level 2-hour drift (%)	< ±10	< ±10	< ±10	< ±10
Upper limit, dynamic range (%)	10	100	25	1

Table 2-2. The AHGD project system specifications

Characteristic	Specification
Total system volume	< 35,000 cm ³
Total system weight	< 10 kg
System power (from 115V 60Hz line)	230 VA
Vibration and shock	18 G, 8 Hz along 3 axes
Final production cost	< \$20,000
Data update rate	1 Hz

Such miniaturization is not trivial; a typical backing pump alone is half the target volume of 35,000 cm³. Miniaturization requires use of the latest in microelectronics, vacuum components, and small mass analyzers. Recently, many types of mass analyzers have been miniaturized including linear quadrupole (Quad),⁵⁶⁻⁶² quadrupole array (QuadArray),⁶³⁻⁶⁶ QITMS,⁶⁷⁻⁷³ time-of-flight (TOF),⁷⁴⁻⁸¹ and sector/cycloidal.⁸²⁻⁹⁰ All were considered for the AHGD project, with representative prototypes supplied from industrial manufacturers when available, and from academia when not. Commercial QITMS instruments have been available for some time, but none were able to mass analyze necessary hydrogen or helium ions. NASA turned to the University of Florida to develop QITMS for the AHGD application

Before beginning QITMS development, the author evaluated four other mass analyzers to provide a comparison basis: 1) a Quad, Figure 2-5; 2) a QuadArray, Figure

2-6; 3) a TOF, Figure 2-7; and 4) a cycloidal focus, Figure 2-8. The analytical performance of each was evaluated using standardized test equipment and methodology and their strengths or weaknesses were determined.⁹¹

Experimental Methodology and Equipment

Four analyte species are monitored during launch preparations. The molecular ion of hydrogen, the cryogenic fuel, is monitored at 2 Da (the atomic ion signal at 1 Da is less intense under standard electron impact (EI) ionization conditions). Helium (4 Da) is monitored, because it is used to trace plumbing leaks and is the pneumatic gas of the SSME actuators (a leaking actuator could disable the associated SSME). Oxygen (32 Da), the cryogenic oxidizer, presents a significant fire hazard at high concentrations, and because of the abundance of oxygen in air (20.9%), argon (40 Da) is monitored to distinguish an air leak from a cryogen leak (argon is the third most abundant constant component of air at 0.93%).

NASA has outlined the following evaluation methodology to be used with all mass spectrometers for determining detection limits, accuracy, and precision, as well as the response and recovery of the system to changing analyte concentrations. The AHGD test procedure below is used to determine all of these criteria. The two-hour drift and dynamic range requirements (Table 2-1) were not evaluated in this preliminary study, because time and materials were not available for the required additional testing.

AHGD Test Procedure

The instrument is exposed to three gas streams: 1) “zero gas” (ZG), which is pure nitrogen; 2) “test gas” (TG), which is a mixture of each analyte (500 ppm H₂, He, O₂, and 100 ppm Ar) in a balance of nitrogen; and 3) “span gas” (SG), which is a mixture of

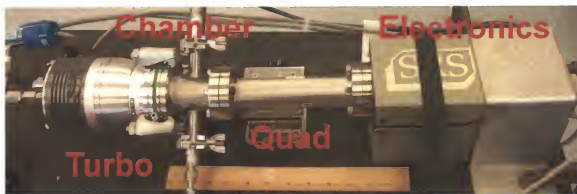


Figure 2-5. Stanford Research System model RGA-100 linear quadrupole mass analyzer. An Alcatel ATH-30+ turbo drag pump was attached to a custom vacuum chamber. A 0.002 in. inlet orifice admits the sample gas, while a Granville Phillips Microlon gauge measures the pressure of the chamber. To the right is the quadrupole assembly, which attaches to the control electronics.



Figure 2-6. Ferran Scientific model POD-01 quadrupole array mass spectrometer. Ferran assembled the shown system specifically for the AHGD project. Inside the case, the system comprises a Ferran Scientific Symphony quadrupole array mass analyzer (45 Da MPA and CNI-06 control electronics), and a custom vacuum chamber evacuated by a Varian V70LP turbo drag pump backed by a KNF diaphragm pump. Gas was sampled through a long capillary, to allow sampling directly from atmospheric pressure.

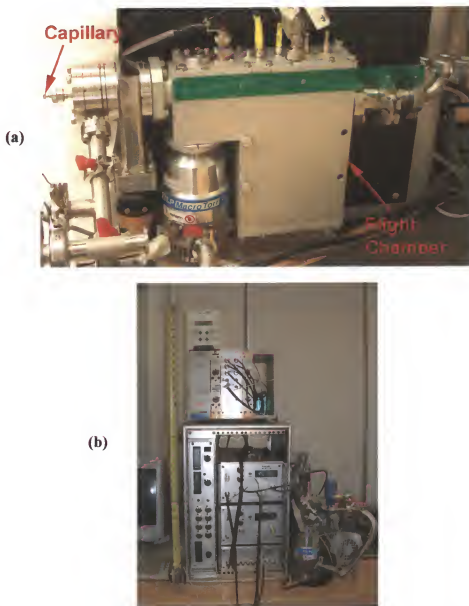


Figure 2-7. IonWorks time-of-flight mass spectrometer. The flight chamber of the IonWorks TOF (a) was compact when compared to other TOF instruments. On the far left, a capillary tube enters an inlet cavity through a 2.75 in. Conflat flange. A mechanical pump evacuates this region via the 0.5 in. pipe (seen extending downward). An orifice admits gas from the inlet cavity into the EI ion source. An orthogonal extraction pulse samples from a constant ion stream, sending ions into a “V” shaped reflector flight path and impinging on an MCP detector. The TOF’s fast speed required sophisticated electronics that were contained in a large rack (b) that dwarfed the mass analyzer.

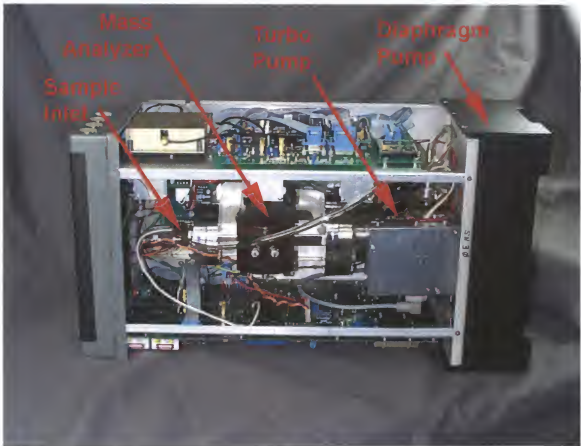


Figure 2-8. Monitor Group MG2100 cycloidal focus mass spectrometer. The crossing magnetic and electric fields of the MG2100 produced a double focusing effect similar to that of a double focusing sector, but with a single analyzer. A gas sample was drawn through a narrow bore capillary into the EI ion source. The ions traveled in cycloidal paths, focused through an aperture to strike a Faraday cup. Ions of different m/z ratios traveling in different paths were sequentially focused through the aperture by scanning the electric field.

each analyte at 10 times the concentration in TG. The following steps are made:

1. Run each gas line for a minimum of 5 minutes to remove air
2. Run ZG for a minimum of 15 minutes to stabilize the system
3. Begin data recording for 2, 4, 32, and 40 Da
4. Run ZG for 3 minutes
5. Run TG for 3 minutes
6. Run SG for 3 minutes
7. Twice, repeat steps 4 through 6
8. Run TG for 3 minutes
9. Run ZG for 3 minutes
10. Stop data recording

Analytical Procedures

Two-point calibration

Data acquired while running ZG and SG were used to generate a two-point calibration. Data points between 2 and 2.5 minutes are averaged together for ZG and SG (a 1 s update rate would average thirty points). Known concentration values certified by the gas mixture manufacturer are used to generate an ion-signal-to-concentration plot of each analyte. This is repeated for each ZG and SG set (total of three).

Calculated detection limit

From the three-minute ZG period of the test procedure, ten subsequent data points after the two-minute mark are converted to values of concentration using the calibration plots. The calculated detection limit is reported as three times the standard deviation of the ten values.

Accuracy of quantification

Data acquired from 2 to 2.5 minutes period while running TG are averaged. This is then converted to a concentration value ($[\text{test}]_{\text{meas.}}$) using the calibration plots, and then compared with the manufacturer certified value ($[\text{test}]_{\text{cert.}}$). Accuracy is reported as the percent error between the two values (Equation 2-1).

$$\frac{[test]_{meas.} - [test]_{cert.}}{[test]_{cert.}} \times 100 = \%Error \quad (2-1)$$

Precision of quantification

In the test procedure, the sequence ZG-TG-SG is repeated three times from which three separate TG concentration values are measured; the average ($\mu_{[test]}$) and standard deviation ($\sigma_{[test]}$) are calculated. Precision is reported as the percent deviation determined using Equation 2-2.

$$\frac{\sigma_{[test]}}{\mu_{[test]}} \times 100 = \%Deviation \quad (2-2)$$

Response time

Response time is defined as the time in seconds needed for transition from ZG to within 95% of TG.

Recovery time

The recovery time is defined as the time in seconds needed for transition from SG to within 5% of TG.

Gas Delivery Assembly

A differential-pressure, flow-by gas delivery system shown in Figure 2-9 was built for the mass spectrometer evaluation. Modifications were made only when necessary to work with a specific mass spectrometer. The delivery system included a gas selection section and an inlet section. Gas cylinders of ZG, TG, and SG, each regulated to an outlet pressure of 10 PSI, were plumbed through three computer-controlled solenoid valves for fast switching. Once selected, a gas passed into a ¼ in. i.d. plenum that was regulated to a constant pressure with a mass flow controller (MFC) (MKS – Andover,

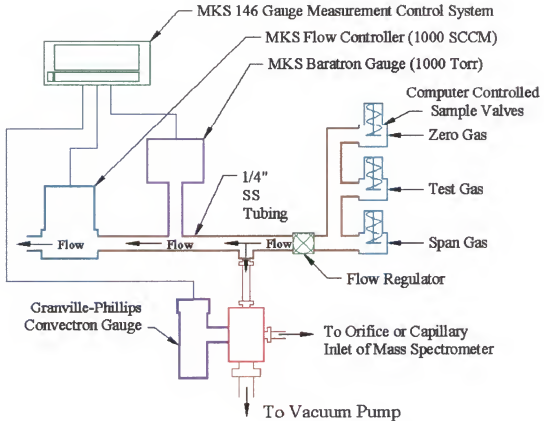


Figure 2-9. The AHGD gas delivery system. Computer controlled solenoid valves were used to select one of three gas streams: 1) pure nitrogen (ZG); 2) 500-ppm H₂, He, O₂, 100-ppm Ar mixture in nitrogen (TG); and 3) 5000-ppm H₂, He, O₂, 1000-ppm Ar in nitrogen (SG). The gas stream was regulated to a constant pressure (900 torr) via a feedback controlled mass flow controller and adjusted to a 500 sccm flow by a regulator. A mechanical pump drew a side stream into an inlet block at a pressure of a few torr. A sampling orifice or capillary then delivers gas into the mass spectrometer.

MA model 1479A) operated by a MKS 146 control box in a feedback loop with a MKS 626A Baratron pressure gauge. A target pressure of 900 Torr was selected, and a flow of approximately 500 SCCM was achieved by adjustment of a regulating valve situated upstream of the MFC. A side stream was drawn out of the plenum (from between the regulating valve and the MFC) by a mechanical pump. This ran past a sampling orifice or capillary, which passed a small amount of gas into the mass spectrometer. The design provided these benefits: 1) the high flow rate of the plenum provided rapid replacement of the gas volume when switching gases; 2) the above-ambient pressure of the plenum kept air from diffusing into the gas system; and 3) a low pressure (2 to 5 torr) side stream allowed sampling into the high vacuum of the mass spectrometer, which was measured with a Granville-Phillips (Hudson, NH) convectron gauge. Short length and small diameter tubes were used where possible for speeding up gas switching.

Evaluated Mass Analyzers

Linear quadrupole

A Stanford Research Systems RGA-100 (Sunnyvale, CA) linear quadrupole mass spectrometer was evaluated. Marketed as a residual gas analyzer (RGA), it was designed specifically to monitor lightweight gases with a mass range from 1 to 100 Da. The system came without a vacuum system, so a small vacuum chamber was constructed in-house (Figure 2-5) to attach an Alcatel (Annecy Cedex, France) ATH-30+ turbo-drag pump, backed by a Vacuubrand (Wertheim, Germany) MZ / 2D diaphragm pump. The system performed best with a chamber pressure in the mid 10^{-5} torr range. The quadrupole measured 11 cm long, with an $r_0 = 4.5$ mm and a drive frequency of 2.7648

MHz. The ion optics and quadrupole settings were tuned as outlined by the manufacturer. Gas samples were admitted through a 0.002 in. orifice directly into the vacuum chamber. Ions were generated in an EI ionization source (-70 eV, 1 mA). A Faraday cup was used for detection, though an electron multiplier was also available.

Quadrupole array

The QuadArray mass analyzer from Ferran Scientific (San Diego, CA) used sixteen rods arrayed four by four, forming nine quadrupoles. Each rod was 1 cm in length with an inscribed r_0 0.5 mm. The drive frequency applied to all rods was 16 MHz, with a mass range from 2 to 45 Da. The evaluated unit was custom assembled for the AHGD application. A model Symphony mass analyzer (45 Da MPA, and a CNI-06 electronics box) was attached to a small chamber evacuated by a Varian V70LP (Lexington, MA) turbo-drag pump that was backed by a KNF (Munzingen, Germany) type UN84.4 diaphragm pump. The capillary inlet was designed to sample directly from a pressure of 1 atmosphere. Because of this, the capillary was attached directly to the high-pressure plenum of the gas delivery system. The instrument was factory tuned; additional in-house tuning was not possible. Ions were generated by EI (-70 eV, 0.3 mA), and were detected by nine Faraday cups.

Time-of-flight

The IonWerks system used an orthogonal-extraction, reflector-TOF packaged into a 10 in. x 10 in. x 2.5 in. vacuum chamber (Figure 2-7). A Varian V70LP turbo drag pump backed by a BOC Edwards (Wilmington, MA) model RV-0.5 rotary vane pump provided vacuum. Like the Ferran Scientific instrument, a capillary was used to transport gas directly from the plenum (900 torr) to the instrument; however, unlike the Ferran a flow-by inlet was built into the IonWerks system. A gas stream was drawn into a

chamber (roughed by the backing pump) and sampled through a 0.005 in. orifice into the EI ionization source (-70 eV, 0.015 mA). The detector was a custom “two-zone” micro channel plate that was designed to increase the response range.⁹² IonWerks optimized the TOF on location for monitoring lightweight gases over a mass range of 1 to 100 Da for the AHGD project.

Cycloidal focus

The Monitor Instruments MG2100 cycloidal focus mass spectrometer used a crossed magnetic and electric double focusing mass analyzer. The complete system was packed into a small 9 in. x 13 in. x 23 in. case. A pair of permanent magnets surrounded the vacuum chamber, which was evacuated by a Varian V70LP turbo drag pump backed by two KNF 84.3 diaphragm pumps (used in series). The inlet capillary of the MG2100 was connected to the in-house inlet block on one end and on the other passed into the EI ionization source (-70 eV, 0.02 mA). The mass range was from 2 to 100 Da, achieved by scanning the electric field of the mass analyzer, and a Faraday cup was used for a detector with a variable gain electrometer (unique to this instrument).

Results of the Examination

The results of the examined analytical criteria are reported for each instrument in Tables 2-3 through 2-6, and are detailed in the following sections. A significant observation is that none of the instruments met all of the AHGD project requirements (Table 2-1), which demonstrates the challenge of the AHGD project. The chapter closes with concluding remarks on each of the evaluated instruments and with general observations pertinent to QITMS development.

Table 2-3. Linear quadrupole analytical performance

Analytical criteria	Hydrogen	Helium	Oxygen	Argon
Detection limit (ppm)	10	12	7	3
Accuracy (% error)	15.7	3.3	16.1	2.2
Precision (% deviation)	1.4	1.8	0.8	0.3
Response time (s)	6	6	6	6
Recovery time (s)	6	6	36	6

Table 2-4. Quadrupole array analytical performance

Analytical criteria	Hydrogen	Helium	Oxygen	Argon
Detection limit (ppm)	58	6	55	5
Accuracy (% error)	44.7	58.4	11.5	4.6
Precision (% deviation)	27.9	10.8	5.2	5.9
Response time (s)	15	15	15	15
Recovery time (s)	15	15	15	15

Table 2-5. Time-of-flight analytical performance

Analytical criteria	Hydrogen	Helium	Oxygen	Argon
Detection limit (ppm)	56	47	80	16
Accuracy (% error)	11.2	60.8	20.3	5.4
Precision (% deviation)	1.9	8.3	4.4	7.5
Response time (s)	15	14	15	16
Recovery time (s)	31	33	32	30

Table 2.6. Cycloidal focus analytical performance

Analytical criteria	Hydrogen	Helium	Oxygen	Argon
Detection limit (ppm)	27	16	105	4
Accuracy (% error)	11.6	35.1	15.2	13.3
Precision (% deviation)	3.7	7.3	7.9	5.9
Response time (s)	22	22	22	22
Recovery time (s)	22	22	44	22

Detection Limits

A calculated detection limit is based on the deviation about the mean of an ion signal acquired when sampling ZG. Ideally the ion signal would remain steady over time, but in reality this does not happen. The background concentration of oxygen and argon may drift because of virtual leaks in the vacuum chamber or trapped gas in the sample delivery system. This is not a problem with hydrogen and helium, found at low concentrations in air (nominally 5ppm and 0.5 ppm respectively); however, these gases

are difficult to remove with turbo-drag pumps once added (poor compression of lightweight gases is discussed in Chapter 3), which can result in signal drifts. Low frequency noise is caused by the signal drifts mentioned above. Higher frequency noise is due mainly to variation in the emission current, the EI ionization process, and the dynamic gas composition within the ion volume at high vacuum (10^{-6} torr).

The calculated detection limits from Tables 2-3 to 2-6 are presented together graphically in Figure 2-10. The Quad results appear better than the other systems. This is somewhat misleading, since the Quad's update time was six times as long as that of the TOF (update times for the four systems are shown in Figure 2-11). The TOF was the only system to meet the 1 Hz AHGD requirement, and it may perform better than the Quad if a longer update time were used, since more data points could be averaged.

The QuadArray had poor detection limits for hydrogen and oxygen, with a large reported error (error bars indicate the 95% confidence interval). This was because of large ion signal fluctuation, shown for oxygen in Figure 2-12 where the signal fluctuates by more than 25% (the similar looking hydrogen signal is off scale). The detection limit for helium was the lowest, but artificially so. The low background concentration of helium produced a very low ion current when sampling ZG. Nearly all of the data points were below the system's detection threshold, which caused them to be reported as zero current. The data set of almost all zeros misleadingly showed low signal deviation.

The worst detection limit was reported for oxygen on the cycloidal focus system, caused by a downward drift of the oxygen signal because of a virtual leak. This was exacerbated because the detection limits were calculated from deviation of ten data

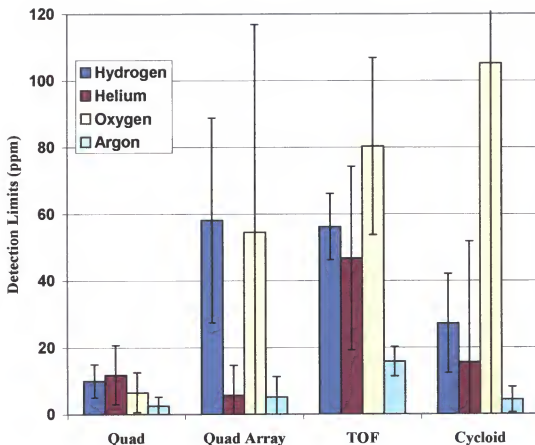


Figure 2-10. Detection limits for the evaluated mass spectrometers. The limits of detection (based on $S/N = 3$) for hydrogen, helium, oxygen, and argon are provided for the four mass spectrometers evaluated. The linear quadrupole mass spectrometer (Quad) was the only system to meet the AHGD requirements (Table 2-1). (Error is reported at the 95% confidence interval).

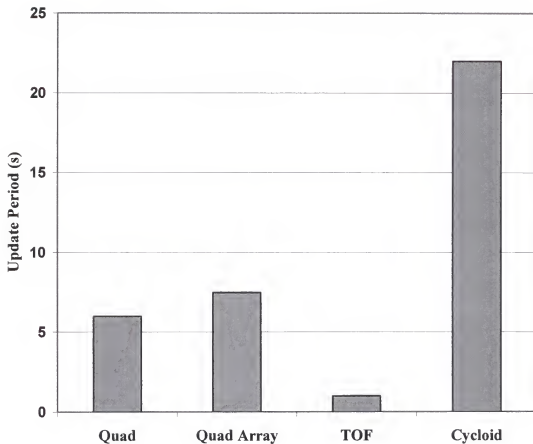


Figure 2-11. Update Rates for four evaluated mass spectrometers. The IonWorks TOF met the AHGD requirement of a 1 Hz update rate, while the other systems were considerably slower. The TOF analytical performance could be improved if data were averaged from 6 to 22 times the measurement period, as was the case with the other instruments.

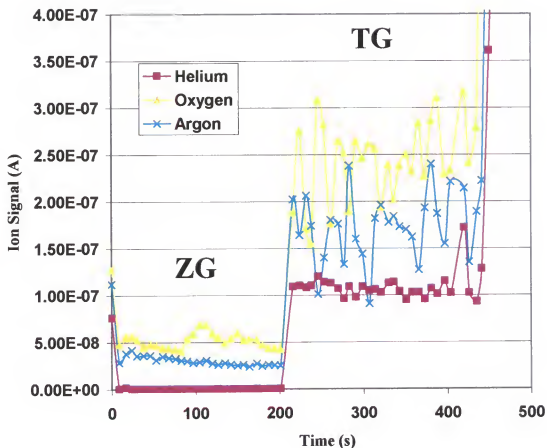


Figure 2-12. Quadrupole array data collected while sampling pure nitrogen (ZG) and then a 500 ppm mixture of hydrogen, helium, oxygen, and 100 ppm of argon (TG). The oxygen detection limit was poor because of the large amount of signal fluctuation (ZG data). The ZG helium ion signal was below the mass spectrometer's detection limit, and the data points were mostly zeros.

points, but with an update period of 22 s, this meant that the standard deviation was taken over the entire three-minute period (compared to a 30-s for the TOF).

Accuracy

An accurate measurement would require a linear signal response, minimal signal drift, and accurate gas cylinder certifications. Accuracy results for the four systems are shown together in Figure 2-13. None of the instruments meet the AHGD requirement of less than 10% error for all four gases. This was surprising for the Quad, which although it was the closest with values for hydrogen and oxygen only slightly above 10%, was expected to perform better. The SRS-100 Quad was considered to be the benchmark instrument for the AHGD project. It had already been extensively evaluated with the same analytical requirements in an earlier NASA project. Previous users of the Quad were able to get all gases below 10%, which suggested that the problem was not caused by the mass spectrometer but by the experimental setup.

To rule out inaccurate gas cylinder certifications as the cause, the experiment was repeated with new gas cylinders. The new accuracy results were: hydrogen, 10.6%; helium, 49.8%; oxygen, 7.4%; argon, 9.2%, showing improved oxygen results but worse helium accuracy. These new gas cylinders were used with the other instruments. Between all three instruments the measured helium concentration ranged from 660ppm to 785ppm, the average of which was within 1.3% of the latest Quad value. This agreement substantiated that inaccurate certifications were the cause for the inaccurate helium measurements, and possibly caused the high oxygen inaccuracy found in the first Quad experiment.

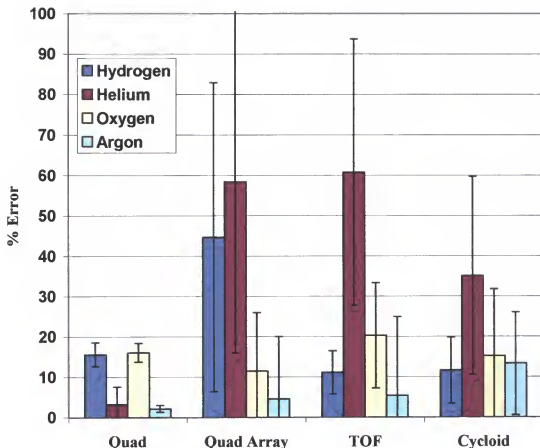


Figure 2-13. Accuracy of the four evaluated mass spectrometers. The % error in calculating a median concentration using a two-point calibration is reported for the mass spectrometer systems evaluated. An erroneous gas cylinder certification resulted in inaccurate helium readings for three systems (a different gas cylinder was used for the reported Quad data). None of the mass spectrometers met the < 10% NASA requirement for all four gases. (Error is reported at the 95% confidence interval).

Precision

The AHGD project required less than 5% deviation throughout the three runs. Only the Quad met this requirement as illustrated in Figure 2-14. The TOF and cycloidal focus systems were within 10%, and the QuadArray showed a significant deviation only for hydrogen which stemmed from large fluctuations in the TG data, caused by unstable ion transmission at a low RF amplitude ($V_p \propto m/z$).

Response and Recovery Time

In addition to a long update period, slow response or recovery to a changing gas concentration would impact the system's effectiveness for the AHGD application. The 10 s and 30 s requirements for response and recovery, respectively, are generous; NASA would prefer to have the time further reduced. Yet even at these values, only the Quad met the response time requirement (Figure 2-15). The other instruments fared better with the longer recovery time requirement (Figure 2-16). An anomalous reading caused the Quad oxygen recovery time to be above 30 ss.

The TOF results were above the requirements, because of its built-in flow-by inlet. The design was similar to the in-house inlet shown in Figure 2-9; a subtle difference resulted in poor response and recovery times. The capillary diameter was much smaller than that used on the in-house inlet, which significantly reduced flow into the inlet cavity and increased the time needed to replenish the inlet's volume and attached vacuum tubes. This caused the slow changing signal shown in Figure 2-17.

Conclusions and Consideration for Future Work

The Quad provided the best analytical performance of the four systems. Still, the Quad was slow with an update period of six times the AHGD requirement. The update

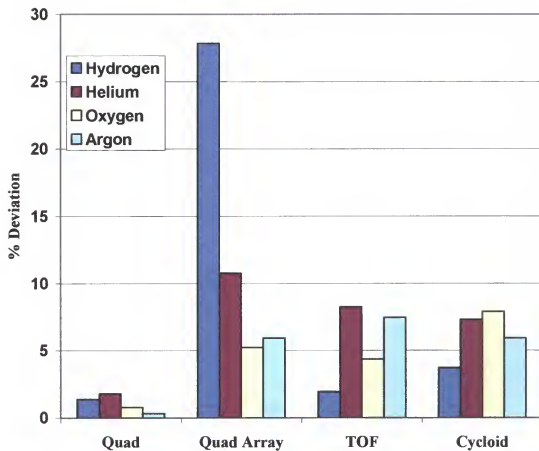


Figure 2-14. Precision of the four evaluated mass spectrometers. The % deviation of three repetitive runs is reported for the four mass spectrometer systems. The linear quadrupole (Quad) was the only system to meet the < 5 % NASA requirement.

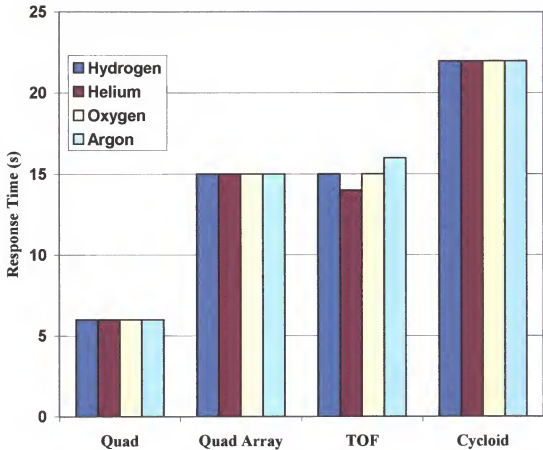


Figure 2-15. Response time of the four evaluated mass spectrometers. The linear quadrupole (Quad) was the only mass spectrometer to meet the <10-s NASA requirement. Both the quadrupole array and the cycloid focus instrument have slow update rates that prevent a precise determination of the actual response time. The TOF instrument responds slowly because of a poor built-in inlet design.

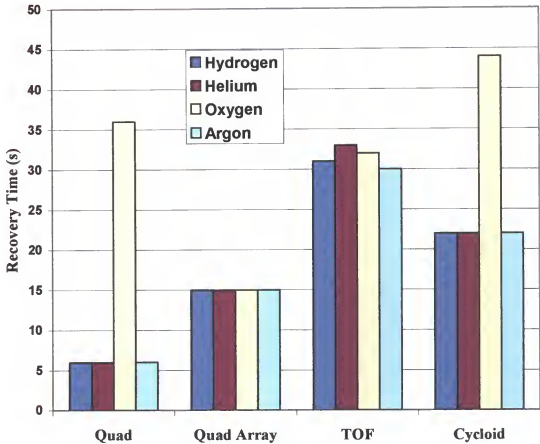


Figure 2-16. Recovery time of the four evaluated mass spectrometers. The NASA requirement of < 30 s was met only by the quadrupole array (Quad Array) for all four gases. Both the linear quadrupole (Quad) and the cycloid focus (Cycloid) had anomalously high recovery times for oxygen. The oxygen ion signal of the Quad began to reduce at the same time as the other three gases, but stopped for a few data points before continuing to decrease to the final level. The Cycloid had a 22 s update rate, which imprecisely defined the response time with only one or two data points.

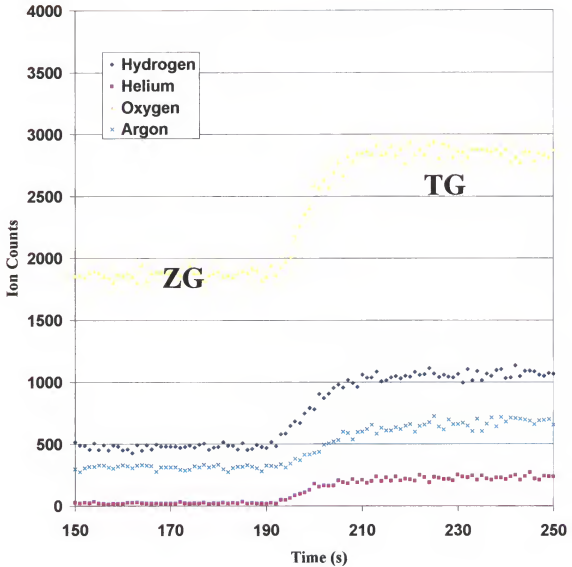


Figure 2-17. TOF data acquired while transitioning from pure nitrogen (TG) to a gas mixture (TG: 500 ppm each of hydrogen, helium, oxygen, and 100 ppm of argon in nitrogen). The transition occurs gradually over approximately 15 s because of the built-in inlet design. A narrow bore capillary provides a minimal flow causing slow replacement of the gas volume inside the inlet.

rate can be increased; however, a significant degradation of performance results. This was a tradeoff common to all of the mass analyzers evaluated. The Quad did have the advantage of a higher emission current, which was from 3.3 to 67 times the emission current used on the other systems. More electrons meant more ions, resulting in improved performance up to the space charge limit of the Quad.

Quadrupole array technology was intended to provide performance comparable to a standard linear quadrupole in a small package. The QuadArray was the smallest mass analyzer (Figure 2-18), but contrary to this intention it performed worse than the Quad. The QuadArray was able to perform about the same as the TOF and the cycloidal focus with all gases except hydrogen. The potential well (Chapter 1) at 2 Da is shallow, which caused poor transmission efficiency, resulting in signal fluctuations. The QuadArray was also designed to operate at a higher pressure than the other analyzers. This was meant to reduce pumping requirements, but the operating pressure of 10^{-4} torr did not provide any benefit since a turbo-drag pump was still required.

The IonWerks' TOF had the largest mass analyzer and vacuum chamber of the group. This was a significant disadvantage, made worse by the large rack of electronics needed to run the instrument. The instrument was fast, but had the shortest update period.

The cycloidal focus instrument was packaged nicely into a portable case that met the AHGD size requirement. The system was also the slowest with an update period of 22 s. The manufacturer indicated that the electrometer was the limiting factor. It had a variable gain, but even at the fastest setting it remained slow. This was because a 10^{12}

ohm feedback resistor that prevented quick current changes, which required the electric field to be scanned slowly.

The preliminary evaluation of these mass spectrometer systems revealed the importance of a well-designed inlet, one that had a high flow with minimal dead volume and used a sampling orifice instead of a capillary. It was also discovered that gas cylinder certification values were not accurate. This would lead to the development of an alternative gas preparation system (Chapter 3). The study also demonstrated the difficulty in achieving the analytical requirements of the AHGD project at the required update rate of 1 Hz. This was later achieved with QITMS technology (Chapter 6), the development of which is presented in the next chapter.

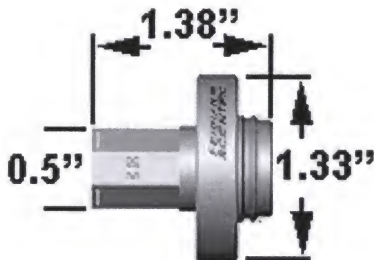


Figure 2-18. Ferran Scientific miniature quadrupole array. The ion source, mass analyzer, and detector were combined into a small package less than 1.5 in. long. A four-by-four array of 1cm long rods formed nine quadrupoles.

CHAPTER 3 LIGHTWEIGHT GAS MONITORING BY QITMS

Introduction

When Wolfgang Paul patented the QITMS in 1960, he realized its applicability to analyzing trace components in a sampled atmosphere.¹⁰ However, commercial development of the QITMS occurred decades later with the advent of mass-selective ejection used with a helium collision gas inside the ion trap.^{8,9,12} The use of this collision gas precluded QITMS use for trace analysis of hydrogen and helium, and previously little effort was made to fill this void. This chapter presents the development of modern QITMS instrumentation for the analysis of lightweight gases.

History of QIT with Hydrogen and Helium Ions

In its early history the QIT was used to store hydrogen and helium ions. In the 1960's, Dehmelt utilized ion traps to contain hydrogen⁹³ and helium⁹⁴ ions in spectroscopy studies of physical and chemical processes. Later, Fulford and March used a QUISTOR for studying ion-molecule reactions of helium ions with molecules in air.⁹⁵ Alheit et al. employed atomic and molecular hydrogen ions to characterize instabilities associated with higher-order anharmonicities within the ion trap.⁹⁶⁻⁹⁸ But, in all the above cases, the ion trap was used exclusively as a storage device; the mass spectrometry was performed by ejecting ions into another mass analyzer, typically a TOF or linear quadrupole. Dawson was the first and until now the last to report on mass-analyzed hydrogen ions with a QITMS.^{24,99} Dawson used the mass-selective storage mode, which involved trapping and detecting ions one mass-to-charge (m/z) value at a time. At this

time, Dawson suggested that the QITMS, when operated in this mode, would be useful for performing leak detection.¹⁰⁰ Compared with mass-selective ejection, Dawson's method was less practical for performing trace analysis of multiple permanent gases, because it was more complex and time-intensive.⁹

Modern QITMS

Mass-selective ejection is the mass analysis method used on all commercial¹⁰¹ and most research QITMS instruments, because of numerous benefits. It is more time-efficient with a high duty cycle, large dynamic range, high sensitivity, and a lower cost.^{9,12} Operating in this mode, mass analysis depends on the ion trap dimensions (r_0 and z_0 in m), the angular frequency (Ω in rads/s), and the RF amplitude (V_p in V_p) as related through the Mathieu equation (discussed in Chapter 1) shown in its axial transformed state in Equation 3-1. To extend the QITMS mass range up to thousands of Daltons, commercial QITMS instruments are set to ion trap parameters that sacrifice their ability to analyze hydrogen and helium. This is best pictured with the stability diagram shown in Figure 3-1. At the lowest stable V_p of a commercial instrument, helium ions (He^+) and hydrogen ions (H_2^+) are beyond the stability boundary at $q_z = 0.908$.

$$q_z = \frac{8eV_p}{m(r_0^2 + 2z_0^2)\Omega^2} \quad (3-1)$$

QITMS performance is improved with the use of a collision gas to dampen ion motion.^{8,9} This process is most efficient with a large mass difference between the analyte and the collision gas species.^{7,99} Therefore, lightweight helium is typically used as the collision gas, with improved ion signal and mass resolution most noticed at m/z values greater than 100 Da. Consequently, permanent gas analysis benefits little from the use of

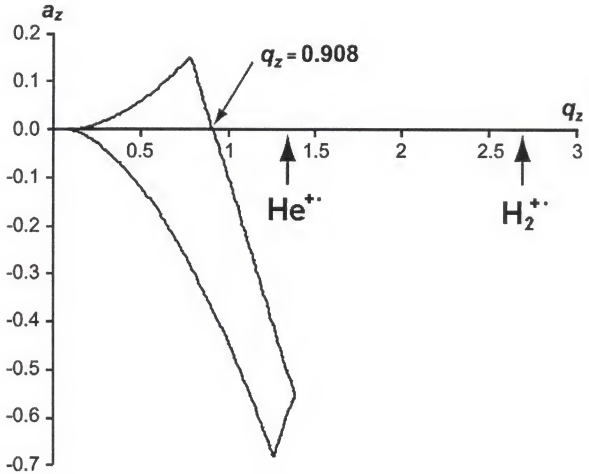


Figure 3-1. Location of hydrogen and helium ions on the stability diagram. Available commercial QITMS instrumentation offers a minimum mass cutoff ($q_z=0.908$) of 6Da. This places hydrogen ions at $q_z=2.724$ and helium ions at $q_z=1.362$, well beyond the stability boundary.

a collision gas. Mass resolution is unimproved, and sensitivity is, at most, doubled.¹⁰² Gases of the same or lower mass than the collision species are difficult to analyze, because scattering occurs and ionized collision gas presents a large amount of chemical noise.

A collision gas was also used for ion injection from an external ionization source. Ion injection was first suggested by Dawson et al. as a means to adapt QITMS to other ionization techniques such as plasma discharge.¹⁰⁰ Since then many ionization types have been adapted for QITMS including electron impact ionization (EI), chemical ionization (CI), electrospray ionization (ESI), atmospheric pressure chemical ionization (APCI), and matrix assisted laser desorption ionization (MALDI). External ionization sources are used in cases when high pressures are needed, or when neutrals from the ionization region would interfere with ion trap operation.¹⁰³ Modern GC/QITMS instruments use combination EI/CI external ion sources. Though both EI and CI can be performed on an internal ionization ion trap,⁷ an external ionization source would permit higher reagent gas pressures for faster analysis, and also allow analysis of negative ions by separating them from positive ions, which is not possible with internal ionization source.^{7,42}

An injected ion has a large initial displacement at the surface of the entrance endcap; therefore, the ion oscillates with a large amplitude of motion, and without any opposing dampening force, the ion will quickly strike an electrode and be neutralized.^{41,103-105} A means must be provided to relax the motion of ions to make ion injection possible. The collision gas, used earlier to improve sensitivity and mass resolution, now serves to reduce the displacement of injected ions. Other alternatives included electrostatic

deceleration and pulsed ion trap operation, but are less efficient and more elaborate. Even with a collision gas, the trapping efficiency for externally injected ions is < 5%, depending on the injection angle and the RF phase angle at injection.^{104,105} With internal ionization only the RF phase angle limits trapping efficiency, with values reported between 15% and 40% efficient.²⁷

Instrumentation and Equipment for Lightweight Mass Analysis

This section describes two QITMS systems developed for the AHGD application (described in Chapter 2); each used mass-selective ejection. The first used internal ionization with no helium gas, in an open trap configuration. The second used all the latest QITMS innovations from Finnigan. With these two instruments modern QITMS was explored for low-mass analysis, an application envisioned since the early days of the ion trap.^{1,10,100}

University of Florida Custom QITMS (UF-IT)

A custom QITMS was assembled at the University of Florida to be more compact and simpler than commercially available QITMS, while achieving the analytical requirements of the AHGD project. Components were recycled from available commercial hardware when possible, and were engineered to work with low-mass ions between 2 Da and 40 Da. Custom software was written to operate the instrument, and acquire data in a format suitable to the AHGD project.

Mass analyzer, source, and optics

Instrument assembly began by selecting an appropriate mass analyzer. The ion trap chosen for the UF-IT was that of a Finnigan (Austin, TX) ITS-40[®] GC/QITMS (circa 1990) shown in Figure 3-2. It had already been designed for internal ionization, and no

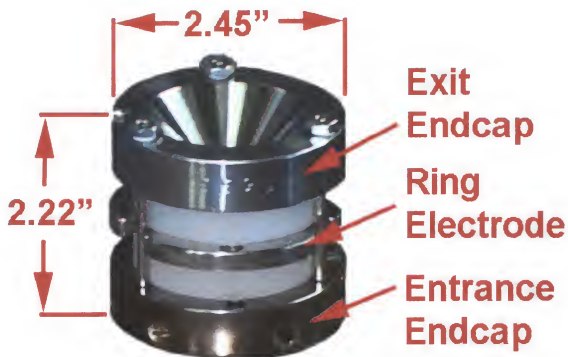


Figure 3-2. The ion trap assembly of a Finnigan ITS-40 used in the UF-IT custom instrument. Three electrodes are stacked together with two quartz spacer rings that serve to electrically isolate and close off the ion trap. The external dimensions are as shown; the internal dimensions are $r_0 = 1.000$ cm, $z_0 = 0.785$ cm.

collision gas was required, plus the optics were simple and compact. The ion trap was machined with hyperbolic surfaces that better approximated an ideal quadrupole field, and would have been difficult to reproduce on a home-built ion trap.

The ion source components of the ITS-40 were also used (shown in Figure 3-3), since they were compact and were already designed to work with the selected ion trap. A bias voltage set between the rhenium filament and the tube lens produced an electron beam turned on and off by the gate lens. The optics sat directly inside the entrance endcap, taking up little space and only the filament assembly was outside, protruding from the Conflat flange.

The solid ring spacers were replaced with three ceramic standoffs as shown in Figure 3-4 to increase conductance of gas through the ion trap (an “open” configuration). Both endcap electrodes were electrically grounded by connection to the Conflat flange, which also held the assembly together on three rods.

Vacuum system

The ITS-40 vacuum manifold (Figure 3-5) was selected for the UF-IT having been designed to mate with the ion trap assembly, and already being compact in size. The transfer line of the ITS-40 was replaced with a shorter 3.5 in.-long and $\frac{1}{8}$ in.-inner diameter (i.d.) tube (Figure 3-6) designed to easily connect with a 0.001 in. inlet orifice (O’Keefe Controls, Trumbull, CT). Gas traveled faster by molecular flow with the shorter, larger i.d. tube, which ended inside the ion trap. A 1-inch NW-16 fitting added to the vacuum chamber allowed connection of a Granville-Phillips model 354 Micro-Ion high-vacuum gauge, placed 90° to the chamber wall to prevent gauge-generated ions from striking the electron multiplier.

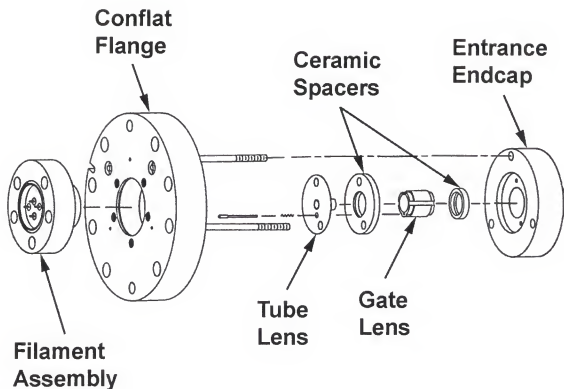


Figure 3-3. Electron optics of an ITS-40 used on the UF-IT. An electron beam from the rhenium filament is focused through the tube lens, and gated on and off from entering the ion trap by the gate lens. The electron optics are recessed into the entrance endcap, taking up minimal space. The filament assembly and the ion trap are bolted on opposite sides to the Conflat flange. (Adapted from Finnigan ITS-40 Schematics Manual, p. 2-15.)

**Ceramic
Standoff**



**Conflat
Flange**

Figure 3-4. Open-configuration on the UF-IT ion trap. The ring spacers of the ITS-40 ion trap were replaced by ceramic standoffs to increase gas conductance through the ion trap. The assembly is bolted together onto a vacuum Conflat flange.

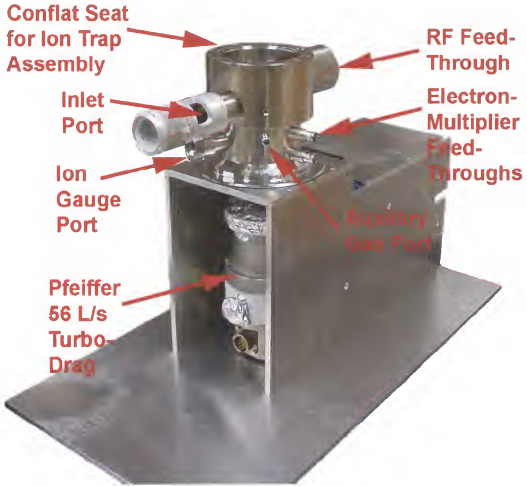


Figure 3-5. The vacuum manifold, turbo-drag pump and chassis of the UF-IT. The vacuum manifold of an ITS-40 was selected for its compatibility with the ITS-40 ion trap assembly and its compact size. A Pfeiffer TPH-065 turbo-drag pump was selected for its high compression ratios for lightweight gases. Components were secured to the shown chassis constructed of $\frac{1}{4}$ in. aluminum plate.

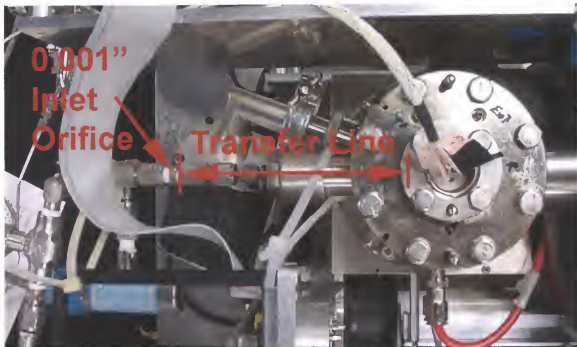


Figure 3-6. The UF-IT transfer line. A 3.5 in. long, $\frac{1}{8}$ in. i.d. transfer line was used to transport gas samples from the 0.001 in. inlet orifice directly into the ion trap. This configuration performed better than fused silica for rapid response to changing gas concentrations.

The high-vacuum was provided by a Pfeiffer TPH-065 turbo-drag pump that offered high compression ratios. Two backing pumps, shown in Figure 3-7, were evaluated independently: 1) a Vacuubrand (Wertheim, Germany) MZ/2D diaphragm pump that featured oil-free operation for minimal contamination (low hydrogen background) in a compact size, and with a base pressure of 2 torr; and 2) a BOC Edwards (Wilmington, MA) rotary vane pump used with an oil mist trap to minimize contamination, which had a low base pressure of 5 mtorr, but was three times the size of the diaphragm pump.

Control, source, optics, detector, and acquisition electronics

The UF-IT was built with electronics from a Finnigan GCQ[®] GC/QITMS (circa 1995.). The main system board (MSB), shown in Figure 3-8, contained circuits for digital control, system monitoring, serial communication, the lens voltage power supplies, and a filament power supply designed for an external EI ionization source. The filament circuit was modified to run the UF-IT filament, keeping it in regulation. One of the lens voltage supplies on the MSB (lens 1 of the GCQ) was connected to the tube lens of the UF-IT, which was originally grounded on the ITS-40. This provided an additional means for tuning the electron beam. The switching voltage supply designed for the gate lens of the GCQ was applied to the UF-IT gate lens. The on/off polarities, configured originally to positive ions, were reversed to gate electrons.

The GCQ detector electronics were also used, which included the DeTech model 2312 electron multiplier (10^5 gain), the high voltage power supply for the electron multiplier (variable from 500 to 3000 V), the electrometer (shown in Figure 3-9), and the 16-bit data acquisition card. A holder for the electron multiplier was designed to accommodate the vacuum manifold with its feed-through connectors, and was positioned directly below

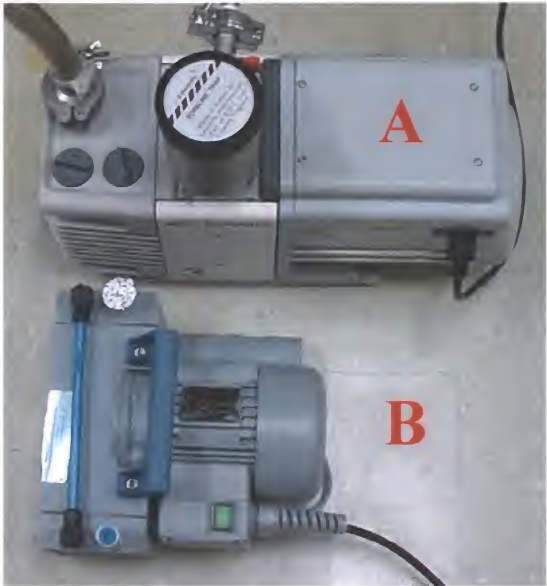


Figure 3-7. Backing pumps used with the UF-IT. Two mechanical pumps were tried for backing the turbo-drag pump: A) a BOC Edwards RV3 rotary vane pump with oil mist trap, base pressure 5 mtorr; B) an oil-free Vacuubrand MZ/2D diaphragm pump, base pressure 2 torr. The compact size and oil-free operation of the diaphragm pump was more in line with the small size requirement of the AHGD project, but the high base pressure was not adequate for backing the TPH-065 turbo-drag pump. Combined with the rotary vane pump, the TPH-065 was able to pump hydrogen faster from the vacuum chamber.

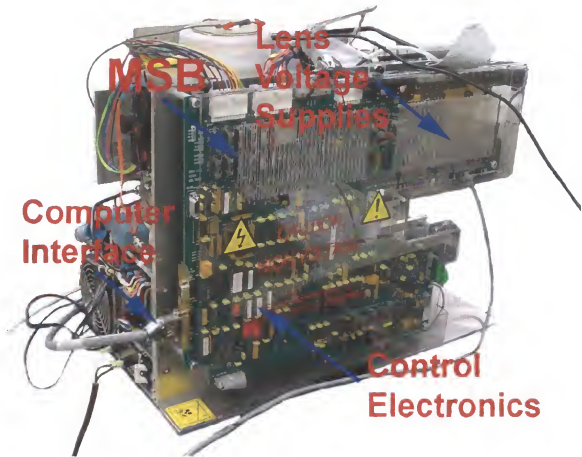


Figure 3-8. The main system board (MSB) of the UF-IT. The MSB contained integral electronic circuits, including the high-speed serial computer interface, the digital and analog control circuitry, and the electron filament and optics power supplies. The board was the bulkiest component of the system, but contained circuitry beyond that used on this system, including three more lens power supplies, and two heater supplies. Eliminating the unnecessary circuits and switching to surface-mount components would reduce the board size significantly.

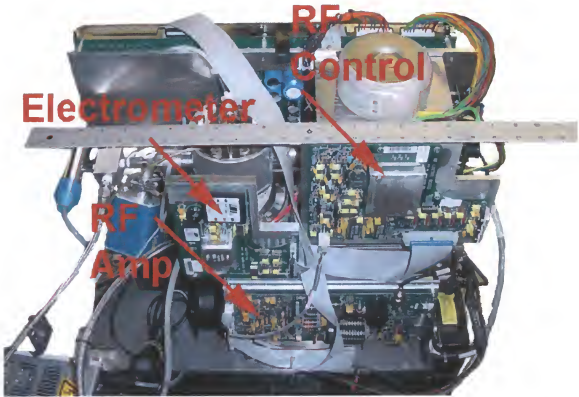


Figure 3-9. The electrometer board, RF control board, and RF amplifier of the UF-IT. In addition to the MSB, three other GCQ circuit boards were incorporated into the UF-IT system: the electrometer board; the RF amplifier; and the RF control board. The electrometer was cut away from a larger GCQ circuit board, and was made to fit with the ITS-40 hardware. The RF amplifier with the RF control board and the RF load circuit (RF coil and ion trap) formed a feedback loop to control the RF amplitude applied to the ring-electrode. A 24 in. ruler suggests the size of the UF-IT.

the exit endcap; no dynode was used. The GCQ electron multiplier did not require additional impedance matching with the electrometer circuit, which was connected to a 16-bit analog-to-digital converter (ADC) that provided more precise acquisition than the ITS-40 12-bit counterpart.

Drive circuitry

The RF drive circuitry of a GCQ was adapted to work with the ITS-40 ion trap (a drawing of the circuit is shown in Figure 3-10). The waveform generator, located on an expansion card inside the control computer, put out a 5 V_{pp} high-impedance signal at a user-selected frequency between 1 and 5000 kHz. This signal passed to an RF amplifier (Figure 3-9) where the waveform was multiplied with a variable DC voltage generated by a 16-bit digital-to-analog (DAC) located on the RF control board. The variable DAC output modulated the amplitude of the RF signal as needed for mass analysis. Power transistors increased the output-power of the amplifier. The signal passed through an impedance matching capacitor and onto an RF coil transformer, which increased the signal amplitude by a factor of 200. A detect capacitor (0.25 pF) sampled the final amplitude, which was compared with the RF DAC setting for feedback control. A high voltage vacuum feed-through transmitted the signal to the ring electrode.

Three RF coils with different diameters were fabricated (shown in Figure 3-11), each with multiple tapping points. This allowed the RF frequency to be varied between 1 and 4 MHz in small increments. The RF coil was placed inside an aluminum box which was used for electro-magnetic shielding (Figure 3-12).

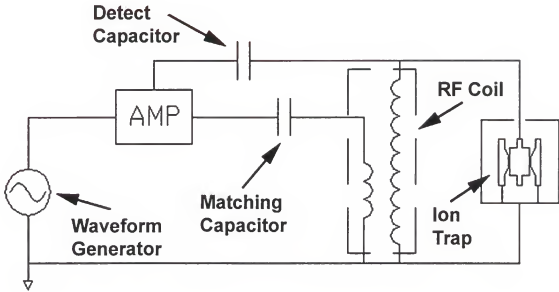


Figure 3-10. The RF drive circuit diagram of the UF-IT. An RF waveform is DC modulated and power amplified by the RF amplifier (AMP). The RF coil then steps up the amplitude to be applied to the ring electrode of the ion trap. A fraction of the final voltage is passed through the detect capacitor for feedback regulation of the output. The primary and secondary sides of the RF coil are RLC networks, which must resonate together for optimal power transmission. The matching capacitor is used to adjust the primary resonant frequency to coincide with the secondary resonant frequency.

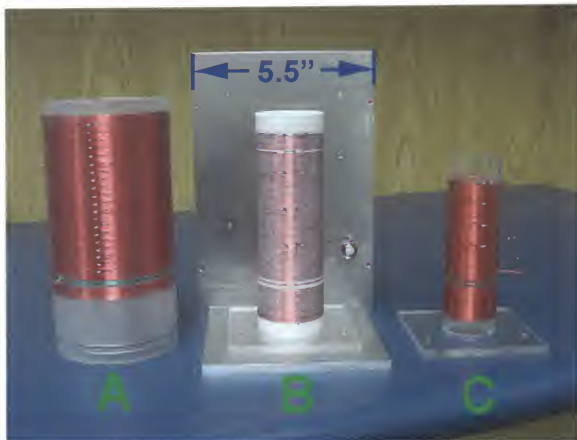


Figure 3-11. RF coils used on the UF-IT. The three RF coils were fabricated to change the frequency of the RF signal applied to the ion trap. A range from 1 to 4 MHz was achieved with the coils, each with multiple tapping points: A) 1.0 to 2.3 MHz, o.d. = 3.48 in.; B) 1.9 to 3.1 MHz, o.d. = 1.85 in.; C) 2.8 to 3.9 MHz, o.d. = 1.49 in..

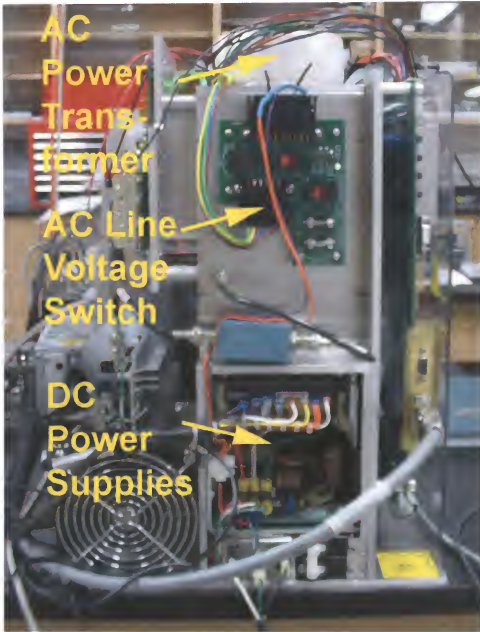


Figure 3-12. Power supplies of the UF-IT. AC and DC power supplies from the GCQ were used on the UF-IT. The DC power supplies were installed into a duct-like portion of the chassis where fans provided forced air cooling. An AC line voltage switch allowed use of either 110 V or 220 V 60 Hz power. An AC transformer converted the line power to multiple amplitudes as needed to run the UF-IT.

Chassis and power supplies

The UF-IT system was constructed around a compact frame made of ¼ in. aluminum plate. The thickness of the aluminum added significant weight to the system, but was beneficial since it allowed new holes to be drilled and tapped for easily adding new components. The chassis was screwed together rather than riveted (used with a thinner material) which allowed the system to be easily taken apart. Power supplies from a GCQ were installed into a duct in the chassis, where forced-air cooling was efficiently used.

Customized software

Another advantage for using GCQ electronics was that the latest (as of 2000) Finnigan software could be used to control the UF-IT. The software had an open-object architecture, which permitted the user to design custom interfaces to operate the instrument using a choice of programming languages. The Custom Tune 1.1 development kit was used with the UF-IT, which came with an example system interface written in Microsoft Visual Basic (Version 6). This code was modified as needed to operate the UF-IT; however, some instrument functions could not be accessed, because this was an early (beta) release of the final software (became XDK for Xcalibur). Extra proprietary code provided by Finnigan (Microsoft Visual C++) was used for adjusting these functions.

Automatic tuning software designed for the GCQ did not work on the UF-IT, because of hardware differences. Software was written (Appendix A) to perform mass calibration using characteristic background ions such as H_2^+ , N^+ , H_2O^+ , N_2^+ , O_2^+ , and Ar^+ , which spanned the targeted mass range. The actual and apparent masses of up to five ions were entered into the graphical interface shown in Figure 3-13. A least-square

fit was then made, producing a slope and intercept value used by the instrument for mass calibration. This process was repeated until an accurate fit was achieved.

New software was also written to display in real-time a plot of ion intensity versus time; the user interface is shown in Figure 3-14, and the source code is in Appendix B. The peak heights of up to eight ions were plotted at a user specified update rate. The user can also save data to a Microsoft Excel spreadsheet where it could be processed later. This display was useful for signal monitoring applications, such as the AHGD project, and was complementary to the qualitative mass spectrum data display already included in the Custom Tune 1.1 software.

Commercial QITMS (PolarisQ)

A Finnigan PolarisQ was selected to evaluate the latest commercial developments for use with the AHGD application. The PolarisQ was released in mid-2000 as a GC/QITMS system featuring an external EI/CI ionization source that required the use of a helium collision gas at a pressure of 1 mtorr. The system included advanced features such as ionization waveforms and resonant injection. One additional feature of interest was that the electronics were fabricated with smaller surface-mount components. This provided all the functionality of the older GCQ electronics, but in a much smaller footprint, which would be useful in assembling a smaller system.

Hardware differences between QITMS systems

The external ionization source, shown in Figure 3-15, was the major difference between the PolarisQ and the UF-IT. A sample gas stream passed through a 0.002 in. orifice (twice that of the UF-IT) and down a 1/8 in. i.d. transfer-line into the ion volume of the source. An electron current of 250 μ A accelerated to 70 eV also passed through the

Mass Calibration	
Actual Mass	Observed Mass
0	0
0	0
0	0
0	0
0	0
65.5386	0
335.298	0

Buttons: FC43, Air, Start, Save, Close

Checkbox: ☐ Show Graph

Figure 3-13. UF-IT mass calibration software. The new code performed mass calibration with user selected ions within the mass range of interest. The GCQ automatic tune used only ions from the FC-43 (PFTBA) molecule. This software let the user select ions of FC-43 or background air with the click of the button, or manually enter upto five ions of their choice. The known mass of each ion was entered in the left column while the apparent mass was entered in the right column. A least-square fitting algorithm was used to generate the slope and intercept values used by the instrument for the mass calibration.

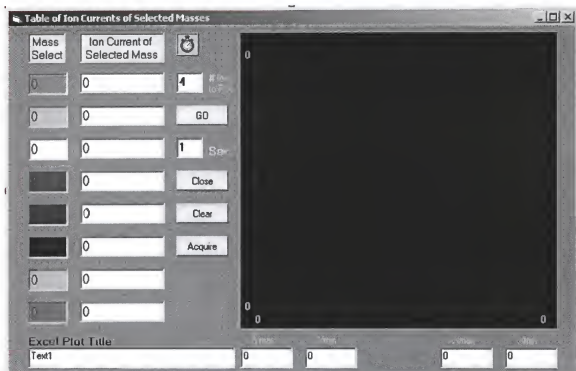


Figure 3-14. New UF-IT real-time graphical display. Data was presented as a plot of ion signal versus time (s). The peak heights of up to eight ions were displayed both numerically and graphically, updated at a fixed rate specified by the user. The acquire button allowed data to be saved to a Microsoft Excel spreadsheet for later processing.

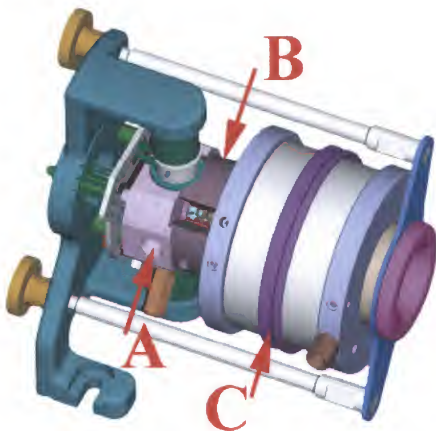


Figure 3-15. PolarisQ external ion source and ion trap assembly. A) gas samples enter the external ion volume, where $250\ \mu\text{A}$ of $70\ \text{eV}$ electrons are used for EI ionization; B) the formed ions are extracted into a three-lens optics stack; C) the focused ion beam passes axially through a hole in the entrance endcap and enters the ion trap where they are stored or ejected depending on their mass-to-charge ratio. The amplitude of the quadrupole field is ramped to bring the trapped ions mass selectively into resonance with an axially applied supplemented RF field (resonance ejection) to axially eject the ions to a detector (not shown). (Adapted from Quarmby, S. T.; Guckenberger, G.B. Introduction to the PolarisQ. *Vender Exposé Pittcon 2000*. New Orleans, LA, March 12-17, 2000.)

ion volume forming EI generated ions. An advantage of the external ion source was that all electrons were in the same electric field during ionization, whereas in an internal ion source electrons were in a dynamic electric field with a broad range of energies (discussed in Chapter 5).

The PolarisQ ion trap was left in a “closed” configuration, since the sample gas passed into the external ion volume. With low conductance, only the ion trap, not the entire manifold, was kept at 1 mtorr of helium. The source and ion trap assembly shown in Figure 3-15 were held in a large vacuum chamber (Figure 3-16), which was evacuated by a BOC Edwards 70 l/s turbo-drag pump backed by a RV3 rotary vane pump. A Granville-Phillips 354 MicroIon Gauge attached to the vacuum manifold was used to measure the background pressure.

Drive circuitry

The PolarisQ RF circuitry was modified to increase the drive frequency. Necessary changes were comparable to those performed on the UF-IT, because the RF circuitry was similar. A smaller RF coil (1.85 in. versus 3.5 in. o.d.) was fabricated for the PolarisQ (shown in Figure 3-16). Tapping points at 50, 65, 80, 95, 110, 125, and 140 turns of the secondary were included, allowing the drive frequency to be variable.

The ion trap of the PolarisQ had a smaller radial dimension (r_0) than that of the UF-IT (0.707 cm vs. 1 cm respectively), which required a proportionate increase in the PolarisQ drive frequency to provide the same potential well depth as on the UF-IT. Based on the final UF-IT frequency of 2.5 MHz, the new PolarisQ drive frequency was calculated to be approximately 2.8 MHz to provide similar trapping conditions, and was achieved by placing the tapping clip (orange clip in Figure 3-16) at 65 turns.

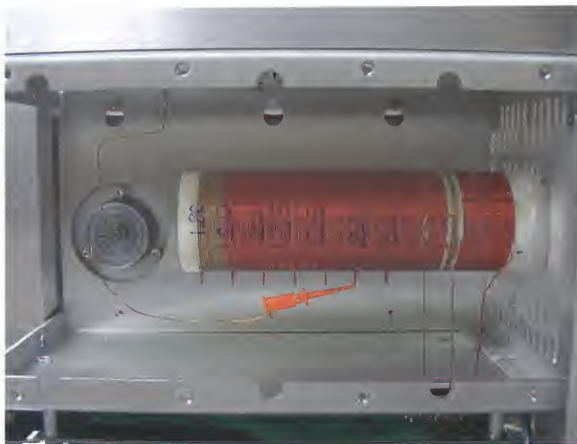


Figure 3-16. The new RF coil of the PolarisQ. The coil is similar to coil B of the UF-IT (Figure 3-11) with an o.d. = 1.85 in.. Tapping points at 50, 65, 80, 95, 110, 125, and 140 turns on the secondary produce a frequency range from 1.8 MHz to 3.2 MHz.

The PolarisQ contained a circuit board called the low-pass filter (LPF) board shown in (Figure 3-17), which had three purposes: 1) to filter high frequency harmonics from the RF drive signal before it was supplied to the RF coil; 2) to supply the matching capacitance of the RF coil primary; and 3) to supply a DC voltage to the secondary of the RF Coil - the trap-offset voltage required for external ion injection. Left in place, the LPF would have significantly attenuated the 2.8 MHz drive frequency, so it was bypassed (the counterpart LPF of the GCQ was not used on the UF-IT; no effect on performance was noticed). A 303pF capacitor in a shielded box provided the capacitance matching of the primary, while the trap-offset circuit was kept in place, since the trap offset was still needed.

The PolarisQ used an AD9832 DDS oscillator chip directly on the RF amplifier to avoid using an external waveform generator like that of the GCQ. The AD9832 oscillator emulated a sine waveform using a 24-bit high-precision DAC, but some harmonics distortion still existed. An LPF (U6 in Figure 3-18) was used to attenuate this distortion, but was removed to prevent attenuation of the new drive frequency. The AD9832 was also bypassed, because it could not be programmed for a frequency beyond ~1.6 MHz. An external waveform generator had to be used to produce the 2.8 MHz signal that was supplied through a coax cable to the amplifier (just after the LPF).

Two additional issues needed to be resolved with the RF amplifier before the PolarisQ was made to work at the new frequency. First, the output of the RF amplifier was significantly attenuated at the higher drive frequency. This was because of the reactant load matching components that were reduced in impedance as the frequency was

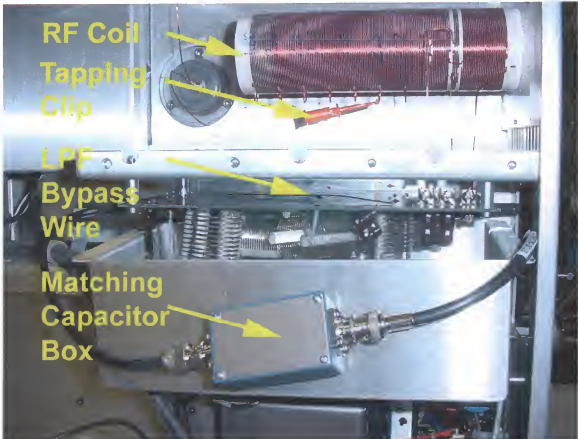


Figure 3-17. The low-pass filter board (LPF) board of the PolarQ. The LPF board served three purposes. First, to attenuate the high frequency harmonics of the 1 MHz drive frequency. This circuit was by-passed to avoid unnecessary attenuation of the new 2.8 MHz drive frequency. Second, to bring the RF coil into resonance by matching the primary resonant frequency to the secondary resonant frequency. A 303 pF capacitor placed in a shielded box took over this function. Third, to apply a DC potential to the ion trap needed for the injection of ions from the external ion source. This part of the LPF board was left intact.

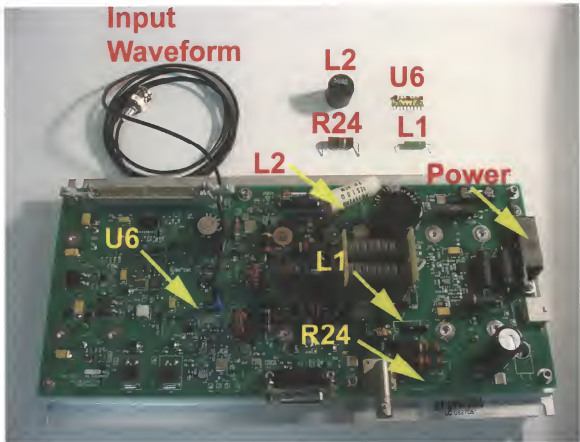


Figure 3-18. The RF amplifier of the PolarisQ. The circuit design of the PolarisQ amplifier was identical to that of the UF-IT except for its use of surface mounted components and the incorporation of an AD9834 oscillator chip for generating the initial signal. To work effectively at 2.8 MHz the low-pass filter board, U6, was removed to prevent attenuation. The initial waveform was supplied from an external waveform generator, because the AD9834 could not be programmed for frequencies above 1.6 MHz. Inductor L1 and resistor R24 were removed to reduce signal attenuation at the amplifier output. Inductor L2 was replaced with a 1 Ω 7W current limiting resistor to protect the power-transistors Q10 and Q12 (not shown).

increased. It was necessary to remove inductor L1, which was shunting a significant portion of the RF power to ground. Resistor R24 was also removed, further increasing the output power of the amplifier.

The second issue involved the power transistors Q10 and Q12 that were operated in parallel. These transistors were each rated to deliver 30 amperes, but were supposed to be adjusted to between 1 and 3 A to prevent overheating. Power was supplied from a +36V DC power supply regulated on the RF amplifier to +28 V. It was determined that at the new drive frequency the load characteristics of the RF amplifier changed, drawing down the DC power supply output to below +35V. The low voltage caused the power-transistors to short (not known why), but was corrected by raising the power supply output to +39V. To help protect the power-transistors, inductor L2 was replaced with a 1 Ω (7 W) limiting resistor.

Custom Software

Finnigan Xcalibur software was used to run the PolarisQ, which includes a later release of the Custom Tune software (used on the UF-IT), now called XDK. XDK (version 1.3) included a custom interface designed in Microsoft Visual Basic that was similar to that used on the UF-IT. This allowed the mass calibration and plot display software designed for the UF-IT to be directly inserted into the PolarisQ interface with minimal modifications. XDK also included access to more commands that were only available on the UF-IT through extra Finnigan proprietary software. This allowed the PolarisQ to be controlled entirely from the Visual Basic interface. To take advantage of this, new software was written, which allowed the user to change the scan function parameters and view a real-time plot display of the data all from one window; the graphical interface is shown in Figure 3-19 with the source code found in Appendix C.

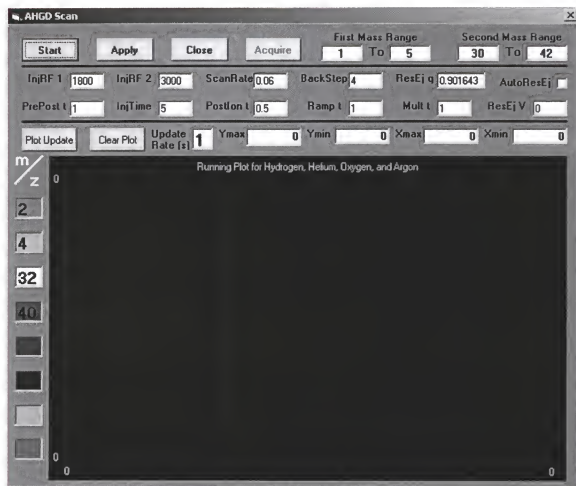


Figure 3-19. The AHGD scan software written for the PolarisQ. The Xcalibur Development Kit (XDK) included with the latest release of Xcalibur for PolarisQ (Version 1.3) allowed access to instrument functions not available with the older software of the UF-IT. The custom AHGD scan function was added to the XDK software, which could be controlled in real-time by the user with the graphical interface.

Tuning the RF Circuit

The RF circuitry used in both the UF-IT and the PolarisQ contained reactive components that were affected by the change in drive frequency. The formed RLC network was an electro-magnetic oscillator akin to the simple harmonic oscillator discussed in Chapter 1. The behavior of the circuit can thus be described by similar equations: Equation 1-16 becomes Equation 3-2 where inertial mass is replaced by inductance L , the restoring force constant by capacitance C , and displacement becomes charge q . The differential of charge q gives the circuit current, $dq/dt = i$, and the circuit resonates naturally at a radial frequency $\omega = \sqrt{1/LC}$. In an ideal LC circuit, energy stored in the capacitor is transferred back and forth to the inductor in a harmonic fashion described by Equation 3-2.

$$\begin{aligned}\frac{d^2 q}{dt^2} + \frac{1}{LC} q &= 0 \\ q &= q_m \cos(\omega t + \phi)\end{aligned}\tag{3-2}$$

The inclusion of resistive component R (all real circuits have at least wire resistance) acts to dampen the oscillation amplitude, just as a collision gas dampens ion motion. This causes a slight shift in the resonant frequency, but because the resistance is low (low dampening force) relative to the inductance of the circuit (high restoring force), power dampening is minimal and the deviation in resonant frequency is negligible. The resistance does have an effect on power loss in the RF circuit. Unlike an ideal LC circuit, an RLC circuit loses energy because of this resistance, lost as Joule heating, the average of which is determined by Equation 3-3. The most efficient way to transmit the remaining power is by operating at the circuit's natural resonance frequency.

$$\overline{P} = i_{rms}^2 R \quad (3-3)$$

During QITMS development, a Wheatstone bridge (Figure 3-20) in combination with a function generator (Stanford Research Systems, model DS345) and an oscilloscope (Tektronix, model TDS-100) were used to determine the resonant frequency. The arrangement determined at what frequency the current (thus power) maximum occurred. Since the current was the ratio of signal-amplitude-to-circuit impedance ($Z = \sqrt{R^2 + (X_L - X_C)^2}$), the maximum current occurred at the lowest impedance when the inductive reactance, $X_L = \omega L$, equaled the capacitive reactance, $X_C = 1/\omega C$, leaving only resistance R . The Wheatstone bridge included two parallel voltage dividers, one with two components of fixed impedance, the other with one component at fixed impedance and the test circuit of unknown impedance (Z_{unk}). The potential differential of the two voltage dividers was monitored with an oscilloscope while a linear frequency sweep was applied from a waveform generator. A dip in the voltage differential would be observed when Z_{unk} reached a minimum at the resonant frequency. A marker signal applied to a second oscilloscope channel determined the dipping frequency - the approximate resonant frequency (± 5 kHz).

The RF coils used on both systems were air-core transformers used to increase the signal amplitude applied to the ion trap. The primary and secondary sides of the RF coil both had natural resonance frequencies. Power was efficiently passed only when the two frequencies matched. Reducing either the diameter of the RF coil or the number of secondary windings would decrease the inductance, $L = \mu_o N^2 l A$, and thus increase the

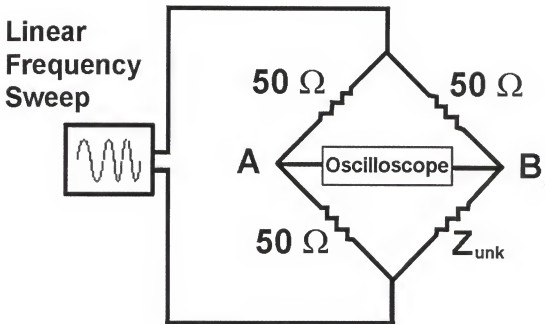


Figure 3-20. Method for determining the resonant frequency of an RLC network. The test circuit of unknown impedance is placed as Z_{unk} . A linear frequency sweep ($10\ \text{V}_{\text{pp}}$, $20\ \text{Hz}$ sweep rate) is applied to a Wheatstone bridge circuit. An oscilloscope is used to measure the voltage differential between the voltage dividers, one of the known impedance (A), the other with Z_{unk} (B). A dip in the voltage differential is observed as the frequency sweep passes to the resonant frequency of the test circuit where Z_{unk} is at a minimum ($X_L = X_C$). A marker signal applied to a second oscilloscope channel is used to determine the dipping frequency. (Adapted from McHale, K. J. Ph.D. Dissertation, University of Florida, Gainesville, FL, 2002; Figure 2-9, p. 90.)

resonant frequency of the secondary. To match the new secondary frequency, the capacitance of the primary was adjusted by changing the matching capacitor. When the two frequencies coincided, the observed voltage dip increased in magnitude, and decreased in width (bandwidth). The tuning efficiency was determined by measuring the quality factor $Q = f_{res} / \Delta f$, where Δf was the dip bandwidth at -3 db (0.707 of signal), and a Q value over 100 was adequate with the use of a class AB amplifier.

Gas Dilution System (GDS)

A gas mixing apparatus called the gas Dilution System (GDS), illustrated in Figure 3-21, was used to evaluate the QITMS performance. Three gas cylinders were used with the GDS (BOC Edwards): 1) containing 99.9995 percent nitrogen gas; 2) containing hydrogen, helium, oxygen and argon each at 500 ppm ± 5 % with balance of nitrogen; and 3) containing the same gasses each at 25,000 ppm ± 5 % with a balance of nitrogen. The manufacturer certified the contents of each cylinder to a tolerance of ± 2 %, relative.

MKS (Andover, MA) mass flow controllers (MFCs) regulated gas flow from each gas cylinder into a plenum (Figure 3-21). The pure nitrogen and the 25,000-ppm mixture were regulated through 1000-standard-cubic-centimeter-per-minute (sccm) 1479A series MFCs, which provided concentrations from 500-ppm to 25,000-ppm (Standard Configuration). In cases where lower concentrations were needed, the 500-ppm mixture was attached to the 1000-sccm MFC in place of the 25,000-ppm mixture, which was attached to a 100-sccm MFC (MKS model 1159B), providing concentrations between 2-ppm and 5,000-ppm (Low-Concentration Configuration). The plenum pressure was manually adjusted with a variable leak valve to 950 torr, measured by a MKS model

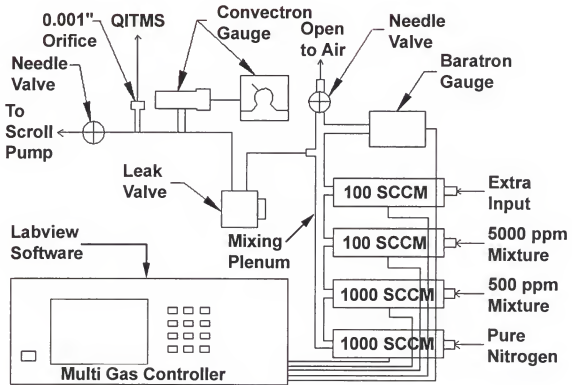


Figure 3-21. Devise gas mixing and delivery system (GDS). Mass flow controllers regulated streams of pure nitrogen and certified gas mixtures at specified rates into a mixing plenum. From this high-pressure region a side stream was drawn through a variable conductance value and passed the inlet orifice of the QITMS by an oil-free scroll pump. Compared with the discrete bottle method devised by NASA, this method avoided complications because of inaccurate gas mixture certifications, and allowed the user to select a concentration from low ppm values on up to the maximum gas mixture concentration provided.

626A 1000-torr Baratron gauge. The MFCs and Baratron gauges were operated with a MKS model 647B multi-gas controller, which was computer-interfaced. Custom software (Figure 3-22), developed in LabView 6i, was used to control gas mixing, and permitted rapid switching between desired gas concentrations. Included was a scheduling feature that allowed the user to set up a time sequenced experiment where sample concentrations would automatically change at specified time intervals (Figure 3-23).

A sample gas stream was drawn from the plenum using a Varian SH-100 (oil-free) scroll pump through a Granville-Phillips 203 variable leak valve. The stream flowed past the inlet orifice of the QITMS. The 203 variable leak valve regulated the pressure at the orifice, which was measured with a Granville-Philips type 127 convection gauge. This differential sampling scheme provided both the higher pressure needed for proper mixing and an acceptable pressure for sampling into the QITMS.

A Stanford Research Systems (Sunnyvale, CA) model RGA 100 quadrupole mass spectrometer was used to compare the GDS to the NASA discrete bottle method, since the linear quadrupole performed well for the AHGD application. Samples from the two gas supplies were selectable by a T-valve for delivery into the quadrupole RGA.

Instrument Development Discussion

GDS Evaluation

NASA methodology for evaluation of mass analyzer performance was outlined in Chapter 2, where difficulties with the NASA discrete bottle method were presented. To evaluate the QITMS, a more accurate and versatile gas mixing apparatus (the GDS) was devised. A single gas mixture was diluted with pure nitrogen in a controlled fashion with all produced concentrations being accurate relative to one another, and removing the

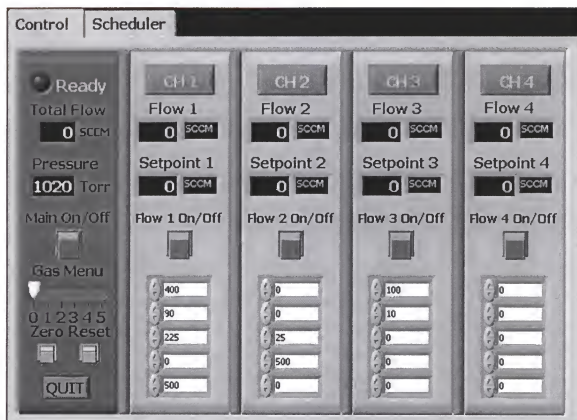


Figure 3-22. Gas Dilution System (GDS) control software. The GDS software allowed the user to quickly switch sample concentrations. The flow settings for four mass flow controllers (MFC) could be adjusted by programming the new values into one of five menus (each a row of the 4x5 array shown) and then sliding the selector to the menu of choice to change all four MFCs at once. Each flow and setpoint as well as the total flow and plenum pressure were displayed.

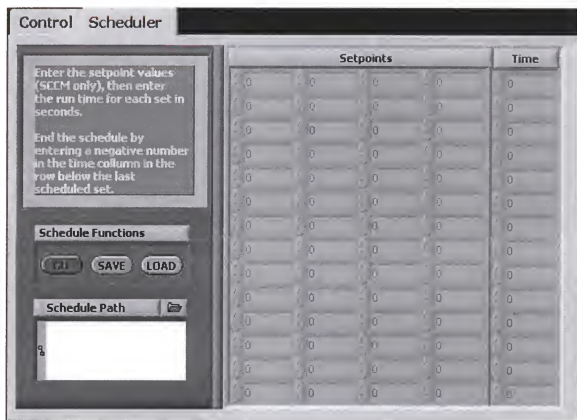


Figure 3-23. The experiment schedule function of the GDS software. The scheduler allowed the user to create and save concentration programs. Each row contained flow values for each MFC and a duration period. Once started, the values listed on the first row would be set. After the period for that row expired, the second row of values would be set (and so on).

manufacturer certification as a possible source of error. The GDS could also produce a wide range of concentrations, not possible with the NASA discrete bottle method. However, since the GDS differed from that outlined by NASA, it was necessary to compare its use with the NASA approved method.

When purchased, a gas mixture cylinder was specified to within $\pm 5\%$ of a nominal concentration, with the actual concentration certified to within $\pm 2\%$ by the manufacturer. Calibration linearity should deviate by no more than $\pm 4\%$, but historically NASA found certified values to be incorrect, as was the case in Chapter 2, adding an immeasurable degree of error to the calibration. The GDS when operated in the Standard Configuration used one gas-mixture cylinder and a pure nitrogen cylinder to produce the ZG, TG and SG standards for the AHGD test procedure (Chapter 2). Therefore, certification errors would not affect the relative linearity of the standards. In addition, the accuracy of the MFCs was $< \pm 1\%$ error with a relative error in linearity of $< \pm 2\%$, which was twice as accurate as the NASA discrete bottle method.

Gas samples were analyzed first from the NASA discrete bottle method (note: the first set of bottles reported in Chapter 2 was used, because the second set had known certification errors), then from the GDS to compare their performance. Mixtures of hydrogen, helium, oxygen, and argon at 0, 500, and 5000 ppm were analyzed sequentially. This was repeated three times, with the ion signals averaged. No prominent differences between the two methods were revealed. Data from each method fell within 5 percent of one another, demonstrating similar precision. Results for hydrogen are shown in Figure 3-24 as an example. A difference in sensitivity of 4.1 % was observed

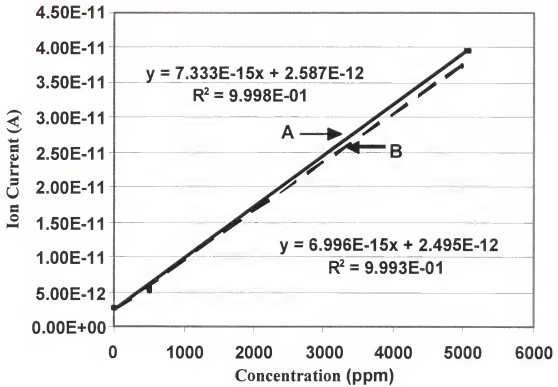


Figure 3-24. Performance comparison of the (A) NASA discrete bottle method and (B) the Gas Dilution System (GDS). Hydrogen gas concentrations (in nitrogen) of 0-ppm, 500-ppm, and 5000-ppm produced from each method were analyzed by a linear quadrupole. The results are similar in both linearity and sensitivity.

for hydrogen, and differences for the other three ranged from 0.5 % for helium to 8.0 % for oxygen. Both methods showed similar concentration linearity, with R^2 values all greater than 0.990, the worst being for oxygen with the NASA discrete bottle method. This suggested further that there was an error in one of the oxygen certified values (alleged in Chapter 2). Background gas concentrations varied between the two methods, because a different pure nitrogen bottle was used for each, and some background drift had occurred. In all, the performance of the GDS was comparable to the NASA discrete bottle method while being more flexible for experiments and avoiding any error from inaccurate certification values.

Results of UF-IT Assembly

The assembled UF-IT was first tried with a drive frequency of 1.0425 MHz using coil A (Figure 3-11) tapped at 105 turns. This was close to the frequency of both the ITS-40 and the GCQ. A mass spectrum of ambient background gas shown in Figure 3-25 illustrates that the instrument did function when assembled. It also indicated by the low ion signal (10^5 vs. a typical 10^7 or 10^8 for the GCQ) that few ions were either being produced or trapped. The gate lens voltage was adjusted to match, as best as possible, the settings of the ITS-40, -130 V when not conducting ions (vs. the ITS-40 -145 V) and +130 V when transmitting the electron beam (versus the ITS-40 +200 V). Also, the electron multiplier high-voltage was increased to 2000 V. Together these two changes improved the ion signal by a factor of 36, seen in comparing Figure 3-25 to Figure 3-26a. A helium collision gas was added into the vacuum chamber through the auxiliary port up to a pressure of optimal ion signal (approximately 2×10^{-4} torr of helium was added). This improved the ion signal by only a factor of two (Figure 3-26), which agreed with

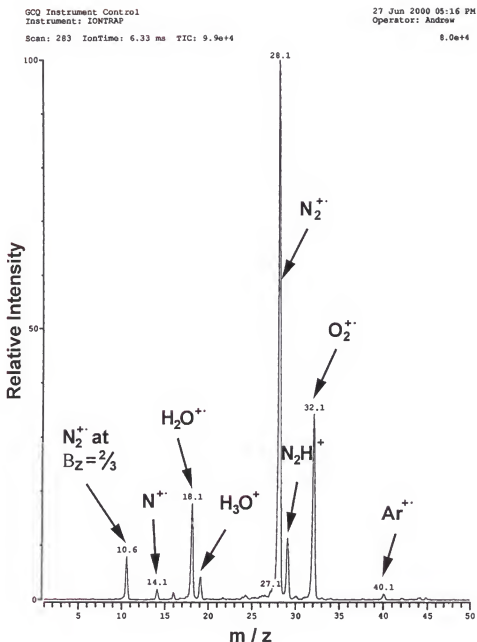


Figure 3-25. First UF-IT mass spectrum taken of room air. Initially a drive frequency of 1 MHz was used, resulting in no observed ion signals below 10 Da. The peak at 10.6 Da was later discovered to be N_2^+ ions being ejected at the $\beta_2=2/3$ resonance line of the quadrupole field in the axial (z) dimension. All other peaks were characteristic of air. Of note was the low signal intensity (TIC $<10^5$).

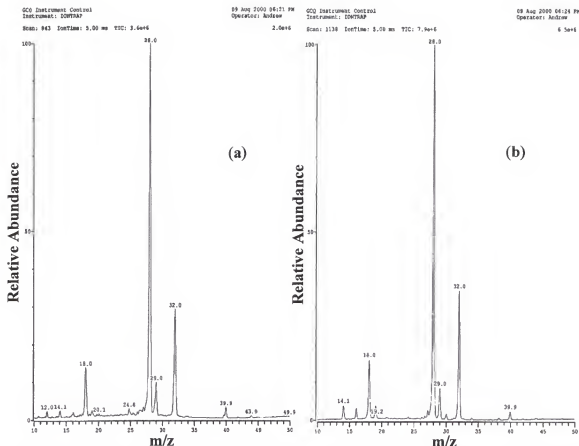


Figure 3-26. The use of a collision gas with the UF-IT. The mass spectrum of room air (a) shows improved ion signal intensity (36 times) after the adjustment of the electron optics and the electron multiplier. With the addition of a helium collision gas at a pressure of 2×10^{-4} torr (b), the mass resolution (FWHM) improved by approximately 20%, and the signal intensity doubled (comparing total ion count (TIC) values).

Shertov's findings for low m/z ions.¹⁰² Thus, the presence of a helium collision gas had a minimal effect on light weight ions, because of the small mass differences between the ions and helium.

Changing the drive frequency

Having verified the operation of the UF-IT, the next step was to change the ion trap parameters to allow the storage of hydrogen and helium ions. The pseudopotential well theory (presented in Chapter 1) was used to explain the limitation for trapping low-mass ions. Equation 3-1 showed a linear relationship between RF amplitude (V_p) and the m/z (Da) of an ion – low mass, low amplitude. The quadrupole field formed by the applied RF signal formed a quadratic potential well within which ions were successfully trapped. The well depth was related linearly to reciprocal mass, but by a square relationship to the RF amplitude as shown in Equation 1-39. Substituting Equation 3-1 into Equation 1-39 gives:

$$\overline{D}_z = \frac{mz_0^2 \Omega^2 q_z^2}{16e} \quad (3-4)$$

allowing the well depth in the axial dimension to be determined for a fixed q_z value, which for the discussion here was 0.2 (typical for ionization). With a 1 MHz drive frequency, and $z_0 = 0.785$ cm, an ion of 2 Da would be in a potential well of depth $D_z = 0.140$ V. To put this in perspective, the thermal potential of a molecule at room temperature would be 0.077 V ($3kT_e/e$). With the presence of neutrals of much higher mass (predominately water and nitrogen), the hydrogen ion cloud would be collisionally heated well beyond the thermal potential, which would be too much energy to be effectively trapped with the weak quadrupole field.

The well depth at specific mass and q_z values could be increased by either enlarging the ion trap inner dimensions (r_0 and z_0), or by raising the drive frequency (Ω). Changing the ion trap dimensions required fabrication of new electrodes, which was difficult because of the problem of machining hyperbolic surfaces. Also, a larger ion trap would require the fabrication of a larger vacuum manifold, which was contrary to the AHGD project goal of building a compact mass spectrometer, and was a significant amount of work.

Instead, the well depth was increased by changing the RF drive frequency. Both the ITS-40 and GCQ had low-mass cutoffs at 10 Da. To lower this to 2, Da for hydrogen analysis, the RF drive frequency would need to be raised to 2.4 MHz (Equation 3-4). Frequencies of 1, 1.4, 1.6, 2.1, 2.3 MHz were tried with RF coil A, while sampling a 5000-ppm analyte mixture, but neither hydrogen nor helium ions were detected. Without having detected an ion of 10 Da under the initial UF-IT conditions, it was not certain that the well depth was sufficient, which would explain why helium ions were not detected at a drive frequency of 2.3 MHz. However, nitrogen ions at 14 Da were detected, and to provide the same well depth at 2 Da, a drive frequency of 3 MHz would be needed. Coil C had a range from 2.8 to 3.9 MHz, and when set to 2.97 MHz, small ion signals at 2 and 4 Da were observed (Figure 3-27a). Yet the total ion signal was low, so it was suspected that not enough electrons were being admitted into the ion trap.

The electron filament power supply of the GCQ was not properly operating with the ITS-40 filament assembly. In the circuit the filament was in series with a 0.25Ω (15W) resistor that formed a voltage divider. The filament current was regulated using a feedback circuit, which monitored the voltage of the divider. The ITS-40 filament had a

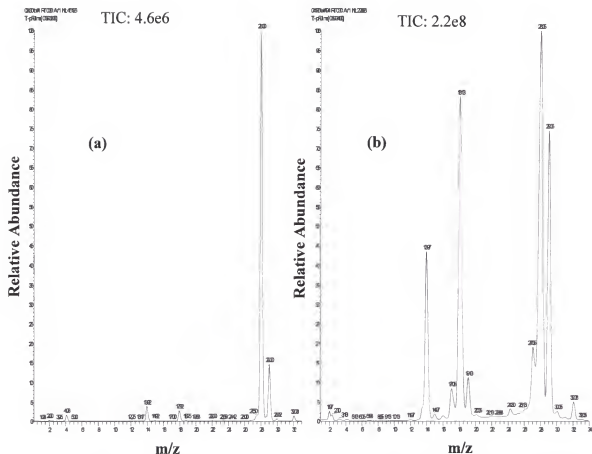


Figure 3-27. UF-IT ion signal improvement after regulating the emission current. Mass spectrum of 1.25% each analyte in nitrogen with the UF-IT set to a 3MHz drive frequency taken before (a) and after (b) the electron filament circuit was brought into regulation.

lower resistance (0.25Ω) than the original GCQ filament (0.5Ω), which increased the relative contribution of the 0.25Ω resistor in the voltage divider; thus, the same feedback voltage was detected at a lower filament current. The 0.25Ω resistor was replaced with a 0.1Ω resistor, which brought the circuit into regulation. The 5000-ppm mixture was analyzed with a $300\mu\text{A}$ emission current. A 50 times increase in ion signal was observed, shown in Figure 3-27b. The ion trap was also space charged, so the emission current hereafter was lowered to $150\mu\text{A}$ and the electron multiplier voltage to 1700 V.

The increased drive frequency produced two effects that reduced mass range. First, as RF frequency increased, the RF amplitude needed to place an ion at a specific q_z value also increased (Equation 3-1), and because of a finite voltage output, the mass range was reduced. Second, the maximum voltage that the RF circuit produced also decreased as the RF frequency increased. As a consequence a higher DC modulation voltage from the RF DAC was needed at 3 MHz to produce the same output amplitude as at 1 MHz. The maximum mass that could be analyzed at 3 MHz was 34 Da, which prevented the analysis of argon ions at 40 Da.

Tuned to the lowest frequency of coil C, 2.76 MHz, the upper mass limit was calculated to be 40 Da. The data of Figure 3-28 verified that argon ions could be detected, but the upper mass limit was right at 40 Da, which caused day-to-day difficulties with the argon signal. RF coil B was therefore used, tuned to a drive frequency of 2.5 MHz, which increased the mass range to between 2 and 60 Da, a preferred configuration.

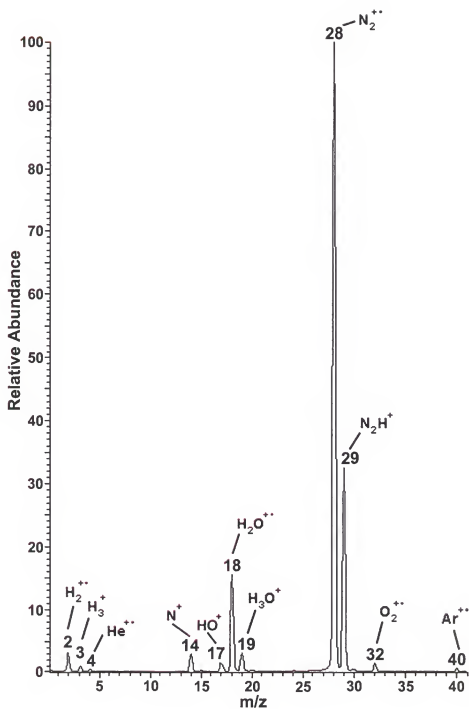


Figure 3-28. Mass Spectrum of 1.25% each analyte in nitrogen acquired on the UF-IT at a drive frequency of 2.76 MHz. All four analytes are clearly observed. In addition, products of ion-molecule reactions are observed at 3, 19, and 29 Da. The significance of ion-molecule reactions are further discussed in Chapter 4.

Pump difficulty with hydrogen

Having sufficiently reduced the low-mass cutoff, the concern now was that the hydrogen background signal appeared elevated relative to other analyte signals. Hydrogen would be the predominant species at ultra-high vacuum levels ($< 10^{-8}$ torr),¹⁰⁸ but at a background pressure of 10^{-6} torr the amounts of nitrogen, oxygen, and water should be magnitudes higher than that of hydrogen, not of equal magnitude as the ion signals suggested. It was possible that ionizing and trapping conditions were preferentially trapping low-molecular-weight species; however, only elevated ion signals for hydrogen, not helium, were observed. Difficulty with the hydrogen signal was further observed when running the AHGD test procedure (0, 500, and 5000 ppm of each analyte in nitrogen) as seen in Figure 3-29a. After the hydrogen concentration was increased, the ion signal did not reach equilibrium (even after more than an hour). When decreasing the hydrogen concentration, the inverted behavior was observed with the signal decay extending for hours. By contrast, helium gave the expected sharp increase or decrease followed by a plateau in the signal level.

After adjustments to ionization and trapping parameters failed to improve hydrogen analysis, the pumping efficiency was questioned. As it turns out, the choice of an effective pumping system was not trivial for this application, because of difficulties with pumping hydrogen. With the use of a turbo-drag pump, the partial pressure P_i of molecule “i” inside the vacuum chamber is determined by Equation 3-5:

$$P_i = \frac{Q_i}{S_i} + \frac{P_i'}{K_i} \quad (3-5)$$

where Q_i is the incoming gas load, S_i is the pumping speed, P_i' the partial pressure at the

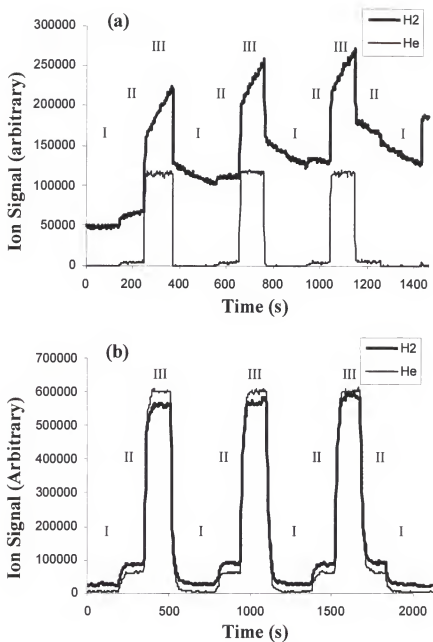


Figure 3-29. Difficulty with pumping hydrogen. Proper compression of hydrogen from the vacuum chamber was critical: a) turbo-drag pump backed by a compact diaphragm pump performed inadequately; b) turbo-drag pump backed by a dual stage rotary-vane pump demonstrated improved compression ability. (Analyte concentration: I, 0-ppm; II, 500-ppm; III, 5000-ppm.

pump exhaust, and K_i the compression ratio. The pumping speed (S_i) depends on the ratio of the pump's rotational spin (a constant) to the thermal velocity of gas "i" ($\langle v_i \rangle = \sqrt{6kT/m_i}$). Thus, the small hydrogen molecule will have a slow pumping speed. As more hydrogen was added, it was not pumped away fast enough and the partial pressure in the chamber continued to rise. When hydrogen was no longer added, that which had built-up was slowly removed from the vacuum chamber. To resolve this a rotary-vane mechanical pump was used to replace the diaphragm pump. The data in Figure 3-29b showed that the hydrogen signal now quickly reached equilibrium when the hydrogen concentration was changed. As well, the hydrogen background signal was reduced by roughly 50%. The compression ratio K_i decreased as the $\sqrt{m_i}$, thus the compressibility of hydrogen was poor; lowering the backing pressure P_i' helped compensate for this.

Exploring the PolarisQ

The PolarisQ provided the use of an external ionization source, ionization waveforms, and resonant ejection. These features are known to improve QITMS performance for detection of larger molecules (e.g., VOCs and biologicals), but here their effect on analysis of lightweight gases was explored.

Collision gas and external ionization

The PolarisQ mass range extended up to 1000 Da prior to modifying for the AHGD application. Figure 3-30a shows that the instrument was able to analyze lower mass ions down to 14 Da. The PolarisQ produced a background spectrum similar to that of the UF-IT, but unlike the UF-IT, the PolarisQ was unable to operate when the helium collision gas was removed (Figure 3-30b-d).

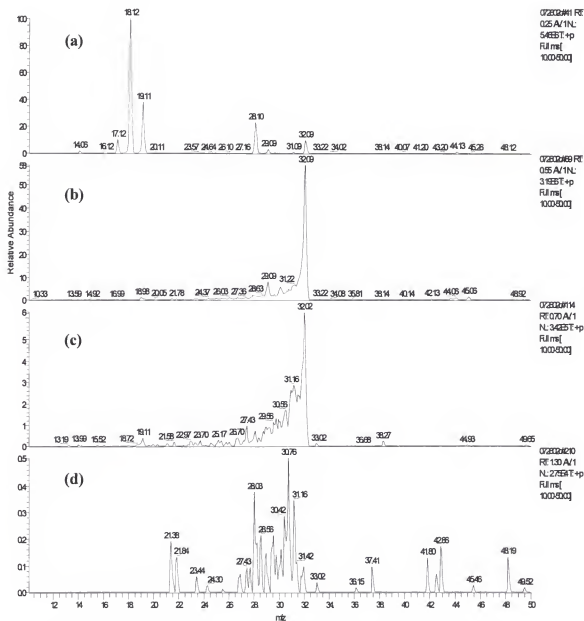


Figure 3-30. Removing the collision gas from the PolarisQ. Ions injected from an external ion source require the use of a collision gas to efficiently trap them. These mass spectra show the dramatic change as the helium collision gas is turned off: a) a mass spectrum of background gas with a 1 mtorr pressure of helium in the ion trap; b) after the collision gas is turned off, all other ions readily react with oxygen, which becomes the dominant peak; c) as the helium pressure lowers further fewer ions are able to be trapped; d) finally only noise is detected when the helium collision gas has been fully depleted (the ion intensity is 0.5% of (a)).

The requirement of a collision gas proved to be a significant disadvantage of an external ion source. First, the collision gas would interfere with the analytes, and second, a helium gas line would need to be run to each mass analyzer placed on the launch pad. Interestingly, as the collision gas pressure was reduced, ion-molecule reaction products not observed before were seen. The thermodynamic end product was the oxygen ions (this will be covered further in Chapter 4).

Injection waveforms

In the AHGD application, nitrogen ions were the primary component of the chemical noise. This chemical noise would be most significant for ions that were close in mass to nitrogen (e.g., oxygen). The PolarisQ used injection waveforms to remove such chemical noise sources.¹⁰⁹ All ions inside an ion trap have a different secular frequency, ω , based on their m/z value. By applying a broadband waveform that combined frequencies associated with all m/z values outside the mass range of interest to the endcaps of the ion trap, these ions would be resonantly excited and if set to the right amplitude would be ejected from the ion trap leaving only the ions of interest.

The effect of ionization waveforms was captured on the oscilloscope in Figure 3-31a-c. The acquisition mass range used was from 30 to 42 Da, with a 6 Da backstep (i.e., the RF amplitude is ramped starting at a voltage corresponding to 24 Da and scanned upward; the computer started its acquisition at 30 Da). Application of the injection waveforms at 1V, than at 2V, reduced the ion signals at 28 and 29 Da, which were no longer being stored inside the ion trap. Primarily ion signals outside of the mass range were reduced, but there was also a reduction in the ion signals for oxygen and argon as seen in Figure 3-32. What was not observed was any increase in the ion signal

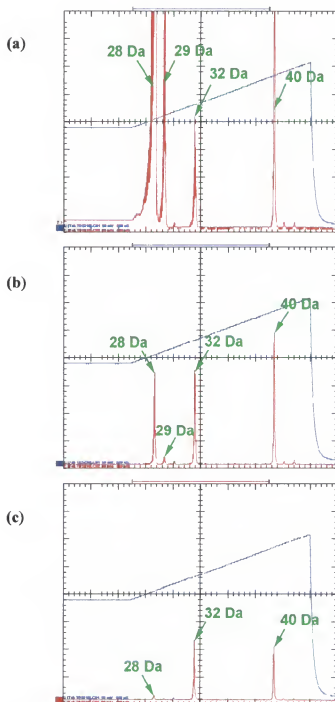


Figure 3-31. Oscilloscope plots of electrometer signal (red) as the RF amplitude was ramped (blue) during mass analysis. The mass range of 30 to 42 Da was selected, with a 6 Da backstep. The application of injection waveforms causes ions outside the selected 30 to 42 Da mass range to disappear, while leaving most ions within the mass range: a) 0V injection waveform amplitude; b) 1V injection waveform amplitude; c) 2V injection waveform amplitude.

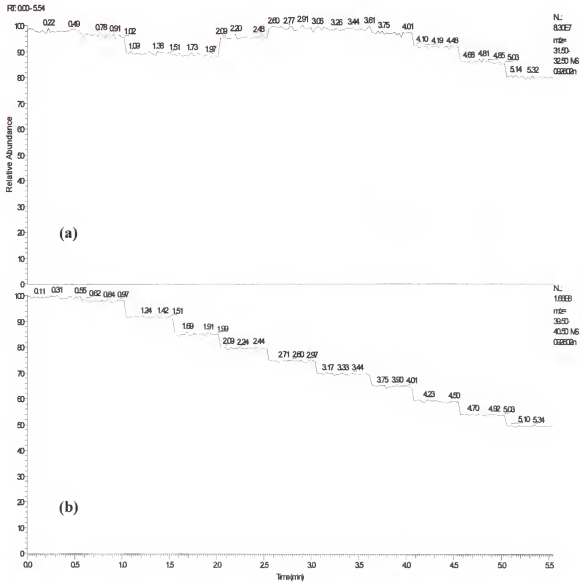


Figure 3-32. Effect of injection waveforms on analyte ion signals: a) 32 Da for oxygen ions; b) 40 Da for argon ions. The injection waveform amplitude was changed from 0.0 V to 1.0 V in 0.1 V increments every 30 s.

for either analyte; thus, detection of oxygen and argon does not improve with the use of injection waveforms (results for hydrogen and helium were not obtained, because calibration of the waveforms was not possible after the drive frequency was changed; results shown were acquired prior to any modifications).

Resonant ejection

The use of resonant ejection allows ions to be ejected in tighter packets. The fixed frequency signal applied to the endcaps brings ions into resonance at $q_z = 0.9016$, before the $\beta_z = 1$ boundary. The signal amplitude is ramped during mass analysis for optimal ion ejection. Figure 3-33b shows the effect of removing the resonant ejection waveform by setting the amplitude to 0 V. Peaks shift to higher mass as expected with the associated increase in ejection q , which delays the ejection of ions in time (corrected by mass calibrating). A more significant observation is the change in peak-widths. Table 3-1 shows the full-width half-maximum (FWHM) values for major peaks with and without resonantly ejection. The mean ΔFWHM is $0.026 \text{ Da} \pm 0.01$, which differs by 13% from the average FWHM of resonantly ejected ions ($0.195 \text{ Da} \pm 0.005$). Though 13% is a noticeable change, unit mass resolution is maintained, meeting is the AHGD project requirement. Peak heights increase by 10% when resonant ejection is turned off. This is favorable for the AHGD application that depends more on sensitivity than on mass resolution.

Injection waveforms and resonance ejection both worked by applying waveforms to the endcaps. This required additional RF circuitry that added to system volume, weight, and increased complexity (i.e., cost). Because neither appeared to provide any significant benefit for the AHGD application, the RF circuitry could be removed from the system, as was the case for the UF-IT.

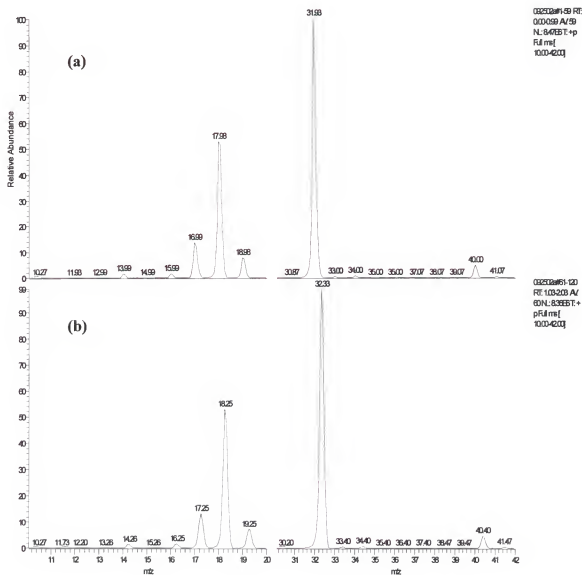


Figure 3-33. Mass spectra illustrating the effects of using resonant ejection: a) background spectrum with the use of resonant ejection (q_z eject 0.9016); b) same conditions, but without the use of resonant ejection (q_z eject 0.908, $\beta_z = 1$ boundary). The peaks shifted because the ions remained in the ion trap longer as the q_z eject was increased. Turning off resonant ejection increased peak widths by 13%, but unit mass resolution was maintained.

Table 3-1. Change in peak width with and without using resonant ejection; ± 0.005 Da error in FWHM assignments, and ± 0.01 Da error in Δ FWHM assignments.

m/z value of major ions	14	16	17	18	19	32	40
FWHM with resonance ejection (Da)	0.180	0.195	0.190	0.200	0.185	0.210	0.205
FWHM without resonance ejection. (Da)	0.215	0.210	0.220	0.220	0.220	0.230	0.235
Difference: Δ FWHM (Da)	0.035	0.015	0.030	0.020	0.035	0.020	0.030

PolarisQ modified for lightweight gas analysis

By changing the drive frequency to 2.82 MHz, the PolarisQ was able to mass analysis helium ions as shown in Figure 3-34a. This was in the presence of collision gas, but the observed helium ion signal was not as intense as expected, because of a combination of factors. First, the ionization efficiency for helium with 70 eV electrons was lower than that of the other species present. Second, helium ions upon entering the ion trap collided with neutrals of the same mass, which heats rather than cools the injected ions, reducing the trapping efficiently. Third, helium ions react quickly with other ambient gas neutrals (covered in Chapter 4).

Adding pure nitrogen to the ion source (Figure 3-34b) significantly suppressed (100 times less) the ion signal for larger background species (e.g., oxygen and argon); however, the helium ion signal was reduced only by 60%. This suggested that there was a significant helium pressure inside the ion source, a significant source of chemical noise for hydrogen and helium detection.

Detecting hydrogen ions with the PolarisQ

A hydrogen ion signal was not detected while using helium as the collision gas, either as a component of background gas (as seen with the UF-IT) or when sampling 2.5% hydrogen in nitrogen. With helium being twice the mass of a hydrogen molecule, injected hydrogen ions were scattered not stabilized.

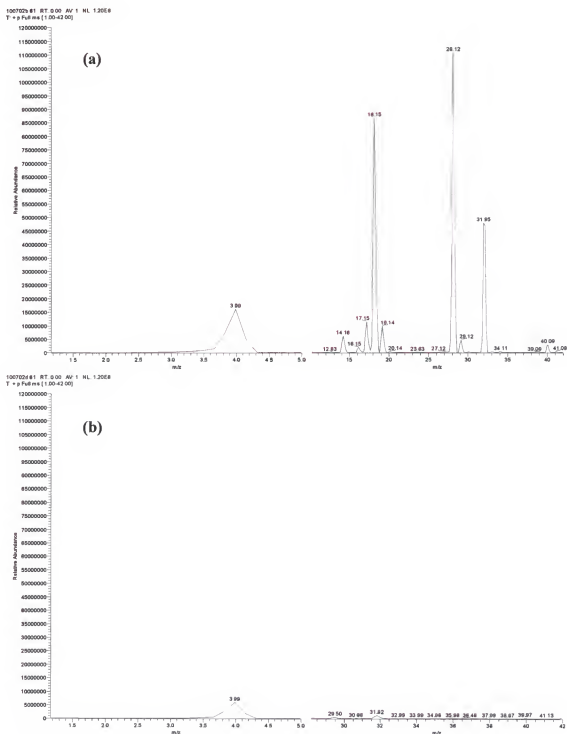


Figure 3-34. Mass spectra with the PolarisQ tuned to 2.82 MHz: a) background gas spectrum; b) pure nitrogen gas sampled. Helium ions from the collision gas are observed in both. The increased nitrogen pressure decreases the helium ion intensity by about 60%, but much less than the decrease of background ion signals (the mass range scaled up for oxygen and argon in (b)).

Using hydrogen as a collision gas would cause less scattering of hydrogen and also helium ions. Figure 3-35a shows the result of using hydrogen as the collision gas. An intense peak at 3 Da was observed, which was the protonated hydrogen molecule H_3^+ . No signal was detected at 2 Da, because the high pressure of hydrogen promotes complete protonation of the hydrogen molecule. Other observed ions at 19 and 29 Da were protonated forms of water and nitrogen, leaving only oxygen un-protonated (has lower proton affinity than hydrogen). The addition of pure nitrogen (Figure 3-25b) into the ion source did not significantly reduce the protonated hydrogen ion signal. When using the hydrogen collision gas, a response was not detected at either 2, 4, or 40 Da while the sample concentration was changed from pure nitrogen to 5000-ppm of each analyte in nitrogen (Figure 3-36). Only oxygen responded, since it did not react with hydrogen.

Conclusions

The assembled UF-IT and the modified PolarisQ were successfully modified to mass analyze lightweight gas ions. The UF-IT was constructed specifically for the AHGD application. It used internal ionization in the absence of a collision gas with an open ion trap configuration for rapid response, and was built into a compact size. The Polaris Q was used to explore the use of an external ionization source, injection waveforms, and resonant ejection, which were found to provide no significant benefit for the AHGD application. Results from both instruments pointed to the occurrence of ion-molecule reactions, which will be discussed in Chapter 4.

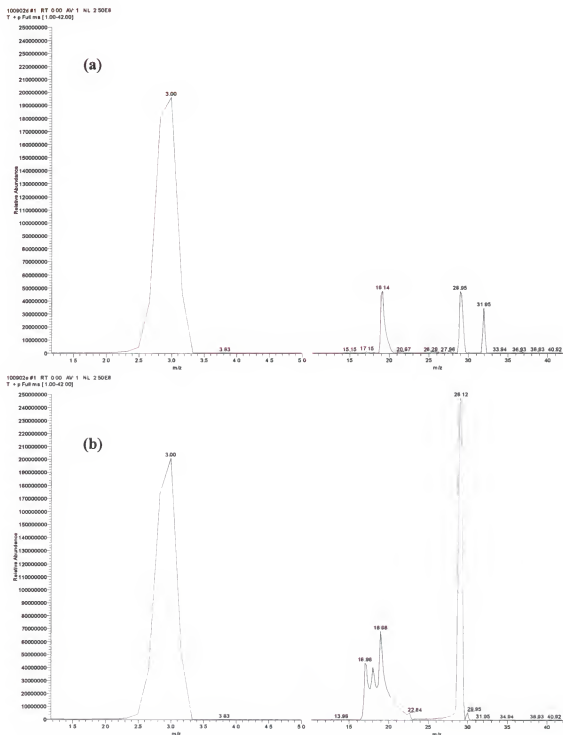


Figure 3-35. Hydrogen as the collision gas in the PolarisQ at 2.82MHz: a) background gas spectrum; b) pure nitrogen gas sampled. With hydrogen as the collision gas, a large 3 Da ion peak was observed as well as peaks at 19 and 29 Da, all products of protonation reactions (H_3^+ , H_3O^+ , HN_2^+ , respectively).

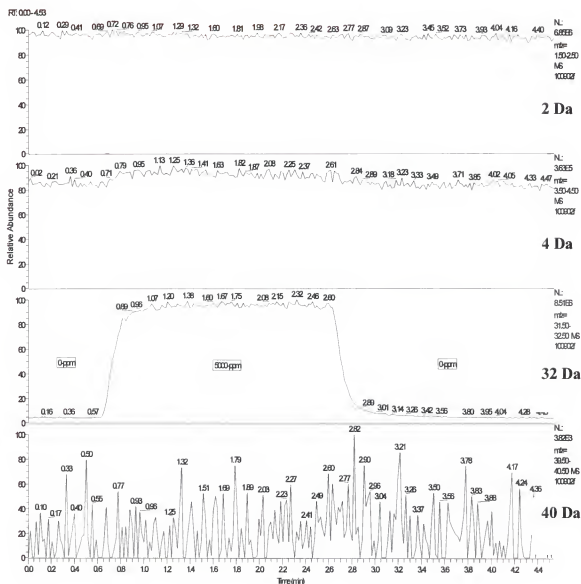


Figure 3-36. Use of a hydrogen collision gas when monitoring the AHGD-analyte ions while changing from pure nitrogen to 5000-ppm of each in nitrogen. The use of a hydrogen collision gas does not improve detection for hydrogen and helium, and eliminates detection for argon. Oxygen is the only analyte to respond, because it does not readily protonate.

CHAPTER 4 ION-MOLECULE REACTIONS: A LIMITATION OF QITMS

Introduction

In Chapter 3, evidence pointed to the occurrence of ion-molecule reactions inside the ion trap with the analytes of the NASA Advanced Hazardous Gas Detection (AHGD) project. Figure 3-28 showed ion signals at 3, 19, and 29 Da, which were $(M+H)^+$ ions of hydrogen, water, and nitrogen, respectively, formed by proton transfer reactions. These reactions were observed with mass spectrometry as early as 1916 when the H_3^+ ion was isolated at 3 Da.¹¹⁰ Since then, exploration of ion-molecule reactions has accelerated. In the 1950s, improving mass spectrometry technology and the advent of chemical ionization prompted further study of ion-molecule reactions. Three types of instruments were used: 1) tandem-in-space mass spectrometry (e.g., sector and triple quadrupole); 2) drift tube methods that used either spectroscopic or mass spectrometric detection; and 3) tandem-in-time mass spectrometers (e.g., FT-ICRMS and QITMS).¹¹¹ Tandem-in-space mass spectrometry controlled reactions by adjusting the gas pressure in the collision cell only. With the drift tube methods (e.g., selected ion flow tube, SIFT), reactions could only be studied at high pressure. Tandem-in-time had the advantage that ions were stored, thus reactions could be explored by changing both time and pressure.^{6,112} At a low pressure reactions were studied on a molecular rather than bulk scale.

Even before its commercialization, the QIT was used for studying gas phase reactions. The concept of the QUISTOR, first proposed by Todd^{34,35} (Chapter 1), was explicit for reaction studies, which led to the development of a low pressure CI source,

where time - not pressure - was used to provide a sufficient number of collisions. This was a concern for the AHGD application, since unwanted reactions would impact quantitative performance by changing analyte ion signals and chemical noise.

In this chapter ion-molecule reactions are explored between the AHGD analytes hydrogen, helium, oxygen, and argon and the background gasses, primarily nitrogen with lesser amounts of water, oxygen and hydrogen. The results provide a framework to customize QITMS for optimal performance with the AHGD application (Chapter 5).

Types of Ion-Molecule Reactions

With electron impact ionization, positive radical ions are formed by



when A collided with an electron of sufficient energy (electron energy > ionization energy of A).^{113,114} The number of ions formed by this process can be estimated by

$$[\sum A^{+\bullet}] \approx [e^-] \sigma_c N_A 2z_0 \quad (4-2)$$

which is valid at low pressure and at short distances: $[e^-]$ is approximated by the product of emission current and ionization time (off by a factor of 2 or 3), σ_c is the ionization cross-section of neutral A in $\text{cm}^2/\text{molecule}$, N_A is the number density of A in $\text{molecules}/\text{cm}^3$, and z_0 is the axial dimension of the ion trap in cm .¹¹⁵ The AHGD small elemental and diatomic species have small EI collisional cross sections, σ_c , each approximately a few angstroms. With a pressure of 7×10^{-6} torr and an emission current of $150 \mu\text{A}$, about 5×10^8 ions will form in 1 ms. For an analyte at 1 ppm, only 500 ions are formed, and during ejection only 50% of these leave through the exit endcap, leaving at best 250 ions or 0.5 pA of ion current for detection.

The average velocity of the ions formed can be determined from:

$$\langle \dot{u} \rangle = \frac{z_0 q_z \Omega}{\sqrt{2\pi}} \quad (4-3)$$

which is an estimate based on harmonic oscillation in the axial direction.⁷ From this equation an ion inside the UF-IT at a $q_z = 0.25$ would be moving at 6900 m/s, or 7 m/ms. At an ambient pressure of 7×10^{-6} torr the mean free path inside the UF-IT is also 7 m, which results in an ion colliding with a neutral once every millisecond. The few analyte ions formed will collide numerous times during the 10 to 20 ms storage time, and will be neutralized, given exothermic reaction conditions. Thus, of particular concern are those reactions with more abundant background gases such as nitrogen or water, since collisions with these species occur most often.

Charge-exchange reactions

One reaction pathway inside the QITMS is charge-exchange, which is generalized as



where an electron transfers from neutral B to the ion radical A.^{110,116-119} This process is exothermic when the recombination energy (RE) of A^+ is greater than the ionization energy (IE) of B; recombination and ionization energies for the species of interest are listed in Tables 4-1 and 4-2, respectively. RE and IE values are the same for atoms, but not for molecules, which can transfer collision energy into vibrational or rotational motion. Highly exothermic reactions can also cause fragmentation of B^+ .

Proton transfer reactions

Since the discovery in 1916 of H_3^+ ions, mass spectrometry has been used in the study of gas phase acid-base chemistry. The Brønsted acid H_3^+ is formed by proton transfer as generalized by the reaction pathway:



which is exothermic when the conjugate base B has a higher proton affinity (PA) than the acid AH^+ .^{110,117,121} The neutral form of an acid will have a higher PA than its ion, thus self-protonation will also occur. To determine absolute proton affinities, the heat of formation is calculated from the appearance potential of a fragment ion of the protonated species; however, this method works with few molecules.¹²² Thus, PA values of most compounds are reported relative to a few absolute values. Table 4-3 lists PA values for several molecules of interest, measured relative to absolute PA values of isobutene (196.9 kcal/mole) and ammonia (205.0 kcal/mole).¹²¹

Table 4-1. Recombination energies (RE) for ions of interest.¹¹⁷⁻¹¹⁹

Ions of interest	RE (eV)
H_2^+	16.4 - 17.4
H_3^+	9.2
He^+	24.6
H_2O^+	12.4
H_3O^+	6.4
N_2^+	15.3
N_2H^+	8.5
O_2^+	11.2 - 11.3
Ar^+	15.8

Table 4-2. Ionization energies (IE) for atoms and molecules of interest.¹²⁰

Atoms / molecules	IE (eV)
H_2	15.4
He	24.6
H_2O	12.6
N_2	15.6
O_2	12.1
Ar	15.8

Table 4-3. Proton affinities for molecules of interest.¹²¹

Molecules	PA (eV)
H_2	4.38
N_2	4.930
O_2	4.384
H_2O	7.501

Hydrogen-atom transfer

A third and less understood reaction involves the net transfer of a hydrogen atom from a neutral,^{117,123-127} expressed as



With self-protonation, where $A = B$, hydrogen atom transfer and proton transfer are indistinguishable.^{110,125} The energetics for hydrogen atom transfer are likely similar to proton transfer, but the exact mechanism is still in dispute. For some reactions, as in the case of $N_2^{+} + H_2$, the apparent homolytic cleavage of an H atom to form N_2H^{\cdot} is said to occur by a charge-exchange proton transfer combined reaction scheme, explained as a hopping mechanism that occurs when the ionization potentials of A and B are close and their vibrationally excited states resonate.^{123,124} This does not work for all A, B pairs. For example, charge transfer between $CO^{+} + H_2$ is endothermic by more than 1 eV, so the formation of COH^{\cdot} must occur by a different method, potentially by direct transfer of the hydrogen atom.¹²⁶

Kinetics of Ion-Molecule Reactions

The reality with QITMS is that stored ions will react given exothermic conditions and enough time. Studying reactions between analytes and resident neutrals becomes important in determining the effectiveness of the instrument for the selected application. The QITMS is useful in studying these reactions, since the instruments scanning rate and the collision rate are comparable. Kinetics of ion-molecule reaction can be explored by adjusting the ion storage time from a few milliseconds for faster reactions to several seconds for slower ones.^{115,128,129}

All of the aforementioned reaction types can be generalized as



where m and n can be any number of product ions and neutrals, respectively. The rate that A^+ disappears can be determined from the rate constant k and the amounts of reactant ion and neutral using the rate equation:

$$\frac{d[A^+]}{dt} = -k[A^+][B] \quad (4-8)$$

which is considered pseudo-first-order for reactions in a QITMS where $[A^+] \ll [B]$.

Integration of Equation 4-8 as first-order gives

$$\ln \frac{[A^+]_t}{[A^+]_0} = -kt[B] \quad (4-9)$$

where the ratio between the initial concentration, $[A^+]_0$, and final concentration, $[A^+]_t$, is replaced by a ratio of initial and final ion signal. Solving Equation 4-9 for k gives

$$k = -\ln \frac{[A^+]_t}{[A^+]_0} \times \frac{1}{t[B]} \quad (4-10)$$

which used with a plot of the ion signal ratios at different reaction times can be used to determine the rate constant if [B] is known, or vice-versa. Equation 4-10 can also be written as the exponential expression:

$$[A^+]_t = [A^+]_0 e^{-k[B]t} \quad (4-11)$$

which is helpful for determining a final concentration of A^+ . Thus, for quantitative applications, it is useful to know the speed at which the analyte ions of interest are reacting. The overall significance of a reaction can be approximated by the magnitude of the rate constant, where values on the order of $10^{-9} \text{ cm}^3/\text{s} \cdot \text{molecule}$ are typical for fast reactions.^{127,130}

The ion-induced dipole collisional rate theory, first presented by Langevin, can be used to approximate a rate constant.^{110,131} The reacting ion and neutral are considered simple particles that have no internal energy, which approach one another at a relative velocity v with a total system energy $E_r = 1/2\mu v^2$, where μ is the reduced mass (in g), $(m_i m_n)/(m_i + m_n)$. The approaching ion with charge q induces a dipole on a nonpolar neutral having a polarizability of α (in cm³). This results in a collision cross section of σ_c (in cm²):

$$\sigma_c(v) = \left(\frac{2\pi q}{v} \right) \left(\frac{\alpha}{\mu} \right)^{\frac{1}{2}} \quad (4-12)$$

that when multiplied with the relative velocity (v in cm/s) gives the estimated rate constant:

$$k_L = v \sigma_c(v) = 2\pi q \left(\frac{\alpha}{\mu} \right)^{\frac{1}{2}} \quad (4-13)$$

otherwise known as the Langevin rate constant. Equation 4-13 works with nonpolar neutrals, which most AHGD analytes and background gasses are, except for water that has a significant dipole, μ_D (in cm²•g/s²•K), that increases the collisional cross section. This is accounted for in the average dipole orientation (ADO) theory, where the rate constant is approximated as

$$k_{ADO}(T) = \left(\frac{2\pi q}{\sqrt{\mu}} \right) \left[\sqrt{\alpha} + C\mu_D \left(\frac{2}{\pi kT} \right)^{\frac{1}{2}} \right] \quad (4-14)$$

which is dependent on the absolute temperature T in K (k is Boltzmann's constant). The value C is a dipole-locking constant that is dependent on the value $(\mu_D/\sqrt{\alpha})$, which for water is 0.25 at 300K (taken from Figure 3 of reference 110, p. 12; dipole moment and

polarizability values were taken from reference 120).^{110,131,132} The approximate k values of these two theories provide a reference point for evaluating the accuracy of the measured reaction rates.

Thermodynamics of Ion-Molecule Reactions

The adaptability of the QITMS to control kinetic ion-molecule reactions can at times be undermined because of presence of a reactive species at high concentration, which is the case for water when the mass spectrometer is first turned on. Product ions observed under such conditions are at thermodynamic equilibrium, which can be induced at lower pressure by increasing the ion-reaction time.

Ion-molecule reactions at thermodynamic equilibrium can be generalized by^{121,122,129}



which can be expressed in terms of an equilibrium constant k_{eq} as

$$k_{eq} = \frac{k_f}{k_r} = \frac{[C^+][D]}{[A^+][B]} \quad (4-16)$$

where the ion signal ratio of C^+ to A^+ can be substituted for the concentration ratio, and the neutral concentration ratio of $[D]/[B]$ remains constant, since many more neutrals exist than ions. The equilibrium constant can also be determined from

$$-RT \ln k_{eq} = \Delta G = \Delta H - T\Delta S \quad (4-17)$$

and for charge-exchange reactions $\Delta H = IE(B) - RE(A^+)$.

Equation 4-16 is particularly useful in the case of proton transfer reactions:



where the change in gas-phase basicity (GB) equals the free energy at temperature T ($-\Delta G$) for the protonation of an ion, and the change in proton affinity equals the reaction enthalpy ($-\Delta H$):

$$\begin{aligned} -\Delta G &= GB(N) - GB(M) \\ -\Delta H &= PA(N) - PA(M) \end{aligned} \quad (4-19)$$

Equipment and Methods

In this chapter we report on reactions between AHGD analyte ions and background gases (i.e., nitrogen, water, etc.). Pure gas standards were used for hydrogen, helium, and argon, while oxygen ions from the background gas were studied to avoid the handling concerns of pure oxygen. The next sections discuss the gas delivery method, the method of determining neutral gas density, and a description of QITMS operational parameters.

Gas Delivery Setup

The gas standards produced by BOC Gases were 99.99% pure. Two-stage cylinder regulators were used to provide a constant output pressure of 20 PSIG, and Swagelok QC series quick-disconnect fittings allowed rapid switching of gas lines (1/8 in. stainless steel).

One gas stream was admitted by the main inlet of the UF-IT (Figure 4-1) using the GDS mixing apparatus detailed in Chapter 3. The gas went through a 1000-sccm MFC that was set to full-open. The exhaust needle valve was left closed to pressurize the plenum to 20 PSIG. The Varian SH-100 scroll pump drew a side stream from the plenum through a Granville-Phillips 203 leak valve that regulated the pressure at the 0.001 in. inlet orifice. The gas then entered the vacuum chamber via the transfer line, which exhausted between the ring electrode and the exit endcap into the ion trap.

A second gas stream was admitted through the auxiliary port, controlled by a Granville-Phillips 203 leak valve, directly from the gas-cylinder regulator. This gas flow proved more difficult to control, because the high-pressure differential across the 203 leak valve required a low conductance, significantly increasing the time needed to switch gases. The small conductance also tended to drift because of condensed water, which was lessened by an overnight bake-out at 200 °C.

Number Density Determination

Evaluation of reaction kinetics required accurate determination of the reactant neutral's number density within the ion trap, which assuming a uniform Boltzmann distribution is determined from:

$$N_d = \frac{C}{k} \times \frac{P}{T} \quad (4-20)$$

where N_d is the number density in molecule/cm³ of a gas at a partial pressure of P in torr. The constant $C = 1.33 \times 10^{-4}$ converts torr to Pascal and m to cm; k is Boltzmann's constant and T is the manifold temperature reported in K.

An accurate measure of the reactant gas pressure was most significant for the calculation.¹²⁹ As a pure gas was admitted into the vacuum chamber, the attached ion gauge responded because of the increased ion current formed. Response tables were used to determine the partial pressure of the gas, which is shown on a two-digit display that is calibrated for nitrogen. Correction factors found in Table 4-4 were required to adjust for ionization differences of other gases.

A second correction was needed for gas samples delivered by the main inlet. The inlet transfer line exhausted directly into the ion trap volume where the pressure was

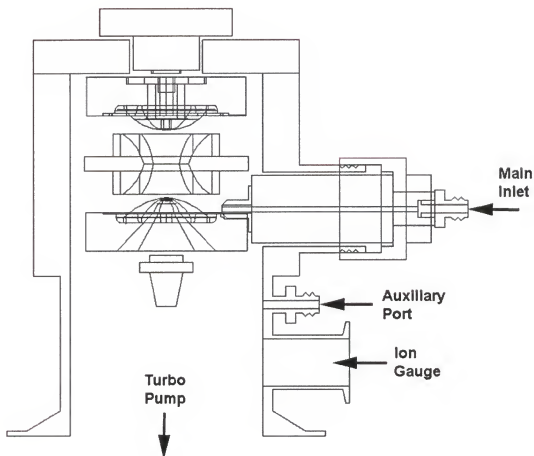


Figure 4-1. Diagram of the UF-IT vacuum chamber. Two gas streams were available for ion-molecule reactions studies. First, gas supplied by the GDS (described in Chapter 3) passed through a 0.001 in. orifice and traveled down the transfer line of the main inlet, which exhausted between the ring and exit endcap electrodes into the ion trap. The second was a gas stream supplied directly from a regulated gas cylinder (20 PSIG) through a Granville-Phillips 203 leak valve that entered through the auxiliary port. An ion gauge was attached to the chamber by a 0.5 in. i.d. pipe with a 90° bend.

higher than that measured at the ion gauge, which was further away. The same issue was not observed for gas admitted through the auxiliary port, because gas more uniformly diffused into the ion trap and ion gauge since both were situated away from the port outlet.

To correct for the difference, a gas was admitted through the auxiliary port, then through the inlet at different pressures as the ion signals were recorded. Correlation charts (Figures 4-2, 4-3, and 4-4) were generated from which the main inlet pressure correction factors reported in Table 4-4 were determined.

Table 4-4. Correction factors for partial pressure measurements (multiply the ion gauge reading by the given factor).

GAS SPECIES	Ion gauge	Inlet
Hydrogen	2.174	1.206
Helium	6.667	--
Nitrogen	1	2.465
Argon	0.840	2.594

Custom Scan Functions

QITMS operation was customized for experiments with each of the four-analyte ions. The scan function for use with helium ions is shown in part A of Figure 4-5. First the RF amplitude was held a low RF amplitude, 104 V_p, placing 4 Da at a $q_z = 0.363$ for a 1 ms ionization period. The RF amplitude was then increased to place 4 Da just inside the stability boundary at a $q_z = 0.907$, which subsequently provided better trapping conditions for the higher mass product ions (e.g., 14, 18, and 28 Da) that were collected during the reaction period (varied from 0 to 30 ms in 14 steps). The RF amplitude was then ramped for the analytical scan to detect ions between 4 and 32 Da.

The scan function used with hydrogen ions is shown in Figure 4-5 part B. As with helium, a low RF amplitude (78 V_p) was required during the 1 ms hydrogen ionization

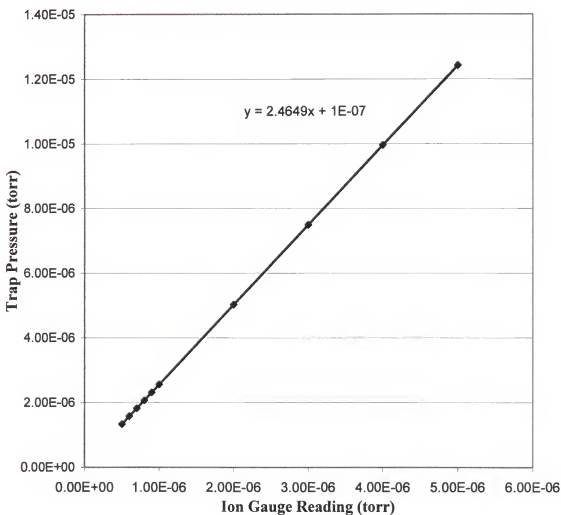


Figure 4-2. Nitrogen correction factor plot. The pressure increase on the ion gauge is multiplied by the correction factor of 2.465 to determine the partial pressure of nitrogen inside the ion trap when the main inlet is used to deliver the gas.

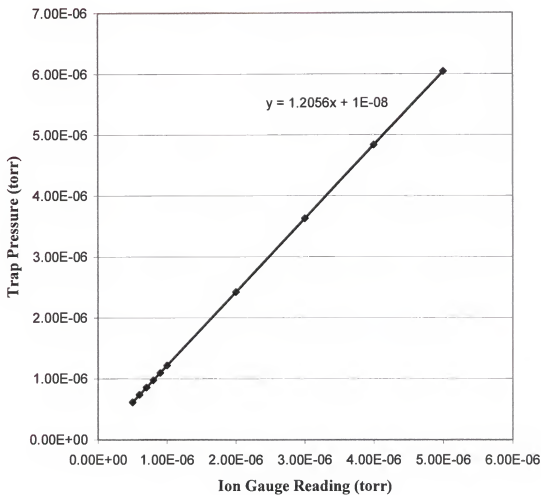


Figure 4-3. Hydrogen correction factor plot. The pressure increase on the ion gauge is multiplied by the correction factor of 1.206 to determine the partial pressure of hydrogen inside the ion trap when the main inlet is used to deliver the gas.

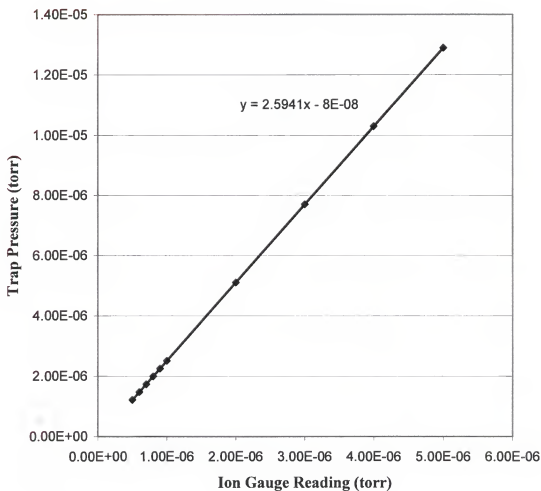


Figure 4-4. Argon correction factor plot. The pressure increase on the ion gauge is multiplied by the correction factor of 2.594 to determine the partial pressure of argon inside the ion trap when using the chamber's main inlet.

period; however, it was not possible to store hydrogen ions and the larger product ions together during the reaction period. Only the self-protonation product ion at 3 Da was low enough in mass to be monitored. The reaction period was varied between 0 and 40 ms in 14 steps with an analytical scan from 2 to 5 Da.

Figure 4-6 shows the scan functions for higher mass species. The reaction between argon ions and ambient water was explored using the scan function in part A. Since nitrogen was not added, the argon pressure was increased to 7×10^{-6} torr to match that used for the AHGD application. A short ionization period of 0.1 ms minimized space charge at the high analyte pressure. Argon ions were kept at a low q_z of 0.091 to trap lower mass product ions during the reaction period, which was stepped from 0 and 60 ms in 10 intervals. Ions between 10 and 45 Da were mass analyzed.

Part B of Figure 4-6 shows the scan function used to determine the thermodynamic end products of ionized background gas. A longer ionization period of 5 ms was required at the low background pressure to produce an adequate ion signal. The reaction period was varied from 0 to 4000 ms over 9 steps, long enough to ensure that thermodynamic equilibrium was reached. Ions between 10 and 45 Da were mass analyzed.

Ion-Molecule Reaction Results

He⁺ Reactions

The dynamics between reactant helium ions and background neutrals are illustrated in Figure 4-7. The helium ion signal decreased rapidly as signals for nitrogen ions increased, N⁺ at 14 Da and N₂⁺ at 28 Da. The reaction was exothermic, $-\Delta H = 9$ eV, with enough energy to break apart the diatomic bond (strength of 9 eV^{120}), explaining

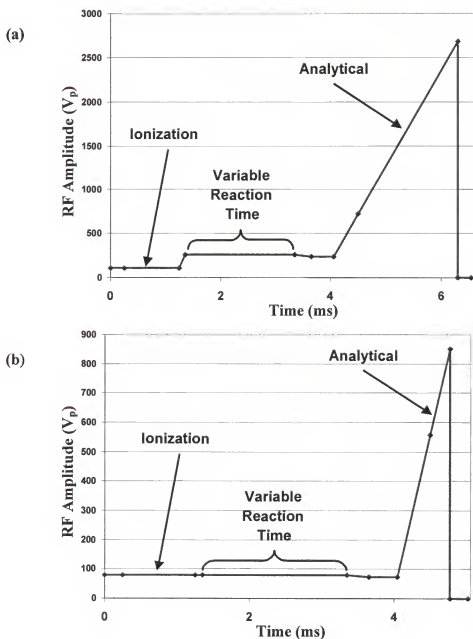


Figure 4-5. QITMS scan functions for low-mass ions. a) Helium ions were collected during a 1 ms ionization period, and then reacted with background gas (predominantly nitrogen) over a variable reaction period. Product ions were mass analyzed between 4 and 32 Da. b) Hydrogen ions collected over a 1 ms ionization period were reacted with hydrogen neutrals, forming protonation products, which were mass analyzed between 2 and 5 Da.

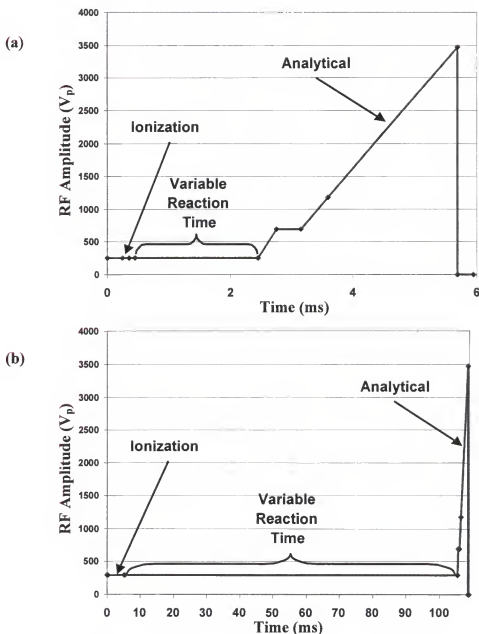


Figure 4-6. QITMS scan function for higher mass ions. a) Argon ions collected over a 0.1 ms ionization period were reacted with ambient water during a variable reaction period, and product ions were mass analyzed between 10 and 45 Da. The scan function was also used in an experiment to estimate the ambient water concentration inside the vacuum chamber. b) The end products of ion-molecule reactions between background gases were determined by using long reaction times (up to 4 s) which allowed thermodynamic equilibrium to be established.

the observed production of both atomic and molecular ions. The increasing water ion signal at 18 Da, which was unaffected when the helium ions were exhausted, was because of reactions with nitrogen ions. The hydronium ion signal at 19 Da increased as more water ions were formed. Charge-exchange between helium ions and water neutrals was not observed at 18 Da, because the reaction was highly exothermic at 12 eV, and fragmentation of the 5 eV hydrogen-oxygen bond occurred. The oxygen ion signal at 32 Da increased, since most ions will charge-exchange with oxygen. Protonated nitrogen at 29 Da also increased because of reaction with hydrogen in the background.

The results from three repetitions of helium ions reacting with nitrogen neutrals are reported in Table 4-5. The reaction rate was derived from similar plots to that shown in Figure 4-8, which is the average of the three runs. The rate constant was determined using Equation 4-10, but was limited to two-digit precision because of the ion gauge display. The calculated k agreed well with the Langevin estimation of $k_L = 1.7 \times 10^{-9} \text{ cm}^3/\text{s}\cdot\text{molecule}$, and with the FT-ICR literature value of $k = 1.75 \times 10^{-9} \text{ cm}^3/\text{s}\cdot\text{molecule}$ ¹³³ Values from drift-tube experiments were lower however, ranging from 1.2×10^{-9} to $1.5 \times 10^{-9} \text{ cm}^3/\text{s}\cdot\text{molecule}$.¹³³

Table 4-5. Repetitive ion-molecule reaction experiments between He^+ and N_2 .

Criteria	Run 1	Run 2	Run 3
Chamber temperature (K)	302	302	302
Background (BG) pressure (torr)	5.8×10^{-7}	5.8×10^{-7}	5.7×10^{-7}
He pressure - aux. port (torr)	2.7×10^{-7}	2.6×10^{-7}	2.5×10^{-7}
N_2 pressure – main inlet (torr)	7.4×10^{-6}	7.4×10^{-6}	7.4×10^{-6}
N_d of added N_2 (molecule/ cm^3)	2.4×10^{11}	2.4×10^{11}	2.4×10^{11}
N_d of BG (molecule/ cm^3)	1.9×10^{10}	1.9×10^{10}	1.8×10^{10}
Reaction rate ($-\ln \Delta \text{He}^+/\text{s}$)	421	412	410
k using N_2 only ($\text{cm}^3/\text{s}\cdot\text{molecule}$)	1.8×10^{-9}	1.8×10^{-9}	1.7×10^{-9}
k N_2 + 50% BG ($\text{cm}^3/\text{s}\cdot\text{molecule}$)	1.7×10^{-9}	1.7×10^{-9}	1.7×10^{-9}

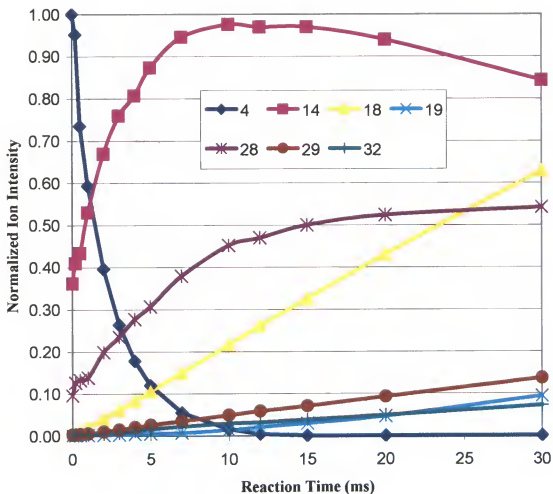


Figure 4-7. Ion intensities versus reaction time for the reaction of He^{++} and background gases. With partial pressure of helium at 2.7×10^{-6} torr, nitrogen at 7.4×10^{-6} torr, and the background gas at 5.8×10^{-7} torr, the helium ion signal decreased rapidly (50% within 1.8 ms) as ion signals for nitrogen increased. The nitrogen ions in turn reacted with ambient water, increasing the ion signal at 18 Da. Water ions self-protonated forming hydronium ions at 19 Da.

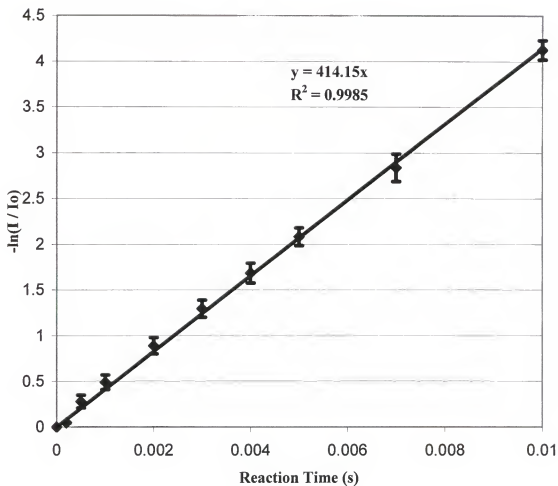


Figure 4-8. Plot of the change in helium ion signal versus reaction time. Data points are the average of three repetitive runs, with error bars of 1σ .

A second k value is reported that took account of the extra nitrogen gas in the chamber background. Air was being leaked into the chamber from the inlet block, which was rough pumped to only 20 mtorr. The leak increased the chamber pressure from a base of 2×10^{-8} torr to the background level of 6×10^{-7} torr. Nitrogen was the major component, but was estimated at only 50% from the background mass spectrum, because water is also abundant under high-vacuum conditions, since it condenses on metal surfaces.¹³⁴ Oxygen was the third major component at $\frac{1}{4}$ the concentration of nitrogen (air ratio). Other minor components included hydrogen, carbon monoxide, and carbon dioxide that evolved from the stainless steel, and argon from air. Because the added nitrogen was much greater than that in the background, the new rate constant was just slightly lower than before; however, the background gas would have more of an impact in later experiments.

The effects of changing the helium or nitrogen pressure were studied, and the results are shown in Tables 4-6 and 4-7, respectively. Changing the helium pressure had a minor effect on the reaction rate, with only a slight change of $< 5\%$ at half or twice the pressure, was explained by changes in the collisional cooling rate. In contrast, the nitrogen pressure had a significant impact on the reaction rate with up to a 39% increase with 1.33 times the nitrogen pressure. In either case, the rate constant remained unchanged at $1.8 \pm 0.1 \times 10^{-9} \text{ cm}^3/\text{s}\cdot\text{molecule}$. Collectively, these results verified that the ion-molecule reaction was pseudo-first order.

In the next experiment, the helium and nitrogen gas plumbing were reversed such that helium now went through the main inlet and nitrogen through the auxiliary port. Three repetitive runs were made using the new configuration with the results shown in

Table 4-8. The reaction rate increased slightly with an average of 427, which was 3% higher than the earlier average of 414. This was because of the higher nitrogen gas pressure, (7.6×10^{-6} torr compared with 7.4×10^{-6} torr earlier. The rate constant remained unchanged, which indicated that experimental results were unaffected by the plumbing configuration. This also validated the main inlet pressure correction factor, which was later assumed for all other experiments.

Table 4-6. Ion-molecule reactions at different He pressures between He^{++} and N_2 .

Criteria	Averages of Table 4-5	Half He pressure	Twice He pressure
Chamber temperature (K)	302	302	302
BG pressure (torr)	5.8×10^{-7}	5.7×10^{-7}	5.7×10^{-7}
He pressure – aux. port (torr)	2.6×10^{-7}	1.3×10^{-7}	5.3×10^{-7}
N_2 pressure – main inlet (torr)	7.4×10^{-6}	7.4×10^{-6}	7.4×10^{-6}
N_d of added N_2 (molecule/ cm^3)	2.4×10^{11}	2.4×10^{11}	2.4×10^{11}
N_d of BG (molecule/ cm^3)	1.9×10^{10}	1.8×10^{10}	1.8×10^{10}
Reaction rate ($-\ln \Delta \text{He}^+/s$)	414	409	437
k using N_2 only ($\text{cm}^3/\text{s} \cdot \text{molecule}$)	1.8×10^{-9}	1.7×10^{-9}	1.8×10^{-9}
k N_2 + 50% BG ($\text{cm}^3/\text{s} \cdot \text{molecule}$)	1.7×10^{-9}	1.7×10^{-9}	1.8×10^{-9}

Table 4-7. Ion-molecule reaction at different N_2 pressures between He^{++} and N_2 .

Criteria	Averages of Table 4-5	2/3 N_2 pressure	4/3 N_2 pressure
Chamber temperature (K)	302	302	302
BG pressure (torr)	5.8×10^{-7}	5.7×10^{-7}	5.7×10^{-7}
He pressure – aux. port (torr)	2.6×10^{-7}	2.6×10^{-7}	2.6×10^{-7}
N_2 pressure – main inlet (torr)	7.4×10^{-6}	4.9×10^{-6}	9.9×10^{-6}
N_d of added N_2 (molecule/ cm^3)	2.4×10^{11}	1.6×10^{11}	3.2×10^{11}
N_d of BG (molecule/ cm^3)	1.9×10^{10}	1.8×10^{10}	1.8×10^{10}
Reaction rate ($-\ln \Delta \text{He}^+/s$)	414	296	574
k using N_2 only ($\text{cm}^3/\text{s} \cdot \text{molecule}$)	1.8×10^{-9}	1.9×10^{-9}	1.8×10^{-9}
k N_2 + 50% BG ($\text{cm}^3/\text{s} \cdot \text{molecule}$)	1.7×10^{-9}	1.8×10^{-9}	1.8×10^{-9}

The results show that helium ions reacted quickly with nitrogen. The half-life of helium ions was 1.8 ms at room temperature and a nitrogen pressure of 7×10^{-6} torr. Thus, most helium ions would be neutralized during the scan, significantly reducing the S/N.

Table 4-8. Ion-molecule reaction with reversed gas lines between He^+ and N_2 .

Criteria	Run 1	Run 2	Run 3
Chamber temperature (K)	297	297	297
BG pressure (torr)	5.5×10^{-7}	5.5×10^{-7}	5.5×10^{-7}
He pressure – main inlet. (torr)	1.3×10^{-7}	1.3×10^{-7}	1.2×10^{-7}
N_2 pressure – aux. port (torr)	7.6×10^{-6}	7.6×10^{-6}	7.6×10^{-6}
N_d of added N_2 (molecule/ cm^3)	2.5×10^{11}	2.5×10^{11}	2.5×10^{11}
N_d of BG (molecule/ cm^3)	1.8×10^{10}	1.8×10^{10}	1.8×10^{10}
Reaction rate ($-\ln \Delta \text{He}^+/\text{s}$)	431	427	424
k using N_2 only ($\text{cm}^3/\text{s} \cdot \text{molecule}$)	1.8×10^{-9}	1.7×10^{-9}	1.7×10^{-9}
k $\text{N}_2 + 50\%$ BG ($\text{cm}^3/\text{s} \cdot \text{molecule}$)	1.7×10^{-9}	1.7×10^{-9}	1.7×10^{-9}

H_2^+ Self-Protonation and Other Reactions

The reactions of hydrogen ions with nitrogen were more difficult to study since both proton transfer and charge-exchange occurred, each being exothermic by 0.55 eV and 0.8 to 1.8 eV, respectively. In addition, product ions could not be stored with the hydrogen ions, because of the large mass difference (consider that helium is twice the mass of the hydrogen molecule, and that q_z is proportional to mass). A competing reaction involved the self-protonation of hydrogen to form H_3^+ , which was low enough in mass to be monitored. Thus, the self-protonation reaction was examined alone by only adding hydrogen gas (Figure 4-9). The reaction was rapid (rate plot shown in Figure 4-10) with a large rate constant of $3.3 \times 10^{-9} \text{ cm}^3/\text{s} \cdot \text{molecule}$. This k value did not match either the Langevin approximation of $k_L = 2.1 \times 10^{-9} \text{ cm}^3/\text{s} \cdot \text{molecule}$, or the literature values which ranged from 2.08 to $2.12 \times 10^{-9} \text{ cm}^3/\text{s} \cdot \text{molecule}$ ¹³³. The value was high because hydrogen ions were also neutralized by reactions with background species, including: nitrogen, $k = 2.8 \times 10^{-9} \text{ cm}^3/\text{s} \cdot \text{molecule}$; water, $k = 5.37 \times 10^{-9} \text{ cm}^3/\text{s} \cdot \text{molecule}$; and oxygen, $k = 7.56 \times 10^{-9} \text{ cm}^3/\text{s} \cdot \text{molecule}$. Each had a greater rate constant than the self-protonation reaction, which increased hydrogen ion loss, and elevated the total rate constant.

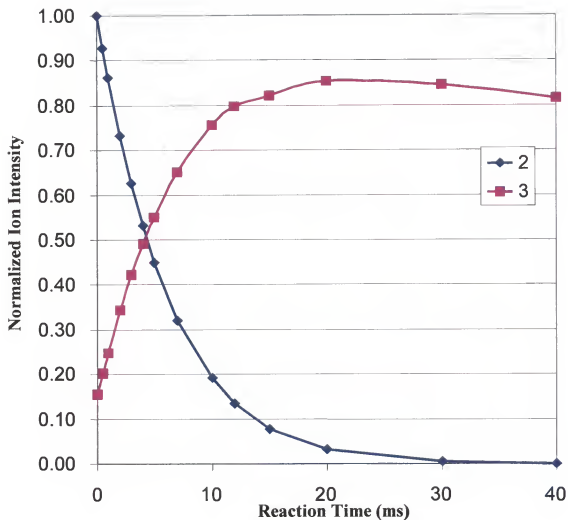


Figure 4-9. Ion intensity versus reaction time for the self-protonation reaction of H_2 to form the H_3^+ ion at 3 Da. At a hydrogen pressure of 1.6×10^6 torr, 50% of the hydrogen ion signal was lost after 4.5 ms, as the self-protonation product was formed. Other reactions occurred with background species, but the product ions were unable to be detected.

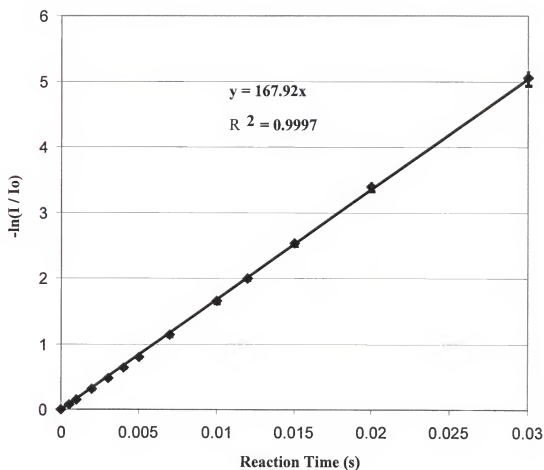


Figure 4-10. Plot of the change in hydrogen ion signal versus reaction time. Data points are the average of three repetitive runs, with error bars of 1σ .

The k value was not corrected when adding the extra background pressure alone, because the individual reactions had different rate constants. This can be accounted for by using the reaction:

$$(N_D \cdot k)_{\text{Total}} = \sum_1^n (N_D \cdot k)_n \quad (4-21)$$

which is useful if the number densities of each gas were accurately known. Since this was not the case, an alternate means for determining the self-protonation k value was used, which involved H_3^+ since

$$k = -\ln \left(1 - \frac{[H_3^+]_t}{[H_3^+]_0} \right) \times \frac{1}{[H_2]t} \quad (4-22)$$

which was valid in this case because the product ion was exclusively produced by self-protonation. The H_3^+ appearance rate (Table 4-9) was slower than the hydrogen ion loss, since no competing reactions were involved. The rate constant of 2.2×10^{-9} $\text{cm}^3/\text{s} \cdot \text{molecule}$ closely matched the expected values, off by 1×10^{-10} because hydrogen in the background gas was not accounted for.

Table 4-9. Self-protonation reaction results for hydrogen; three replicate runs.

Criteria	Run 1	Run 2	Run 3
Chamber temperature (K)	297	297	297
BG pressure (torr)	3.8×10^{-7}	3.8×10^{-7}	3.8×10^{-7}
H_2 pressure – main inlet (torr)	1.6×10^{-6}	1.6×10^{-6}	1.6×10^{-6}
N_d of added H_2 (molecule/ cm^3)	5.2×10^{10}	5.2×10^{10}	5.2×10^{10}
N_d of BG (molecule/ cm^3)	1.2×10^{10}	1.2×10^{10}	1.2×10^{10}
Reaction rate ($-\ln \Delta H_2^+ / s$)	167	167	169
k using H_2 only ($\text{cm}^3/\text{s} \cdot \text{molecule}$)	3.3×10^{-9}	3.3×10^{-9}	3.3×10^{-9}
k H_2 + BG ($\text{cm}^3/\text{s} \cdot \text{molecule}$)	2.6×10^{-9}	2.6×10^{-9}	2.7×10^{-9}
Reaction rate ($-\ln(1 - \Delta H_3^+) / s$)	118	115	120
k using H_2 only ($\text{cm}^3/\text{s} \cdot \text{molecule}$)	2.2×10^{-9}	2.2×10^{-9}	2.3×10^{-9}

Though self-protonation limited sensitivity for hydrogen detection, reactions with nitrogen were more of a concern since it was at a much higher concentration. To

evaluate these reactions, hydrogen ion loss was monitored at five different nitrogen pressures; the results are reported in Table 4-10 with reaction rate plots shown in Figure 4-11. Rate constants were determined at each pressure using Equation 4-21. The average, $2.7 \times 10^{-9} \text{ cm}^3/\text{s-molecule}$, was close to the literature value of $2.8 \pm 0.2 \times 10^{-9} \text{ cm}^3/\text{s-molecule}$,¹³³ but higher than the approximation $k_L = 2.3 \times 10^{-9} \text{ cm}^3/\text{s-molecule}$

Table 4-10. Hydrogen ion-molecule reaction at different N₂ pressures.

Criteria	1 st N ₂ pressure	2 nd N ₂ pressure	3 rd N ₂ pressure	4 th N ₂ pressure
Chamber temperature (K)	297	297	297	297
BG pressure (torr)	3.5×10^{-7}	3.5×10^{-7}	3.5×10^{-7}	3.5×10^{-7}
H ₂ pressure – main inlet (torr)	1.6×10^{-6}	1.6×10^{-6}	1.6×10^{-6}	1.6×10^{-6}
N ₂ pressure – aux. port (torr)	1.0×10^{-6}	2.0×10^{-6}	3.0×10^{-6}	3.9×10^{-6}
Reaction rate ($-\ln \Delta H_2^+/s$)	260	342	423	489
k of H ₂ ⁺ + N ₂ (cm ³ /s-molecule)	2.8×10^{-9}	2.7×10^{-9}	2.6×10^{-9}	2.6×10^{-9}

As reported in Chapter 3, ion-molecule reactions were evident when hydrogen was used as the PolarisQ collision gas. In Figure 3-35 the 3 Da peak was prominent both before and after adding nitrogen, since at the high hydrogen pressure the self-protonation reaction occurred rapidly, and all hydrogen ions were exhausted before mass analysis occurred. Observed ion signals, except that of oxygen, were all of protonated species formed by either proton transfer or hydrogen atom transfer. This prevented monitoring of analyte ions. Even though the UF-IT did not use a high hydrogen pressure, reactions with hydrogen ions still limited analytical performance. At a nitrogen pressure of 7×10^{-6} torr, half of the hydrogen ions were lost after 1.1 ms, less than one-tenth the time required for the entire scan.

N₂⁺ Reacting with H₂O

Water having the highest proton affinity of the involved gases was also involved in proton transfer and hydrogen atom transfer reactions,. Water also had a low ionization

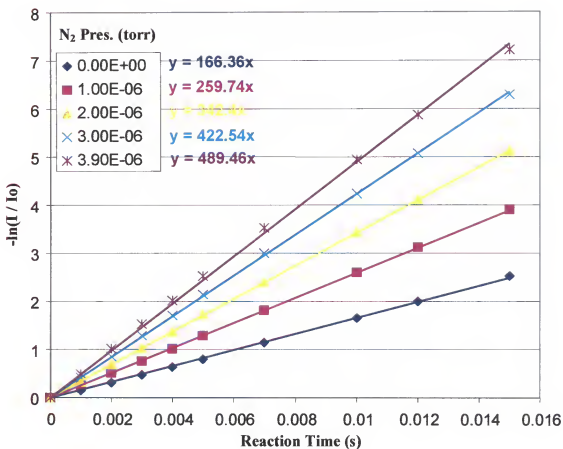


Figure 4-11. Five plots of the change in hydrogen ion signal versus reaction time, each with a different partial pressure of nitrogen added to the ion trap.

energy, allowing most other ions (except oxygen) to charge-exchange readily. Thus, a high water concentration would adversely affect analytical performance.

Mass spectra suggested that the background was 35% water. To verify this, the reaction between nitrogen ions and ambient water was studied (results reported in Table 4-11). The reaction rate was slow because of the low water concentration. Using a rate constant of $2.3 \times 10^{-9} \text{ cm}^3/\text{s} \cdot \text{molecule}$, the average of reported literature values,¹³³ the calculated water partial pressure was $1.3 \times 10^{-7} \text{ torr}$, or 32.5% of the background gas, which agreed with the earlier approximation. This pressure was then used in the next set of experiments.

Table 4-11. Determination of water vapor pressure via reaction with N_2^+ ; three replicate runs.

Criteria	Run 1	Run 2	Run 3
Chamber temperature (K)	297	297	297
BG pressure (torr)	4.0×10^{-7}	4.0×10^{-7}	4.0×10^{-7}
N_2 pressure – aux. port (torr)	7.2×10^{-6}	7.1×10^{-6}	7.0×10^{-6}
N_d of BG (molecule/ cm^3)	1.3×10^{10}	1.3×10^{10}	1.3×10^{10}
Reaction rate ($-\ln \Delta \text{H}_2^+/\text{s}$)	10.1	9.75	9.70
N_d of H_2O (molecule/ cm^3)	4.4×10^9	4.2×10^9	4.2×10^9
H_2O pressure (torr)	1.4×10^{-7}	1.3×10^{-7}	1.3×10^{-7}

Ar^+ Reactions

The ion-molecule reaction of argon ions with nitrogen was marginally exothermic ($-\Delta H = 0.2 \text{ eV}$). The reaction had already been studied by QITMS¹²⁸ and other techniques,¹³³ and was known to be slow, with a rate constant between 1.0×10^{-11} and $7.0 \times 10^{-12} \text{ cm}^3/\text{s} \cdot \text{molecule}$. In contrast, argon ions readily react with water (Figure 4-12). Products from charge-exchange and hydrogen atom transfer were observed at 18 and 41 Da, respectively. The absence of signal at 28 and 32 Da indicated that reactions with nitrogen and oxygen were much slower with comparable concentration.

Using the previously determined water pressure of 1.3×10^{-7} torr (the background pressure remained constant) a rate constant of 3.3×10^{-9} cm³/s-molecule was calculated (Table 4-12 and Figure 4-13). The value was higher than both the ADO approximation for polar neutrals of $k_{ADO} = 2.0 \times 10^{-9}$ cm³/s-molecule and literature values that were between 1.0×10^{-9} and 2.1×10^{-9} cm³/s-molecule. Other reactions were not obvious to explain the higher rate constant, but it was possible that argon charge-exchanged with background hydrogen, and produced ions that were not detected. It was also possible that the determined water concentration was not accurate, since at the low water pressure, small differences had a larger impact on the calculated value.

Water concentrations were kept low inside the ion trap under controlled experimental conditions. With only 1.3×10^{-7} torr of water, argon ions had a half-life of 33 ms, which was longer than the scan period; however, water concentration in samples from the Space Shuttle may not be as well controlled, and sensitivity and signal stability may be affected.

Table 4-12. Ion-molecule reaction between argon ions and water; three replicate runs.

Criteria	Run 1	Run 2	Run 3
Chamber temperature (K)	297	297	297
BG pressure (torr)	4.0×10^{-7}	4.0×10^{-7}	4.0×10^{-7}
Ar pressure – main inlet (torr)	7.2×10^{-6}	7.2×10^{-6}	7.2×10^{-6}
N_d of added Ar (molecule/cm ³)	2.3×10^{11}	2.3×10^{11}	2.3×10^{11}
N_d of H ₂ O (molecule/cm ³)	4.3×10^9	4.3×10^9	4.3×10^9
Reaction rate ($-\ln \Delta H_2^+ / s$)	13.6	14	14.2
k using H ₂ O (cm ³ /s-molecule)	3.2×10^{-9}	3.3×10^{-9}	3.3×10^{-9}

Thermodynamics of O₂⁺ and H₃O⁺

Three of the four AHGD analytes were found to react rapidly with gases in the background, but oxygen ions, on the other hand, were unreactive. Figure 4-14 shows that at thermodynamic equilibrium (> 2 s reaction time), oxygen ions were still present inside the ion trap. Oxygen had a relatively low ionization energy; thus, other ions charge-

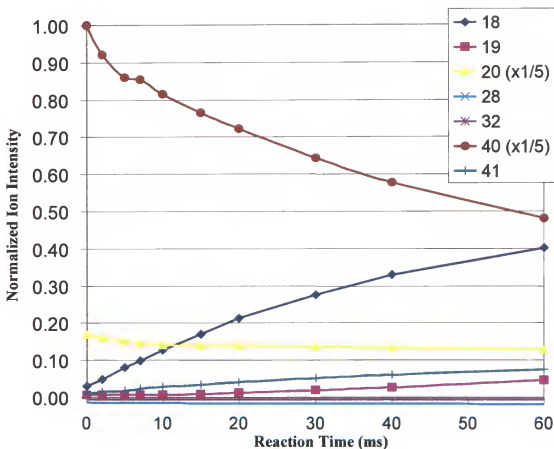


Figure 4-12. Ion intensities versus reaction time for the reaction of Ar^{++} with background gas. At an argon partial pressure of 7.2×10^{-6} torr and an approximate water partial pressure of 1.3×10^{-7} torr, argon ions are slowly lost, with a half-life of 60 ms. Reaction products at 18 and 41 Da are detected, indicating both charge-exchange and hydrogen atom transfer are occurring. The signal intensities for argon ions at 20 and 40 Da were reduced to 1/5 of their initial level to permit display with less intense product ion signals.

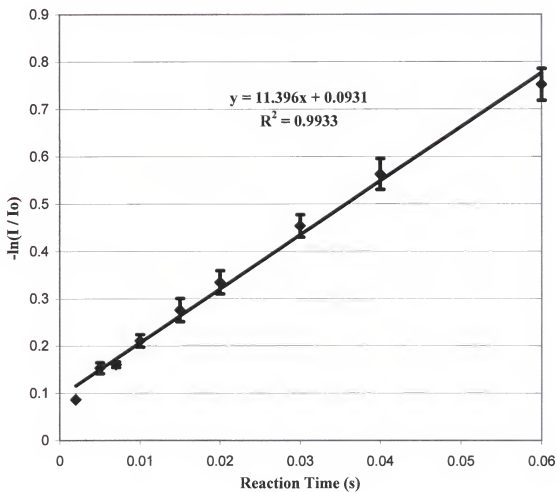


Figure 4-13. Plot of the change in argon ion signal versus reaction time. Data points are the average of three repetitive runs, with error bars of 1σ .

exchanged with neutral oxygen, causing the oxygen ion signal to increase until the reactant ions were depleted.

The only other ion signal observed at equilibrium was that of the hydronium ion at 19 Da, which had a lower recombination energy than the oxygen ionization energy. Water also had a low ionization energy, just as oxygen; thus, water ions were readily produced through charge-exchange with other ions. The hydronium ion was primarily produced by self-protonation, but was also formed by reactions with other Brønsted acid ions such as H_2^+ and N_2H^+ that had lower proton affinities than water.

As evident from Figure 4-14, a long reaction period was required to reach thermodynamic equilibrium. This was not the case when the vacuum pumps were first started. While the vacuum chamber was open to air, a large amount of water condensed inside, which did not immediately pump away when the chamber was placed under vacuum. Mass spectra consisted exclusively of hydronium and oxygen ion peaks. This lasted for only a few hours on the UF-IT, which had an open trap configuration more conducive to pumping away water, but lasted for three days on the PolarisQ, which had a closed ion source and ion trap. The AHGD project stipulated a maximal two-hour evacuation period. To meet this requirement, chamber heaters were installed on the UF-IT, which sped up the removal of water (actual pump-down times varied in proportion to the time the system was left open to air).

Conclusions

Ion-molecule reactions between ions of the AHGD project analytes and background gases have an effect on the analytical performance of the QITMS. Reactions such as hydrogen and helium ions with nitrogen, the predominant background component, occur

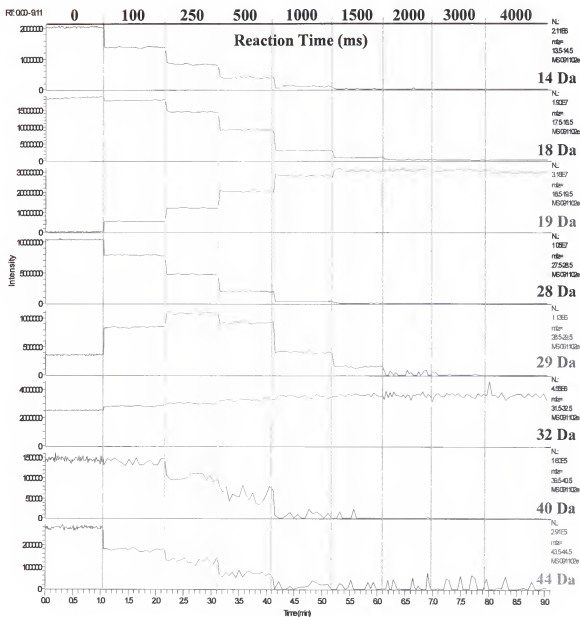


Figure 4-14. Monitored ion signals of background gases (4.0×10^{-7} torr) as the reaction time was incremented from 0 to 4000 ms. Thermodynamic equilibrium was reached after 2000 ms, with only ion signals for hydronium and oxygen ions remaining.

rapidly, consuming half of the stored ions within 1 to 2 ms. Thus, ion signals are significantly reduced during the 10 to 20 ms long QITMS scan function. At the same time, chemical noise was increased by the addition of product ions. The AHGD analytes also react readily with water, which makes the QITMS potentially sensitive to environmental changes.

The negative effects of ion-molecule reactions can be mitigated by controlling both time and pressure inside the ion trap. With the proper adjustment of these parameters, the QITMS can operate at high nitrogen and water pressures, but with a sacrifice in analytical performance. In Chapter 5, the optimization of QITMS for the AHGD application is presented, which is followed in Chapter 6 with the performance results.

CHAPTER 5 OPTIMIZING QITMS FOR LIGHTWEIGHT GAS ANALYSIS

Introduction

The QITMS is a dynamic mass spectrometer that performs ionization, ion manipulation, and mass analysis in a series of steps spread out in time. The operational parameters for each step can be adjusted to optimize the QITMS for a particular application. This is particularly important for the Advanced Hazardous Gas Detection (AHGD) application in light of the rapid ion-molecule reactions discussed in Chapter 4. In this chapter optimization of the UF-IT to minimize effects of ion-molecule reactions while maximizing analytical performance is discussed.

Conditions for Ionization

The first step in mass analysis is ionization of the analytes, which on the UF-IT is performed inside the ion trap by electron impact (EI) ionization. Ionization occurs as electrons enter the ion trap over a variable period. If their mass-to-charge ratio is above the low-mass cutoff, they are then trapped in the quadrupole.

Electron energy

Thermalized electrons entering the ion trap will collide with neutral gas, but will only produce ions when the electron energy is greater than the ionization energy of that gas. On the UF-IT, electrons are accelerated from a heated filament by a user adjustable bias potential. The kinetic energy then changes as they pass through sequential electric fields generated by the electron optics until they enter the ion trap. Once inside, their energy is dependent on the oscillating quadrupole field. Since the field is not static,

electrons that enter at different times will have different energies,^{135,136} as illustrated in Figure 5-1 where electron energy is plotted versus RF phase angles. The quadrupole field strength, the trajectory angle of incoming electrons, and their initial energy, are other factors that influence the final electron energy, but the energy distribution is always periodic as shown. For half of the RF cycle, the quadrupole field potential is negative relative to the incoming electrons, thereby repelling them from the ion trap. During the positive part of the RF cycle, the electron energy varies. At some points it is too low to ionize the gas, and at others points it is high enough to fragment molecules. Thus, intact ions are formed during less than half of the ionization period, providing an ionization efficiency of only 20 to 30%.

Time and pressure

One advantage of QITMS is that the ionization period can be lengthened to store more ions and increase the signal-to-noise (S/N) ratio. The duty cycle is therefore high, making QITMS well suited for gas monitoring. Raising the analyte pressure can also increase the number of ions. In either case, however, chemical noise is also increased, unless the analyte can be separated from the gas matrix. Ions also undergo more collisions at longer ionization times and higher pressures, which will potentially neutralize analyte ions.

Low-mass cutoff

The low-mass cutoff during ionization is the m/z value that corresponds to a $q_z = 0.908$ for the given RF amplitude, where all ions below this cutoff have unstable trajectories. By properly setting the low-mass cutoff unwanted ions could be excluded during ionization; however, at the same time the ions of interest should have a q_z value

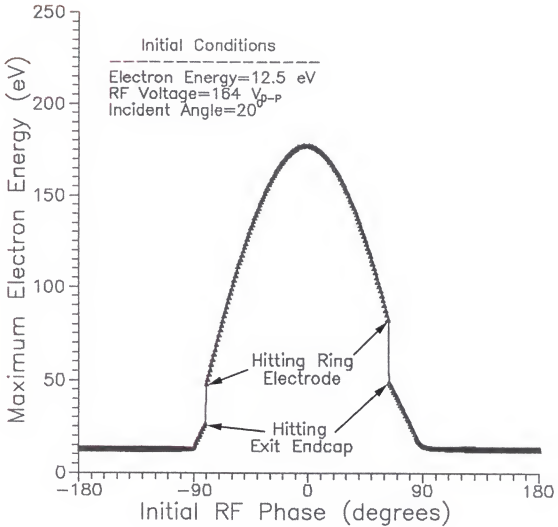


Figure 5-1. Distribution of electron energies of an internal ionization QITMS. The electron energy is dependent on the RF phase angle of the quadrupole field. (Adapted from Pedder, R. E.; Johnson, J. V.; Yost, R. A. Electron Energy in Quadrupole Ion Trap Mass Spectrometry. *Proceedings of the 40th ASMS conference on Mass Spectrometry and Allied Topics*. Washington, DC, 1992; Figure 2c, p. 1761.)

between 0.1 and 0.4. This is the optimal range where black holes at higher q_z values are avoided and the potential well depth is great enough to efficiently trap ions.

Space charge effects

Two or more ions of like charge stored in the ion trap will influence one another by coulombic repulsion. As more ions are trapped, the repulsive force grows to produce a significant potential that distorts ion trajectories causing what are known as space charge effects.^{7,12,25,137-139} Space charge manifests as an apparent shift in the stability diagram, which causes ions to eject late, and appear at higher m/z values.^{7,25} Severity of the space charge effect depends on the ion cloud shape, the m/z values of the ions, and their kinetic energy, but most influential is the number of stored ions. Peak shifts are noticed with as few as 10^4 ions, while decreased mass resolution is perceived at higher ion densities around 10^6 ions, above which additional ions become unstable and are ejected. Space charge occurs because ions of the same m/z value oscillate at the same frequency and therefore within the same local space of the ion trap. As more of these ions are collected, the ion cloud tends to expand outward, shifting some ions to higher frequencies, and interfering with ions at lower m/z . This results in tailing of the space-charged peak to lower mass, which is most significant for peaks that are close together.¹³⁹ Space charge effects will occur at lower ion density if the ion's q_z value or the drive frequency is increased, or by reducing the dimensions of the ion trap. Ions that are collisionally cooled will also experience greater space charge effects, but their energy is minimized through collisions. Overall, space charge is a significant limiting factor for the ion trap. New technologies, such as the toroidal¹⁴⁰ or the two-dimensional¹⁴¹ quadrupole ion traps, use geometries of increased trapping volume to improve detection by allowing more ions to be accumulated before reaching the space charge limit.

Ion Storage in the QIT

The QITMS is well suited to a variety of applications, because of its ability to store and manipulate ions. Electric fields can be used to probe the ion cloud to change its density, energy, or composition, as needed. Ion energy is also reduced during this period through collisional cooling, which improves mass resolution and sensitivity, particularly for larger molecules.^{21,23,40,102} This requires a collision gas, such as helium, that is unreactive and small enough to prevent scattering of lighter ions. The collision gas is also used for molecular dissociation.¹⁴² A selected ion can be resonantly excited by applying a waveform at its secular frequency. This allows for more energetic collisions that result in fragmentation. Waveforms can also be used to isolate single mass-to-charge values. Using ion isolation and collisional dissociation together, the QITMS can perform more complex scans such as selective reaction monitoring (SRM),¹⁴³⁻¹⁴⁶ or multiple stage mass spectrometry (MSⁿ).^{10,15,42,147-149} These experiments can also be performed with tandem-in-space mass spectrometers, such as the triple quadrupole or the compound sector,¹⁴⁸ but the QITMS is more flexible because the timing of the experiment can be controlled.¹⁵⁰ This versatility distinguishes the QITMS from other mass analyzers; however, this comes at a cost – extra time is required for these complex scans. This lowers the duty cycle and allows events to go unnoticed if they fall between scans.

Ion Ejection from the QIT

In mass-selective ejection, the RF amplitude is ramped to increase the secular frequency of ions until they mass selectively come into resonance at the $\beta_z = 1$ stability boundary, where they absorb energy and are displaced axially through holes in either endcap for detection.⁷⁻⁹ The quadrupole field strength increases linearly with displacement from the center of the ion trap, providing a linear relationship between RF

amplitude and mass-to-charge. An auxiliary field can also be applied to the endcaps to resonantly eject ions at any point in the stability diagram. Resonant ejection is used on commercial instruments, because it minimizes complications from the nonlinear behavior of a real ion trap discussed in the next section.

Ejection by nonlinear resonance

It is not possible to produce a pure quadrupole field in a real ion trap.¹⁵¹⁻¹⁵⁴ Truncation of the electrodes to a finite size and the addition of holes in the endcaps cause superposition of higher-order fields (e.g., hexapole, octopole, decapole, etc.) onto the quadrupole field. The strengths of the higher-order fields do not increase linearly with distance from the ion trap center, which causes the ion trap to behave nonlinearly as the RF amplitude is ramped. Odd order fields in particular, such as hexapole or decapole, are not symmetrical; therefore, they tend to also defocus the ion cloud by shifting the center of oscillation away from the middle of the ion trap (the even order fields, such as octopole or dodecapole, are symmetrical). The strength of higher-order fields increases as an ion moves to higher q_z values. Because of this, hexapole and octopole fields are most influential, since they cross the $a_z = 0$ line at the higher q_z values (Figure 5-2 where hexapole field lines start at $n_z = 3$ and octopole at $n_z = 4$).^{154,155} When an ion absorbs energy from these fields, its displacement is increased, and given enough time this displacement can result in ejection if the field is strong enough. Since ions are lost at the points where higher-order resonance lines cross the $a_z = 0$ line, they are known as black holes, and above and below the $a_z = 0$ line, resonance lines carve out large areas of poor trapping efficiency known as black canyons. This is illustrated in Figure 5-3 for a part of the stability diagram.^{97,154}

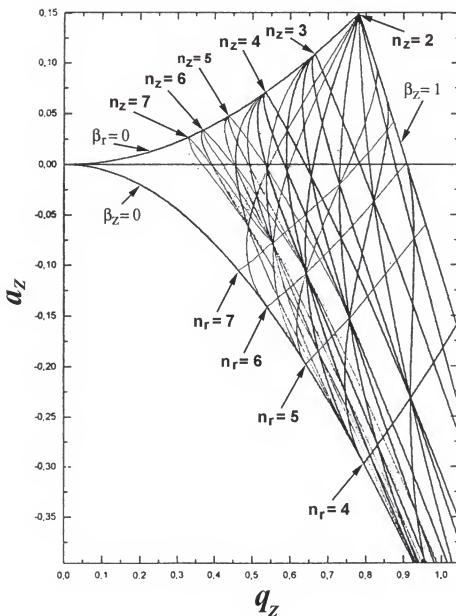


Figure 5-2. Lines of nonlinear resonance within the stability diagram. Higher-order field lines described by the equation $n_r \omega_r + n_z \omega_z = \Omega$ stretch between the axial, n_z , and radial n_r , nodes each for a different field order (2 for quadrupole, 3 for hexapole, 4 for octopole, etc.). These lines can also be expressed in terms of β values by the equation $(n_z/2)\beta_z + ((N - n_z)/2)\beta_r = 1$, where N is the series $n_z, (n_z + 1), (n_z + 2)$, etc. For example: the first line of node $n_z = 2$ has $N = 2$, thus $(2/2)\beta_z + ((2 - 2)/2)\beta_r = 1$ or $\beta_z = 1$; the first line of node $n_z = 3$ has $N = 3$, thus $(3/2)\beta_z + ((3 - 3)/2)\beta_r = 1$ or $\beta_z = 2/3$. (Adapted from Alheit, R.; Gudjons, Th.; Kleineidam, S.; Werth, G. *Rapid Commun. Mass Spectrom.* Vol. 10, 1996; Figure 3, p. 586.)

In order to absorb energy from high-order fields, ions must first be displaced from the ion trap center. The presence of a collision gas that cools the ions to the center of the ion trap helps to minimize these effects; however, ion displacement will still be large during ionization,¹⁵⁴ or ion injection,^{42,154} depending on the type of ion source used. Displacement is also large during the collisional dissociation step of an MS/MS experiment, when ions are excited to allow fragmentation. The fragment ions will also have large displacements, and because they are lower in mass they will have higher q_z values; therefore, they may coincide with a higher-order resonance point and be ejected.^{154,156}

The shifting of peaks to higher mass caused by higher-order fields was a significant problem with the prototype Finnigan ITD that held up its release.¹⁸ The negative octopole field induced by holes in the endcaps allowed some ions to remain stable beyond $q_z = 0.908$. To resolve this, Finnigan stretched the ion trap axially by 10.6%, such that r_0^2 no longer equaled $2z_0^2$, which added a positive octopole field to cancel out the negative field.^{18,157-159}

Even with a stretched geometry, multiple higher-order resonance points exist close to $q_z = 0.908$. These fields reduce the pseudo-potential well depth close to the $\beta_z = 1$ stability boundary as illustrated in Figure 5-4.¹⁶⁰ The reduced potential well can no longer hold all of the ions, so they begin to eject through sequential black holes, resulting in wide mis-shaped, poorly resolved peaks. This is avoided on commercial instruments by using resonant ejection at a slightly lower q_z value than 0.908.¹⁶¹

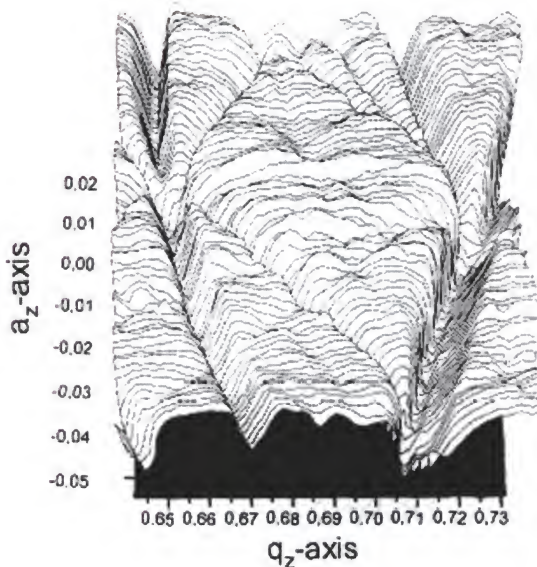


Figure 5-3. Three-dimensional representation of black canyons within the stability diagram. The ion intensity at different a_z , q_z values was plotted. Trapping efficiency is poor where high-order field lines cross the stability diagram, forming black canyons. (Adapted from Alheit, R.; Kleineidam, S.; Vedel, F.; Vedel, M.; Werth, G. *Int. J. Mass Spectrom. Ion Process.* Vol. 154, 1996; Figure 9, p. 162.)

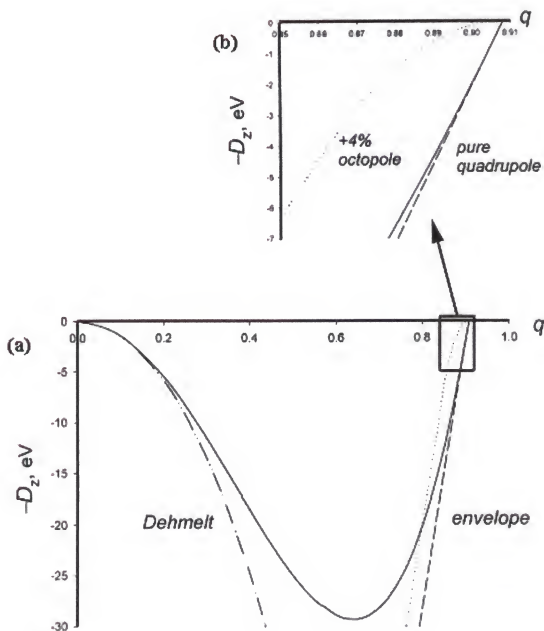


Figure 5-4. Distortion of the pseudo-potential well caused by a +4% octopole field. Stretching of the ion trap in the axial dimension produces a positive octopole component. The pseudopotential well, shown in (a) over the entire stability diagram and in (b) for higher q_z values, is estimated using the Dehmelt approximation (solid line), and the beat-envelope method (dashed line). The addition of a positive octopole field distorted the potential well, (indicated by the dotted line), decreasing the depth at $q_z=1$ stability boundary. (Adapted from Sudakov, M. *Int. J. Mass Spectrom.* Vol. 206, 2001; Figure 8, p. 38.)

Mass resolution controlled by ejection rate

Bulkier compounds produced greater peak shift on the prototype ITD, because they were less effectively cooled to the center of the ion trap, and were therefore more influenced by the higher-order fields. The axial dimension was modified to correct the problem, but later it was realized that this selective higher order field effect could be positively used to resolve isobars.^{159,162,163} This was not, however, a general purpose means to increase mass resolution on the QITMS.

High-resolution was first achieved on the QITMS by using mass-selective storage in a manner akin to performing high-resolution scans on a quadrupole. The operating line was positioned closer to the apex of the stability diagram, which narrowed the mass range of stable ions within the ion trap.^{164,165} Though effective, this method reduced sensitivity, and could not be used with mass-selective ejection on commercial instruments.

In the early 1990s, mass resolution was found to be improved with mass-selective ejection by slowing the ion ejection ramp rate.^{161,166-168} This would eject ions farther apart in time, allowing for more RF steps between peaks, which narrowed peaks measured in mass units. Unfortunately, peak height was also decreased because the same number of ions was ejected, so the peak area remained the same. However, the ions came out over a longer period so the peaks were broader and shorter (as viewed in time), with a decrease in S/N.¹⁶⁶

Specialized scan routines

The use of longer scans decreases the duty cycle of the instrument, reducing the detection capability. For those applications where sensitivity is critical the duty cycle can be maximized by monitoring a single m/z value with a type of scan known as selective-ion monitoring (SIM).¹⁶⁹ Ionization and isolation waveforms (or apex isolation) can be

used in a SIM scan to remove ions of different m/z values, allowing more analyte ions to be stored. The SIM scan also uses ionization and trapping conditions optimized specifically for the analyte ion, which further improves detection.

Similar to SIM scan, a segmented scan is used for applications that require monitoring of ions of different m/z values spread over a wide mass range.¹⁷⁰ The duty cycle is maximized by using short independent scans, known as segments, for ions that are far apart, and each segment uses optimal ionization and trapping conditions for its m/z range.

Experimental Details

This chapter details optimization of QITMS for analysis of AHGD analytes. Parameters for ionization, ion storage, ion ejection, and data acquisition were examined. A segmented scan routine was created to provide optimal conditions with the greatest duty cycle for maximum sensitivity.

Sample Gas

Pure nitrogen and a mixture containing 5000ppm of each analyte in a balance of nitrogen were used for all experiments unless otherwise stated. The gas samples were mixed and delivered using the GDS (described in Chapter 3), and passed into the ion trap through the main inlet. Briefly, the GDS used MFCs to admit gas from either a gas cylinder of pure nitrogen or a 2.5% mixture of each analyte in nitrogen. Gas was continuously admitted into a mixing plenum at 500 SCCM, and was regulated to 900 torr. A side stream was drawn by a mechanical pump through a Granville-Phillips variable 203 leak valve that allowed regulation of the inlet pressure between 20 mtorr and 10 torr.

Instrumentation

Optimization was performed using the UF-IT described in Chapter 3. A 0.001 in. orifice admitted gas through the transfer line and into the ion trap. Pressure measurements were taken with a Granville-Phillips Microion Gauge, and temperature was regulated to 30 °C by a heating element controlled by an Omega CN9000A thermostat with a k-type thermocouple. The UF-IT had a mass range from 1 to 62 Da using a drive frequency of 2.5 MHz.

The modified Polaris Q, also described in Chapter 3, required similar optimization, which was performed with the optimized UF-IT as a model. Gas passed through a 0.002 in. orifice, twice the size as used on the UF-IT, and into an external EI ion source. The chamber pressure was measured with a Granville-Phillips Microion Gauge, but the ion trap was filled to 1 mtorr with a helium collision gas. Only the ion source was heated (kept at 250 °C), leaving the vacuum chamber and ion trap to fluctuate with the room temperature. The modified PolarisQ operated at a drive frequency of 2.82 MHz with a proven mass range between 3 and 44 Da.

Software

Customized software for the UF-IT and PolarisQ instruments (Chapter 3) allowed easy adjustment of ion trap parameters. Mass analysis was performed by a series of steps, each with specific settings for the dynamic ion trap parameters: electron bias, electron lens potential, gate lens potential, electron multiplier voltage, and data acquisition, all of which were synchronized to the timing of the RF amplitude. A two-dimensional array called the scan matrix was used to program the necessary settings for the scan function (the AHGD optimized scan matrices are in Appendix D for the UF-IT and Appendix C for the PolarisQ).

Results and Discussion of QITMS Optimization

QITMS instrumentation poses a unique advantage over other mass analyzers because of its ability to accumulate large numbers of characteristic ions. The QITMS has a high duty cycle, which is useful for on-line monitoring purposes to detect fast changing signals. The combination of high sensitivity and rapid analysis makes the QITMS well suited for the AHGD project.

Ionization of the QITMS

The goal with QITMS is to quickly accumulate a large number of ions to maximize S/N and to average many scans per a given period for greater precision. Integral to this is the creation of a dense stream of ionizing electrons, an adequate analyte pressure, and sufficient time to fill the ion trap. Ionization conditions would need to minimize effects from ion-molecule reactions, while at the same time capitalize on the ion storage capability of the ion trap.

Electron optics

The UF-IT uses internal EI ionization; therefore, the energy of ionizing electrons varies with respect to the oscillating RF field. Though the user cannot control this, the electron optics can be optimized to properly focus the 200 μ A electron beam through the 1 mm hole in the entrance endcap. The ion trap and electron optics were taken from a Finnigan ITS-40, which used a gate lens potential of +200 V when admitting electrons. The gate lens power supply used on the UF-IT only reached a maximum of +130 V. To compensate for the difference, the electron lens was adjusted to a negative potential, optimally -80 V. At the same time, the filament bias was kept at the same optimal voltage relative to the electron lens of -17 V by setting the filament bias to -97 V.

Ion trap pressure versus ionization time

The response of the instrument to a varying pressure and ionization period was examined. The experiment involved monitoring ion peak intensity as the pressure was increased nine times between 1×10^{-6} and 6×10^{-6} torr, and with ten different ionization periods varied from 1 to 10 ms at each pressure. The experiment was performed, first while sampling pure nitrogen, and then repeated while sampling the 5000-ppm analyte mixture. Figures 5-5 through 5-8 are three-dimensional plots of the ion intensity change for hydrogen, helium, oxygen, and argon ions, respectively.

The two lighter species required lower trap pressures than the heavier two. The loss in ion intensity for hydrogen and helium illustrated their reactivity, fitting well with Chapter 4 results in which both ions reacted quickly with nitrogen. Hydrogen appeared more affected than helium, partially explained by the faster reaction rate of hydrogen ions with nitrogen, but in addition, hydrogen was more apt to be scattered by successive impacts with nitrogen molecules (the major background species), since hydrogen was half the size of helium.

The plots for oxygen and argon also differed from one another. Oxygen sensitivity improved with increased pressure and ionization time, because oxygen ions were unreactive, and more were continually produced through charge-exchange of other ions with neutral oxygen. In contrast, argon ions reacted with other neutrals, particularly water, which explained the plot leveling off at higher pressures and longer ionization periods.

Overall, the optimal ionization conditions were quite different for the lower and higher masses. Ideally, different pressures for both would provide the best performance,

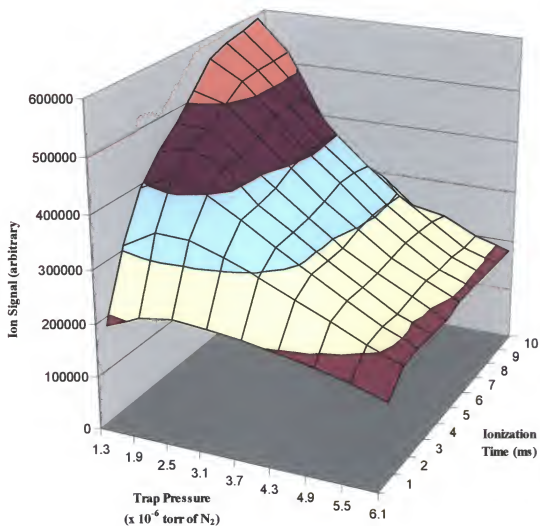


Figure 5-5. Hydrogen ion signal response with changing ionization conditions. The gas pressure and ionization period were varied while monitoring the ion signal at 2 Da. Plotted is the difference in intensity between the pure nitrogen and the 5000-ppm hydrogen in nitrogen mixture. Actual trap pressures can be calculated by multiplying the plotted value by the main inlet correction factor of 2.54 (detailed in Chapter 4).

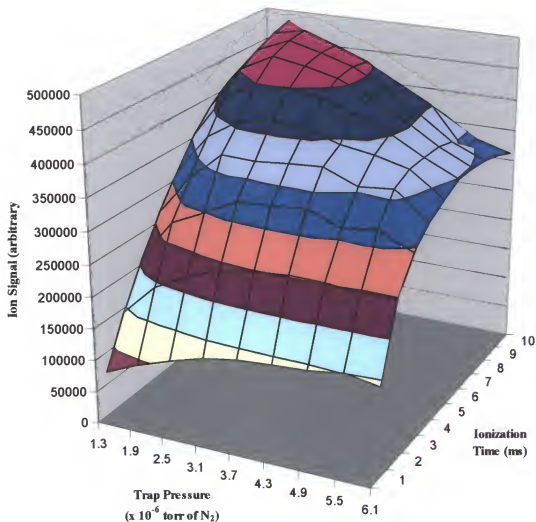


Figure 5-6. Helium ion signal response with changing ionization conditions. The gas pressure and ionization period were varied while monitoring the ion signal at 4 Da. Plotted is the difference in intensity between the pure nitrogen and the 5000-ppm helium in nitrogen. Actual trap pressures can be calculated by multiplying the plotted value by the main inlet correction factor of 2.54 (detailed in Chapter 4).

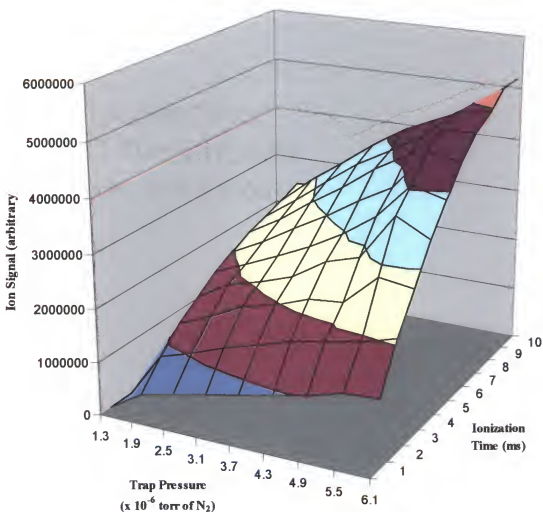


Figure 5-7. Oxygen ion signal response with changing ionization conditions. The gas pressure and ionization period were varied while monitoring the ion signal at 32 Da. Plotted is the difference in intensity between the pure nitrogen and the 5000-ppm oxygen in nitrogen mixture. Actual trap pressures can be calculated by multiplying the plotted value by the main inlet correction factor of 2.54 (detailed in Chapter 4).

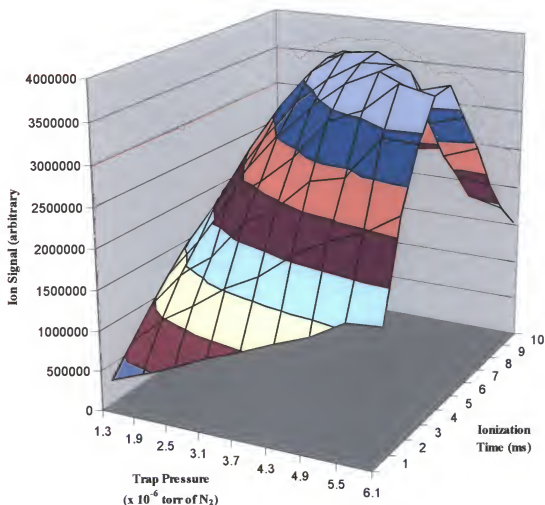


Figure 5-8. Argon ion signal response with changing ionization conditions. The gas pressure and ionization period were varied while monitoring the ion signal at 40 Da. Plotted is the difference in intensity between the pure nitrogen and the 5000-ppm argon in nitrogen mixture. Actual trap pressures can be calculated by multiplying the plotted value by the main inlet correction factor of 2.54 (detailed in Chapter 4).

but this is not realistically feasible (pulsed pressure valves are available but at a sizeable cost). A compromise in trap pressure was found at 3×10^{-6} torr (7.6×10^{-6} torr with the main inlet correction factor), where detection limits for all four appeared comparable (Chapter 6). At this pressure a 5 ms ionization period was the most efficient, above which only the signal for oxygen ions continued to increase linearly.

The optimal q_z for ionization

A proper RF amplitude during ionization is critical for efficient trapping of ions. The optimal amplitude is inversely proportional to the mass of an ion, and thus is different for the lighter and the heavier AHGD analytes. The lower mass ions were trapped most efficiently at a q_z value close to 0.35 as shown in Figure 5-9, but because helium is twice the mass of hydrogen, q_z values of the two species differed considerably for a given RF amplitude. A compromise of 90V was selected, where the ion signal for helium, which was most difficult to ionize, was near to its maximum while the hydrogen ion signal was still substantial (the RF amplitude could be lowered to improve hydrogen detection).

The optimal q_z value for oxygen and argon as observed in Figure 5-10 is approximately 0.13, which is, as expected, lower than that for the lighter masses. Argon is only 20% more massive than oxygen, thus their q_z values per given RF amplitude will be close together, which allows both ions to be near their maximum intensity at the same RF amplitude of 335V. With considerably different ionization conditions for the lighter and the heavier ions, two different ionization periods were required to provide adequate sensitivity for both. This was best performed with a segmented scan function, where hydrogen and helium would be ionized and analyzed independently of oxygen and argon.

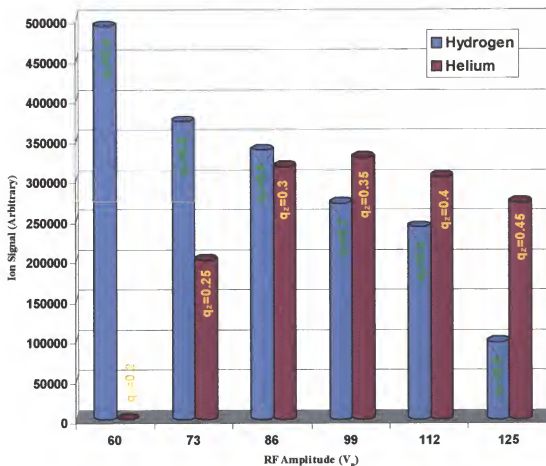


Figure 5-9. Plot of H_2^{++} and He^{++} ion signals versus RF amplitude during ionization. Both species were ionized most efficiently at a q_z of 0.35; however, because helium is twice the mass of hydrogen, their q_z values at a given RF amplitude were much different. Thus a compromise of 90 V was selected, because it maximized the helium ion signal (the most different to ionize) while maintaining a substantial hydrogen ion signal.

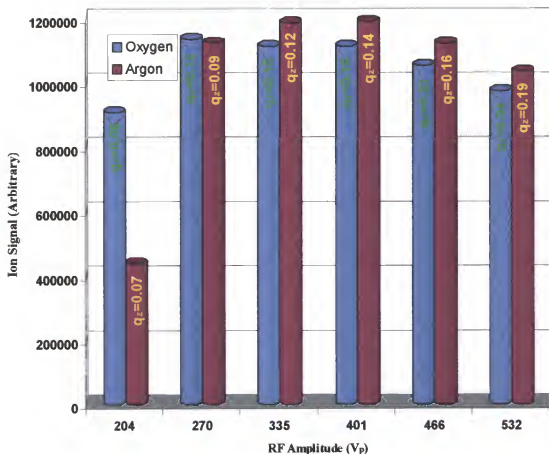


Figure 5-10. Plot for O_2^{++} and Ar^{++} ion signals versus RF amplitude during ionization. The optimal q_z value for ionization was approximately 0.13 for both species. Since argon is only 20% more massive than oxygen, their q_z values at a given RF amplitude were close together, which allowed optimal trapping of both at 335 V.

Intermediary Scan Function Activity

Every extra millisecond after ionization decreases the performance of the UF-IT, because of the rapid ion-molecule reactions occurring with the AHGD analytes. This conflicts with the normal operation of a commercial QITMS, where a long post-ionization period is used to collisionally cool ions. For the AHGD application, collisional cooling is not used, since it does not provide any benefit. All remaining post-ionization activity must occur rapidly to maximize S/N.

The first post-ionization event is the removal of unwanted nitrogen ions during the oxygen/argon scan segment. Most ions formed will be from nitrogen, the predominant gas, and since it is near in mass to oxygen and argon, all of these ions will be efficiently trapped together (not the case during the lighter mass scan segment). The large nitrogen ion population will induce space charge effects that interfere with the analyte ions. To minimize unwanted ion-ion interactions, the nitrogen ions are ejected from the ion trap right after ionization by quickly ramping the RF amplitude. Figure 5-11 shows that the nitrogen peak appears to decrease as the ramp period is extended. This is because nitrogen ions are now ejecting before the electron multiplier is initialized over an optimal period of 0.3 ms where the nitrogen ion signal is no longer detected, thereby protecting the electron multiplier from damage caused by excessively high ion currents.

The electron multiplier is also protected is using a standby state of 400 V during ionization. The lower cathode voltage decreases the gain of the device, thereby reducing wear-and-tear. When increasing the bias voltage to its operational value of 1600 V, charge flows to the anode, observed as a wide hump in Figure 5-11. A minimal period of 0.4 ms is required for the changing current to decay, before the electron multiplier is ready for detection.

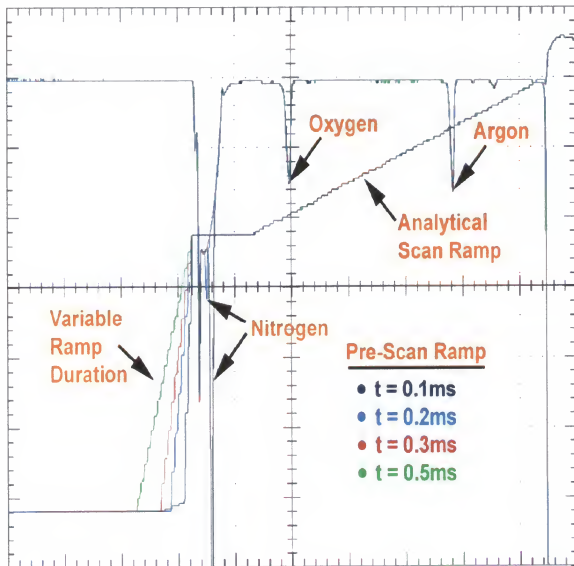


Figure 5-11. Oscilloscope display of post-ionization activity. The inverted output of the electrometer circuit is displayed at the top, with the ion signals for nitrogen, oxygen, and argon appearing as indicated. A plot of the RF amplitude is also displayed showing the nitrogen ejection ramp on the left. By increasing the duration of the ramp the detected nitrogen ion signal decreased. At a period of 0.3 ms, all of the nitrogen ions ejected prior to initializing the electron multiplier preventing damage. The initialization period, where the cathode voltage is raised to 1600V for detection, is indicated by the wide hump from the charging current. A 0.4 ms period elapses before the electron multiplier output stabilizes, after which the analytical scan begins.

Ion Ejection and Acquisition

The final step of mass analysis is the analytical scan, where the RF amplitude is ramped to mass selectively eject ions to produce the mass spectrum. The mass range of a particular scan depends on the starting and ending amplitude of the RF ramp. The rate of the ramp, known as the scan rate, influences mass resolution and sensitivity. This is demonstrated in Figure 5-12, where four different scan rates were tried, from the normal Finnigan GCQ value of 0.18 ms/Da up to nine times this rate. Peaks become taller, narrower, and occur closer together with faster scan rates. This is because the same number of ions leave the ion trap in a shorter time; therefore, the area of a peak remains the same, but it becomes taller and narrower. At the same time, mass resolution decreases, since fewer RF steps are made between masses. The limiting factor in this case is not the number of available DAC bits, but the speed at which the RF DAC output is changed. All electrical components, including the RF DAC, are updated every 30 μ s by the control DSP. Thus, at a scan rate of 0.02 ms/Da, at most, only one RF step separates each m/z. The next fastest rate, 0.06 ms/Da, has a sufficient number of steps to maintain unit resolution.

The acquisition hardware provided another limitation. Samples were taken at a rate of 100 kHz; therefore, a maximum of two points was acquired per m/z when using a scan rate of 0.02 ms/Da, which was insufficient to characterize a peak. At a scan rate of 0.06 ms/Da, six data points were acquired per m/z, which was sufficient to characterize a peak, but with some distortion resulting in signal fluctuations. This negative point was outweighed by the greater speed and peak heights of the faster rate, which minimize signal loss because of ion-molecule reactions, and maximizing the S/N.

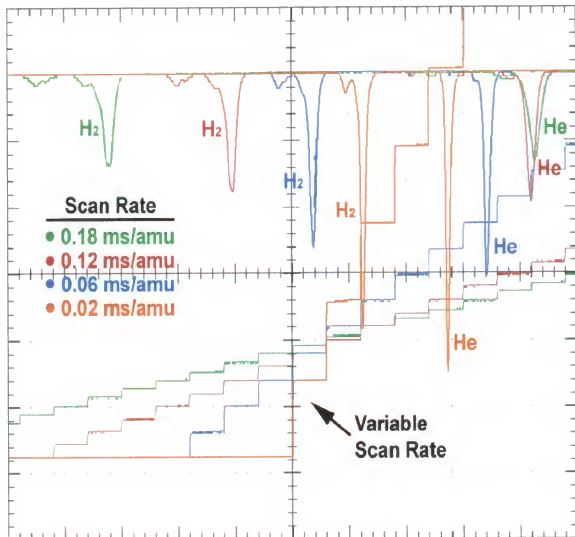


Figure 5-12. Oscilloscope display of H_2^{++} and He^{++} ion peaks using different scan rates. The inverted output of the electrometer is displayed at the top, with ion signals for hydrogen and helium ions as indicated. The RF ramp used to eject the ions is indicated at four different rates from the normal Finnigan GCQ rate of 0.18 ms/Da up to nine times this rate. The produced ion signals are color-coded to the scan rate used. Ions are ejected in tighter packets with increasing rate, thereby reducing peak widths measured in time, and increasing peak height for better S/N. The hydrogen and helium peaks are, however, closer together with only two RF DAC steps between them. Therefore, mass resolution is decreased.

A delay between ion ejection and signal processing was an additional complication. Figure 5-13a shows the ejection of hydrogen ions observed on the oscilloscope, and Figure 5-13b as displayed on the computer screen. It took nearly 400 μs before the ion peak was processed for display or saving to a file. Because of this, the start and stop points of the acquisition were delayed from the start and stop of the RF ramp, which added an additional 0.4 ms to the scan time.

Post scan activity

Once the analytical scan has been completed, the instrument must be reset for the start of a new scan. During a 0.25 ms period following the analytical scan, the RF amplitude is lowered to 0 V, clearing the ion trap of any remaining ions. Afterward, the RF amplitude is reset to the ionization level. The RF signal is allowed to stabilize for another 0.25 ms before ionization begins.

Nonlinear resonance

Slowing the scan rate improves mass resolution; however, other unwanted effects were observed. Figure 5-14 is a spectrum of pure nitrogen taken at a fast scan rate of 0.06 ms/Da. A few minor peaks appeared at fractional masses, but were dismissed as peaks of common background components (e.g., carbon, oxygen, etc.) that were inaccurately displayed because of the limited number of RF steps. Figure 5-15 shows a mass spectrum of the same gas, but this time with a slow scan rate of 1.00 ms/Da. As expected, peak widths decreased, but unexpected new peaks appeared, forming an identical pattern to the left of the three major ion peaks (14, 18, and 28 Da).

Table 5-1 lists the distinguishable peaks from Figure 5-15 between 5 and 28 Da. The major ion signals at 28, 18, and 14 Da correspond to the ions N_2^+ , H_2O^+ , and either N^+

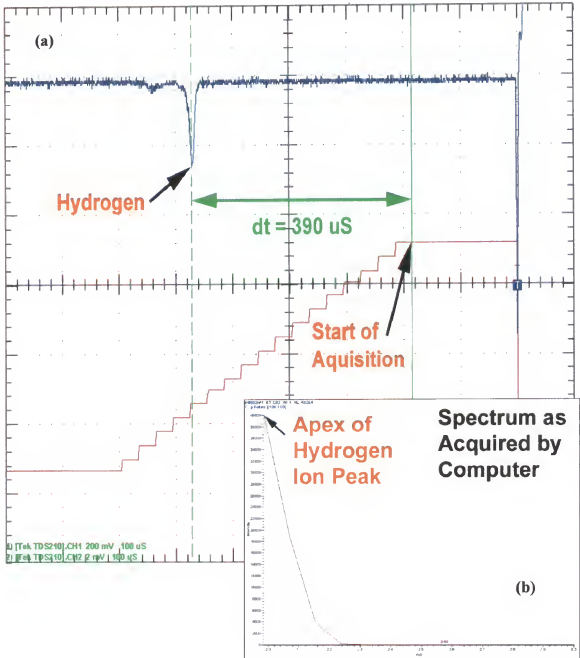


Figure 5-13. Oscilloscope display of delayed acquisition: a), and computer acquired display, b), of the hydrogen ion peak. The inverted output of the electrometer is shown in blue at the top of (a), with the hydrogen ion peak marked, and the analytical scan is illustrated in red. Hydrogen ions are ejected after five RF steps, but the computer does not display the peak until $390 \mu\text{s}$ later when the acquisition began.

061102c: #223-288 RT: 3.35-4.32 A/V: 66 NL: 5.00EB
T: -p Full ms [5.00-45.00]

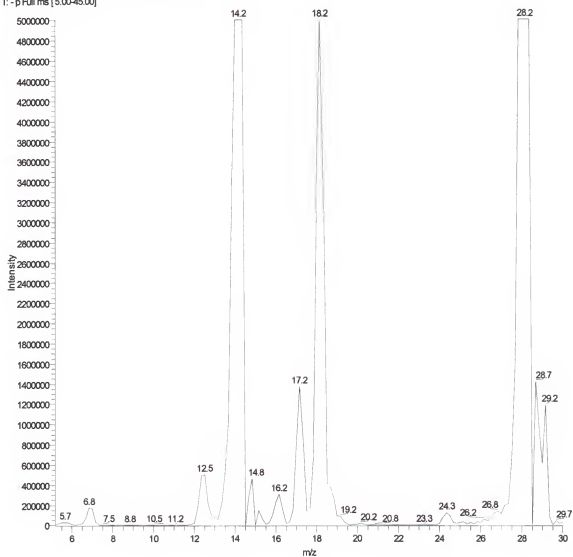


Figure 5-14. Mass spectrum taken of pure nitrogen at a scan rate of 0.06 ms/Da. The spectrum has been normalized to the water ion peak at 18 Da to show less intense background peaks. Some tailing of the nitrogen ion peak at 28 Da is observed, because of space charge effects.

061102a #57 RT: 3.18 AM: 1 NL: 1.00E5
T: -p Full ms [5.00-45.00]

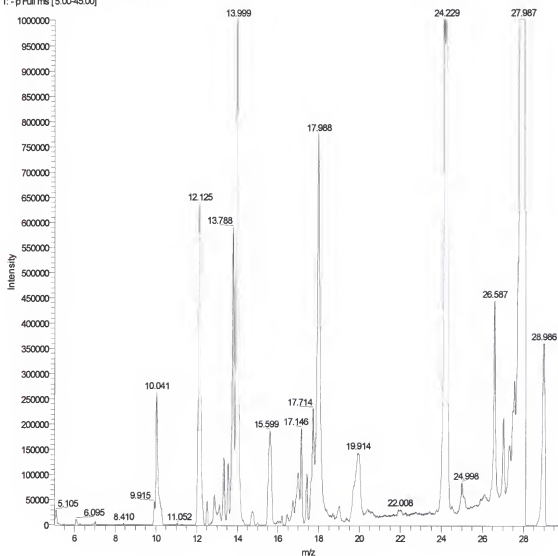


Figure 5-15. Mass spectrum taken while sampling pure nitrogen at a scan rate of 1 ms/Da. The spectrum was normalized to the atomic ion peak of nitrogen at 14 Da to show less intense background peaks. Peaks widths were considerably reduced with the slower scan rate. At the same time new peaks appeared that were not observed at the faster scan rate. The same peak pattern appeared to the left of each major ion peak, N_2^+ peak at 28 Da, the H_2O^+ peak at 18 Da, and the N^+ peak at 14 Da. The peaks of the pattern corresponded to ejection through black holes along the $a_z = 0$ line of the stability diagram.

or N_2^{+2} . It was assumed that these peaks occurred at $q_z = 0.90805$; all the others were assigned q_z values relative to these three, and $q_r = -1/2q_z$ values (e.g., the peak at 24.219 Da relative to N_2^{+2} at $q_z = 0.90805$ would have a $q_z = [(24.219 \times 0.90805)/28.0061] = 0.786$ with $q_r = -q_z/2 = -0.393$). From the resulting $q_z q_r$ pairs, β_z , β_r values were calculated. Nearly every new peak corresponded to the early ejection of one of the three major ions through black holes in the stability diagram. Ejection at the dominant $\beta_z = 2/3$ and $1/2$ resonance points was observed for all three major ions. Ejections at the more minor resonances were observed for at least two of three. The slower scan rate provided ions with more time to resonate and gain energy for ejection through black holes, complicating the mass spectrum when attempting high-resolution analysis.

High-resolution

The separation of isobars would effectively demonstrate the high-resolution capability of the UF-IT, but few isobar pairs exist that are light enough to be analyzed by the instrument. One pair is that of N_2^{+2} at 28.006 Da and $CH_2=CH_2^{+2}$ at 28.031 that is of interest to plant scientists wanting to monitor ethylene gas, which promotes the ripening of food. NASA in particular wants to monitor ethylene within the International Space Station for plant experimentation, and during future long duration space flights (e.g., a Mars mission) when crops would be grown for food.

A GC/MS system would be a likely choice for detecting ethylene in air, but a mass spectrometer that could resolve these isobars without chromatography would be even better. Eliminating the GC removes: a) the need for a carrier gas (typically helium); b) the need to replace columns when they spoil; and c) the need of a power hungry GC oven. The stand-alone MS would also be more compact, cost efficient, and faster than

Table 5-1. Observed nonlinear resonance ejection using a slow scanrate.

Observed Mass	q_z N_2^+	q_z H_2O^+	q_z N^+	B_z	B_r	Resonance equation	Ion
27.987	0.908	--	--	0.997	0.335	$B_r = 1$	N_7^+
27.566	0.894	--	--	0.890	0.330	$B_r = 1/3$	N_2^+
27.029	0.876	--	--	0.834	0.323	$B_z + 1/2B_r = 1$	N_2^+
26.587	0.862	--	--	0.799	0.317	*	N_2^+
26.103	0.846	--	--	0.767	0.311	$1/2B_z + 2B_r = 1$	N_2^+
24.998	0.811	--	--	0.705	0.297	$B_z + B_r = 1$	N_2^+
24.219	0.785	--	--	0.668	0.287	$B_z = 2/3$	N_2^+
24.156	0.783	--	--	0.665	0.286	$B_z = 2/3$	N_2^+
22.008	0.714	--	--	0.577	0.259	$3/2B_z + 1/2B_r = 1$	N_2^+
20.419	0.662	--	--	0.523	0.239	$B_z + 2B_r = 1$	N_2^+
19.914	0.646	--	--	0.507	0.233	$3/2B_z + B_r = 1$	N_2^+
19.714	0.639	--	--	0.500	0.231	$B_z = 1/2$	N_2^+
18.704	0.606	--	--	0.469	0.218	$B_z + 5/2B_r = 1$	N_2^+
17.988	0.583	0.908	--	0.997	0.335	$B_z = 1$	H_2O^+
17.714	0.574	0.894	--	0.890	0.330	$B_r = 1/3$	H_2O^+
17.420	0.565	0.879	--	0.841	0.324	$B_z + 1/2B_r = 1$	H_2O^+
17.146	0.556	0.865	--	0.806	0.319	*	H_2O^+
16.451	0.533	0.830	--	0.403	0.192	? $2B_z + B_r = 1$?	N_2^+
16.199	0.525	0.817	--	0.715	0.299	$B_z + B_r = 1$	H_2O^+
15.599	0.506	0.787	--	0.670	0.288	$B_z = 2/3$	H_2O^+
14.746	0.478	0.744	--	0.614	0.271	? $B_z + 3/2B_r = 1$?	H_2O^+
13.999	0.454	0.706	0.908	0.997	0.335	$B_z = 1$	N^+
13.788	0.447	0.696	0.894	0.890	0.330	$B_r = 1/3$	N^+
13.546	0.439	0.683	0.878	0.839	0.324	$B_z + 1/2B_r = 1$	N^+
13.346	0.433	0.673	0.865	0.806	0.319	*	N^+
13.115	0.425	0.662	0.850	0.523	0.239	$B_z + 2B_r = 1$	H_2O^+
12.883	0.418	0.650	0.835	0.511	0.235	$B_z = 1/2$	H_2O^+
12.515	0.406	0.631	0.811	0.705	0.297	$B_z + B_r = 1$	N^+
12.136	0.393	0.612	0.787	0.670	0.288	$B_z = 2/3$	N^+
11.041	0.358	0.557	0.716	0.581	0.260	$3/2B_z + 1/2B_r = 1$	N^+
10.273	0.333	0.518	0.666	0.527	0.240	$B_z + 2B_r = 1$	N^+
10.041	0.325	0.506	0.651	0.512	0.236	$3/2B_z + B_r = 1$	N^+
9.915	0.321	0.500	0.643	0.504	0.233	$B_z = 1/2$	N^+
8.410	0.272	0.424	0.545	0.413	0.196	$3/2B_z + 2B_r = 1$	N^+
7.021	0.227	0.354	0.455	0.337	0.163	$5/2B_z + B_r = 1$	N^+
6.916	0.224	0.349	0.448	0.331	0.160	$B_z = 1/3$	N^+
6.274	0.203	0.316	0.406	0.298	0.145	? $3B_z + 1/2B_r = 1$?	N^+
6.095	0.197	0.307	0.395	0.289	0.141	$B_z = 2/7$	N^+

* indicates an undetermined value; ?? indicates an uncertain determination

the GC/MS alternative. The sensitivity and resolution required for this application are limiting factors. The amount of ethylene is unlikely to rise beyond the ppm level, thus quantifying trace ethylene is particularly challenging without using chromatography to separate it from the more abundant isobar. At the same time, the two peaks are only 0.025 Da apart, which requires high resolving power with minimal peak distortion from space charge of higher-order fields effects.

The increased drive frequency of the UF-IT lowered its effective upper mass limit to 62 Da. Ideally all 65,536 DAC steps could then be used over this narrow mass range, providing over 1000 steps per Da, and 1 milli-dalton resolution. In reality, the RF DAC could only be updated every 30 μ s, and at a scan rate of 0.06 ms/Da this translated to two RF steps per Da, far from the ideal 1000 steps. By slowing down the scan rate to 3 ms/Da, 100 RF DAC steps could be made per Da with 0.01 Da resolving power, which could resolve the isobars.

Figure 5-16a shows the high-resolution spectrum of pure nitrogen. The peak at 27.993 is from nitrogen ions ejected at $q_z = 0.90805$, while all others are from nitrogen ions ejecting through black holes. In the pure ethylene spectrum of Figure 5-16d ions leaving at $q_z = 0.90805$ appear at 28.013 Da. The measured difference of 0.02 ± 0.01 Da matches the true difference of 0.025 Da.

Higher-order resonance effects complicated the spectrum. Ejection of ethylene ions through black holes close to $q_z = 0.908$ overlapped with nitrogen ion peaks, making the two indistinguishable. When ethylene was added, the total ion intensity significantly decreased. Likely most, if not all, of the nitrogen ions were neutralized by charge-exchange with ethylene (RE of N_2^+ at 15.3 eV¹¹⁰ > IE of $C_2H_4^+$ at 10.5 eV¹²⁰). Ample

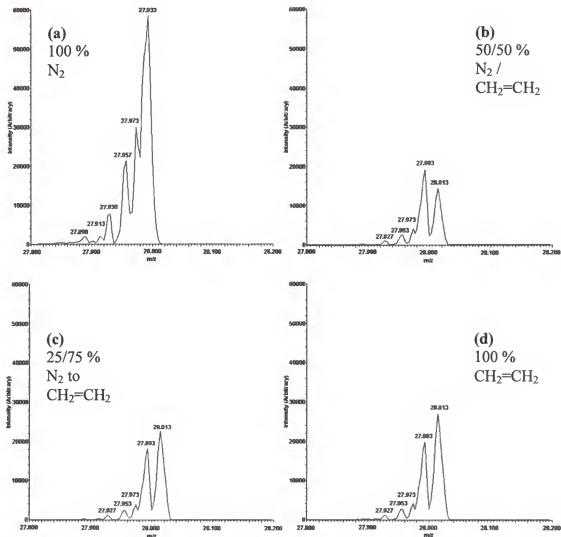


Figure 5-16. Mass spectra of the isobars, nitrogen and ethylene. Using a 3 ms/Da scan rate, the nitrogen ion peak observed at 27.933 Da in (a) was distinguished from the ion peak of pure ethylene observed at 28.013 in (d). In both cases, a series of peaks to the left of the main peak was observed, caused by nonlinear resonance effects near the $\beta_z = 1$ boundary. Nonlinearly ejected ethylene ions overlapped the ion peaks of nitrogen, making the two indistinguishable in the spectra (b) and (c). Despite this complication, the nitrogen ion signal of (a) and the ethylene ion signal of (d) are distinctly different. The mass difference was 0.2 ± 0.1 Da, which matched the actual difference of 0.25 Da.

time existed for the completion of this reaction because of the slow 3 ms/Da scan rate. This explains the miniscule changes observed when increasing the ethylene from 50% to 75%, and to 100% ethylene, shown in Figures (b), (c), and (d), respectively.

Despite complications with sensitivity, it is apparent from Figure 5-16 that spectra from the UF-IT were different for pure nitrogen and pure ethylene, with a resolving power of 0.02 ± 0.01 Da. The demonstrated high-resolution was achieved without the use of resonant ejection, which was stipulated as a requirement for high-resolution on commercial QITMS instruments.^{166,167}

Conclusions

The operation of the UF-IT has been optimized for analysis of hydrogen, helium, oxygen, and argon in a nitrogen background. The optimal ion trap pressure was 7.5×10^{-6} torr at 30°C. An AHGD scan function illustrated in Figure 5-17 was designed using the results of the parameter evaluation detailed in this Chapter. The complete scan lasted for 14 ms and was divided into two segments for independent analysis of the lighter masses, scanned between 1 and 5 Da, and heavier masses, scanned between 30 and 42 Da. The ionization period was increased to 70% of the total scan time, which raised the duty cycle for improved analytical performance. Seventy scans (termed μ -scans), acquired during the 1 s AHGD update period, were averaged to increase precision. Data were further smoothed using a three-point running average.

The AHGD scan used a scan rate of 0.06 ms/Da, which still provided unit mass resolution at three times the Finnigan GCQ scan rate. High-resolution was also achieved by slowing the scan rate of the UF-IT in an experiment to resolve isobars at 28 Da, but complications from higher-order field effects and ion-molecule reactions prevented

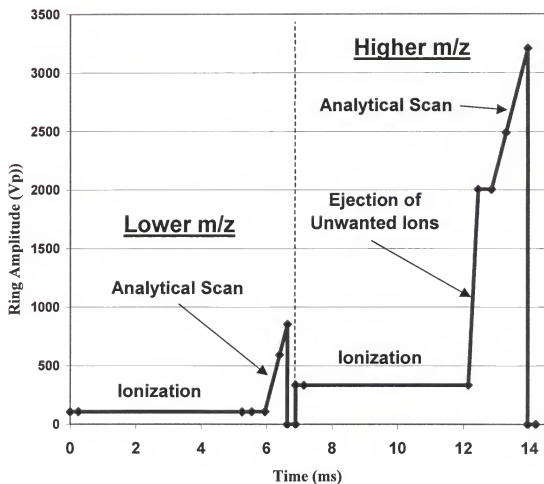


Figure 5-17. Optimized UF-IT scan function. The scan is made up of the sections: ionization, post-ionization, the analytical scan, and post-scan activities as marked by the blue diamonds. The plot indicates the duration and RF amplitude used for each section. The scan uses separate optimized segments for the lower and the higher m/z values.

quantitative analysis of isobar mixtures. The primary limitation of the UF-IT's resolving power was the slow update rate of the RF DAC, which at 0.03 ms required a 3 ms/Da scan rate to provide 0.01 Da mass resolution. A quicker RF DAC update rate would permit high-resolution at faster scan rates, thereby reducing the effects of ion-molecule reactions and nonlinear resonance.

Similar optimization was performed on the modified PolarisQ for the AHGD application, but was not detailed in the chapter. The PolarisQ scan function depicted in Figure 5-18 paralleled that of the UF-IT. A 3 ms ion injection period replaced the 5 ms ionization period used on the UF-IT, because of the PolarisQ's external ion source. The scan rate was kept the same at 0.06 ms/Da scan, with similar scan segments of 1 to 5 Da for hydrogen and helium ions, and 28 to 42 Da for oxygen and argon. The PolarisQ scan function lasted for 14 ms with 70 μ -scans averaged together per second just as on the UF-IT. Having optimized both QITMS instruments for the AHGD application, the next step was to evaluate their analytical performance, which is presented in Chapter 6. QITMS is compared with other mass analyzer technologies that were evaluated in Chapter 2.

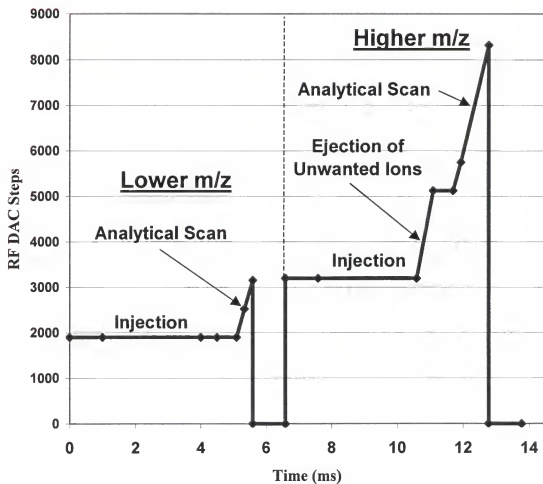


Figure 5-18. Optimized PolarisQ scan function. The scan is made up of the sections: ion injection, post-injection, the analytical scan, and post-scan activities as marked by the blue diamonds. The plot indicates the duration and RF DAC value used for each section. The scan uses separate optimized segments for the lower and higher m/z values.

CHAPTER 6 PERFORMANCE EVALUATION OF QITMS

Introduction

Quadrupole ion trap mass spectrometry recently has become popular in many applications; however, analysis of lightweight gases is still performed with linear quadrupole, sector, and time-of-flight mass analyzers.¹⁷¹ The research presented in this dissertation has focused on the unique development of QITMS instrumentation for monitoring and quantifying lightweight gases. In this chapter QITMS is evaluated and compared to other mass analyzers for the Advanced Hazardous Gas Detection (AHGD) project – to quantify trace amounts of hydrogen, helium, oxygen, and argon in a nitrogen matrix.

Techniques for comparing instrumental performance have been standardized in the literature.¹⁷² The methodology used for the AHGD project was adapted specifically by NASA to determine the viability of mass analyzer technology as Space Shuttle flight safety equipment. Analytical calculations were based on standardized methods, such as use of the IUPAC approach for determination of detection limits¹⁷³ with procedures designed for simulating launch preparation conditions.

The most recent data for QITMS instruments is presented, with improved performance relative to previous reports by the author and co-workers in the literature.^{174,175} The results presented for other mass analyzer technologies from Chapter 2 are also different from those previously reported.¹⁷⁵ In this case the data is acquired and processed solely by the author, which reduced errors in the comparison.

Experimental

For an effective comparison, the methodology and evaluation conditions must remain as constant as possible. This was difficult in this case, because the QITMS evaluation and that of the other instruments was performed two years apart. Though attempts were made to maintain uniformity, significant differences existed that needed to be addressed. The QITMS evaluation was conducted at the University of Florida, while the other instruments were evaluated at Kennedy Space Center. Environmental changes were considered to have a minimal affect, since both labs were within similar humid Floridian climates and were climate controlled. Daily fluctuations in temperature and humidity were comparable, because in both cases experiments were conducted during the fall season. Whenever possible, instruments were optimized for in-house use.

Analytical Methodology

The AHGD methodology outlined and used in Chapter 2 was also followed for evaluation of the QITMS instruments. This included the AHGD test procedure, the use of the two-point calibration plot, and the methods for determining detection limits, accuracy, precision, response times, and recovery times. The tests were conducted with three different gas samples: pure nitrogen, termed zero gas (ZG); a mixture of hydrogen, helium, oxygen, and argon each at 500 ppm in a balance of nitrogen, termed test gas (TG); and a mixture of the same gases each at 5000 ppm in a balance of nitrogen, termed span gas (SG).

Two additional AHGD criteria were also determined for the UF-IT:

Two-hour drift – for evaluating system stability. The system was first initialized by running ZG for 15 minutes. The test began by running ZG, TG, then SG in series, each for 3 minutes, which would later be used to produce a calibration plot. Afterward, ZG

was sampled for the remainder of a two hour period, which was followed by a three minute run of TG. Ten data points were averaged from the initial ZG signal and another ten from the last three minutes of the two-hour ZG period. The two average values were then converted to concentration units using the calibration plot. The difference in concentration was reported as the 2hr-ZeroDrift in ppm. Ten data points were also averaged and converted to concentration units from each of the TG periods. In this case, the difference in concentration was reported as a percent value using Equation 6-1 as the 2hr-TestDrift, which was required to be within $\pm 10\%$ for all four gases.

$$2hr - TestDrift = \frac{[TG]_f - [TG]_i}{[TG]_i} * 100\% \quad (6-1)$$

Linear dynamic range – for determining response characteristics to changes in analyte concentration. The dynamic range required by the AHGD project extended over five orders in magnitude, from a few ppm to a few percent. Available gas standards limited the maximum concentration used for the UF-IT dynamic range evaluation to 2.5% of each gas, but with the gas dilution system (GDS – detailed in Chapter 3) a wide range of intermediate concentrations could be analyzed. First, the system was initialized by running ZG for 15 minutes. Then the concentration of hydrogen, helium, oxygen, and argon was increased stepwise between 0 and 2.5 % of each in nitrogen. The ion signal at each concentration was then plotted to evaluate linearity.

Sample Delivery

All of the gas samples for the QITMS evaluation were produced using the GDS apparatus (Figure 6-1). As demonstrated in Chapter 3, the GDS provided comparable performance with improved flexibility compared to the discrete bottle method employed

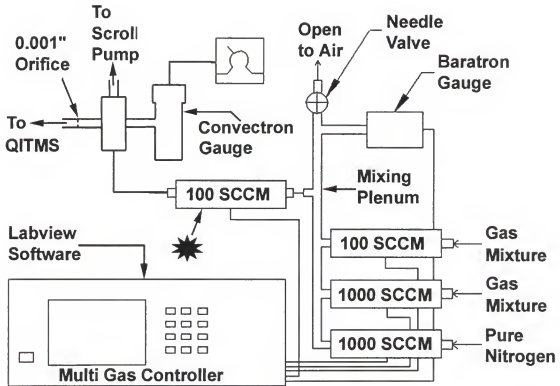


Figure 6-1. Revised diagram of gas dilution system (GDS). An MKS 100 SCCM mass flow controller (indicated by the star) replaced a Granville-Phillips 203 variable leak valve for improved inlet pressure regulation.

in evaluating the other mass analyzers in Chapter 2. A wide range of concentrations could be produced by diluting a gas standard of hydrogen, helium, oxygen, and argon each at 2.5% in nitrogen with a second gas stream of pure nitrogen. Total gas flow through the mixing plenum was regulated to 500 SCCM at a pressure of 950 torr. The mass spectrometer inlet was regulated to a pressure of 5-torr, which provided an optimal ion trap pressure of 7.5×10^{-6} torr.

Instrumentation

The UF-IT and the PolarisQ QITMS instruments were both evaluated for the AHGD application using the optimized operational conditions determined in Chapter 5. The UF-IT incorporated an internal ionization source with an open ion trap configuration, while the PolarisQ used an external ionization source that required a collision gas inside the ion trap for adequate trapping efficiency. Both used commercial ion traps operated at higher drive frequencies, 2.5 and 2.8 MHz respectively for the UF-IT and PolarisQ. This increased the potential-well depth to trap the lightweight ions of hydrogen and helium; however, this also reduced the upper mass limit of the instruments to below 100 Da.

Results and Discussion of QITMS Performance

In earlier reports of UF-IT performance,^{174,175} the detection limits for oxygen and argon were worse than their respective AHGD requirements of 25 and 10 ppm, while those for hydrogen and helium were better than their requirements of 25 and 100 ppm. The UF-IT was less sensitive to higher mass ions, producing poorer detection limits. This was recently resolved through optimization of the electron filament bias potential; however, afterward a significant amount of $1/f$ noise¹⁷⁶ was observed in the oxygen and argon ion signals.

The 1/f noise went unnoticed previously because of the poor sensitivity. Now drifting occurred that was significant over the course of the analysis period. The drifting corresponded to changes in the background pressure. Similar behavior was reported earlier in Chapter 4 when a Granville-Phillips 203 variable leak valve was used to admit gas into the auxiliary port. The GDS apparatus also used a 203 leak valve that regulated the mass spectrometer inlet pressure. The inlet pressure was observed drifting over long periods; therefore, the valve was replaced by a MKS 100-SCCM mass flow controller (MFC) as shown in Figure 6-1 with automatic servo-control for improved conductance stability. The pressure and subsequently the ion signals no longer drifted as before, thereby improving the accuracy of the analytical evaluation.

Custom Built QITMS

The latest performance characteristics of the UF-IT are presented in Table 6-1. The detection limits for hydrogen, helium, oxygen, and argon were all better than the AHGD requirements of 25, 100, 25, and 10 ppm, respectively. The accuracy and precision of quantification for all four gases were within the AHGD specifications of $< \pm 10\%$ error and $< \pm 5\%$ deviation. As well, all response and recovery times were quicker than the respective 10 s and 30 s requirements. Only the 2hr-TestDrift value for hydrogen exceeded the AHGD requirement of $< \pm 10\%$ change, but this was more likely caused by poor pumping than by the mass analyzer. Similar problems were reported in Chapter 3 when a backing pump had to be replaced.¹⁷⁴ Hydrogen stability may be further improved by replacing the high-vacuum turbo-drag pump with one that has a better hydrogen compression ratio.^{177,178}

Table 6-1. Custom built (UF-IT) QITMS analytical performance

Analytical criteria	Hydrogen	Helium	Oxygen	Argon
Detection limit (ppm)	12	12	7	2
Accuracy (% error)	2.6	4.3	4.7	3.8
Precision (% deviation)	2.1	2.2	0.8	0.8
Response time (s)	8	7	8	8
Recovery time (s)	6	6	8	6
2hr-ZeroDrift (ppm)	148.9	0.1	20.2	5.9
2hr-TestDrift (%Δ)	28.5	0.1	4.3	1.6

Figure 6-2 depicts the UF-IT response while sampling different concentrations from pure nitrogen up to 2.5% of each analyte. While other performance criteria focused on signal linearity below 5000 ppm, this test demonstrated the effectiveness of the UF-IT for quantifying higher concentrations. The plot shows that the response remains linear throughout the tested concentration range with R^2 values of 0.9989 or better for each analyte. The response characteristics for concentrations above 2.5% could not be determined using the available gas standards. However, linearity beyond 2.5% was less critical since a leak of that magnitude would already be considered serious, at which point monitoring becomes more qualitative than quantitative.

Modified Commercial QITMS

Previously, PolarisQ performance results were reported for oxygen and argon only, since the instrument had not yet been modified for lightweight gas analysis.¹⁷⁵ The drive frequency was raised to 2.8 MHz thereby increasing the potential-well depth for allowing lower mass ions to be trapped. Afterward, the success of the modifications was confirmed by the detection of ions of the helium collision gas, but because a high helium pressure was used inside the ion trap, trace detection of helium was not possible. Further, ion signals for hydrogen were not observed at all, because these ions were scattered upon collision with the abundant, more massive, helium neutrals.

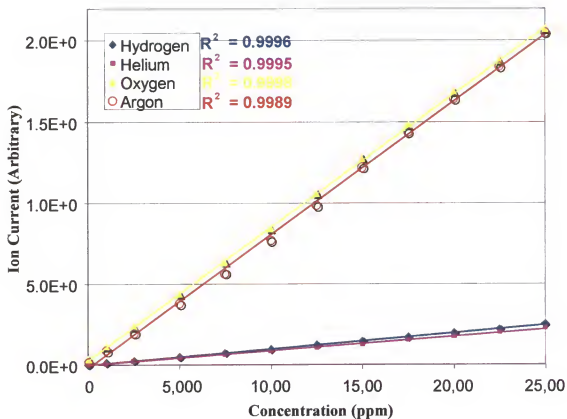


Figure 6-2. Plot of UF-IT response over the concentration range from 0 to 25,000 ppm (2.5%) for each AHGD analyte in nitrogen. Response remained linear through the range with R^2 values of 0.9989 or better.

Trace helium detection was not improved when the collision gas was changed to hydrogen. The considerable pressure of the external ion source promoted rapid loss of helium ions through charge-exchange with nitrogen or hydrogen, which minimized sensitivity. Hydrogen ions were now observed only as the protonated H_3^+ ion, but the high collision gas pressure prevented trace detection. Removal of the collision gas all together was of no help, since it resulted in complete loss of signal from the poor trapping efficiency of injected ions without collisional cooling. Thus, despite successfully decreasing the low-mass cutoff of the PolarisQ, the instrument was unable to be used with the lighter mass analytes of the AHGD project.

Modifying the PolarisQ had an additional impact on the analytical performance with oxygen and argon. Table 6-2 lists PolarisQ results from both before and after the modifications were made. Sensitivity to oxygen and argon decreased afterwards, which worsened detection limits. At the same time, accuracy improved for both gases; however, this was not attributed entirely to the PolarisQ modifications. The stability of the inlet pressure had also been improved when the 203 leak valve was replaced with the MFC, performed after the PolarisQ had been modified.

Table 6-2. Modified commercial (PolarisQ) QITMS analytical performance

PolarisQ Performance criteria	Before modification		After modification	
	Oxygen	Argon	Oxygen	Argon
Detection limit (ppm)	8	3	20	27
Accuracy (% error)	39.8	9.8	3.9	4.8
Precision (% deviation)	0.5	2.9	1.5	2.5
Response time (s)	27	24	25	21
Recovery time (s)	25	26	22	24

The response and recovery times remained relatively unchanged, since they primarily depended on the gas flow through the instrument, which had not been altered; however, the PolarisQ took four times as long as the UF-IT to respond and recover to a

changing gas concentration. The external ion source volume was closed tighter, and operated at a higher gas pressure than the source of the UF-IT. Therefore, with a lower conductance, it took longer to replace the gas inside the volume. This fact, combined with the inability to efficiently trap ions without a collision gas, made the external ion source ineffective for the AHGD application.

Performance Comparison

With an internal ionization source, the UF-IT was capable of analyzing all four AHGD analytes, demonstrating that QITMS could be used for lightweight gas analysis. The UF-IT performance is compared with the PolarisQ and the other mass analyzers in Figures 6-3 through 6-7. Though the PolarisQ was faulted by its inability to detect hydrogen and helium, its quantitative performance for oxygen and argon is better than many of the other instruments. The UF-IT performed even better, matching if not exceeding the performance of the linear quadrupole, which was the best performing instrument in Chapter 2. The two are best distinguished by their update speed. Figure 6-8 shows the update period for each evaluated instrument. The UF-IT provided parallel analytical performance at six times the rate of the linear quadrupole. This was significant, since the primary purpose of the AHGD project was to reduce time delays.

The UF-IT can also be slowed for other applications when speed is less important. Signal fluctuation is reduced, since more data points are averaged, thereby improving detection limits. Thus, at the same speed, the QITMS would perform better than the linear quadrupole. This is primarily from the greater duty cycle of the QITMS, with its ability to store ions, specifically for applications that require monitoring of more than one species. The QITMS is able to store ions of different m/z at the same time, while the

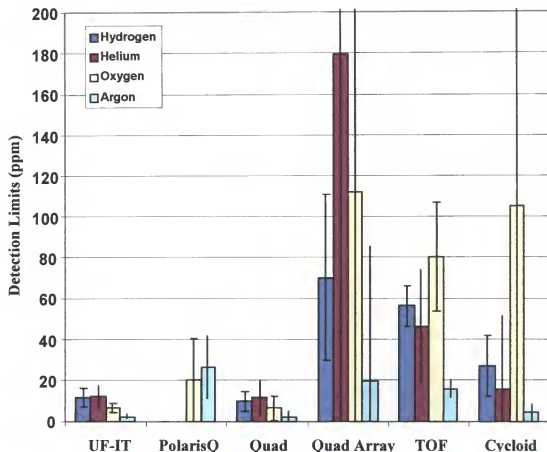


Figure 6-3. Plot of detection limits for six mass analyzers evaluated for the AHGD application. The two QITMS instruments, UF-IT with internal ionization and the PolarisQ with external ionization, are compared with four other mass analyzers previously evaluated in Chapter 2. The UF-IT and linear quadrupole (Quad) have similar detection limits, and are the only instruments to meet the AHGD requirements for all four gases. Detection limits are calculated based on a S/N ratio of three, with a 95% confidence interval indicated by the error bars.

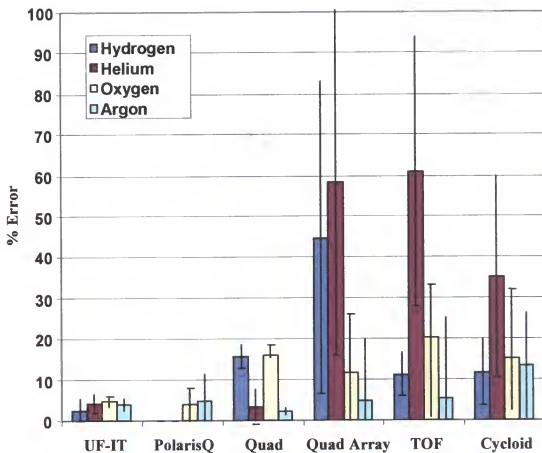


Figure 6-4. Plot of quantification error for six mass analyzers evaluated for the AHGD application. A two point calibration plot was used to calculate the concentration of a test sample of known concentration. The percent error of the quantified value is reported for all four gases. The UF-IT is the only instrument to meet the AHGD requirement, $< \pm 10\%$, for all gases. The 95% confidence interval is indicated by the error bars.

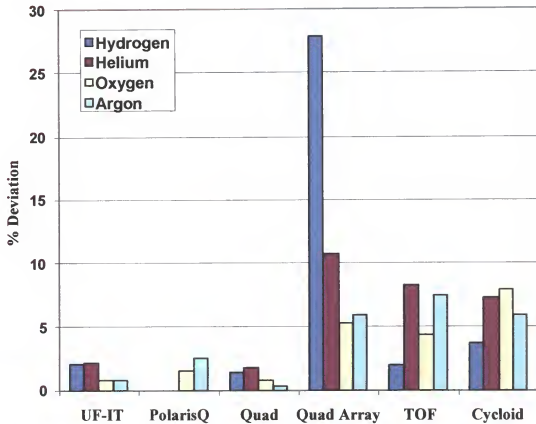


Figure 6-5. Plot of precision for six mass analyzers evaluated for the AHGD application. Deviation of the calculated concentrations of three-test gas samples is reported as a percent value. The UF-IT and the linear quadrupole meet the AHGD requirement of $\leq \pm 5\%$ deviation.

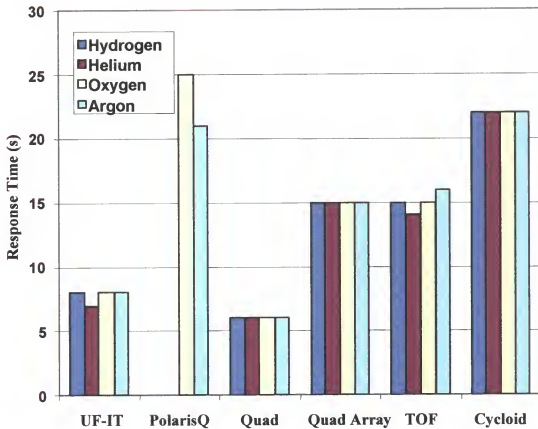


Figure 6-6. Plot of response times for six mass analyzers evaluated for the AHGD application. Measured is the time required to reach 95% of final equilibrium value when switching from pure nitrogen to 500 ppm of each analyte in nitrogen. The UF-IT and the linear quadrupole meet the requirement of < 10 s.

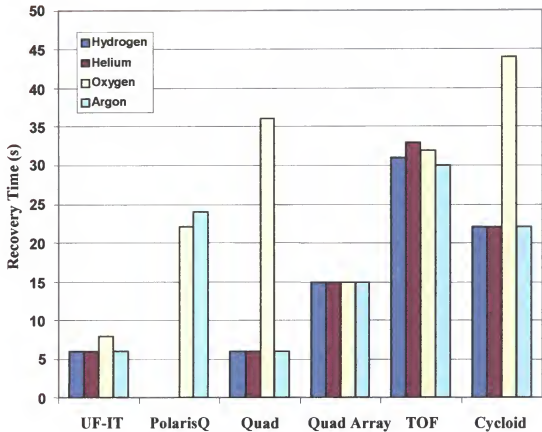


Figure 6-7. Plot of recovery times for six mass analyzers evaluated for the AHGD application. Measure of the time required to reach 95% of final equilibrium value when switching from 5000 ppm to 500 ppm of each analyte in nitrogen. The UF-IT and quadrupole array instruments met the requirement of < 30 s.

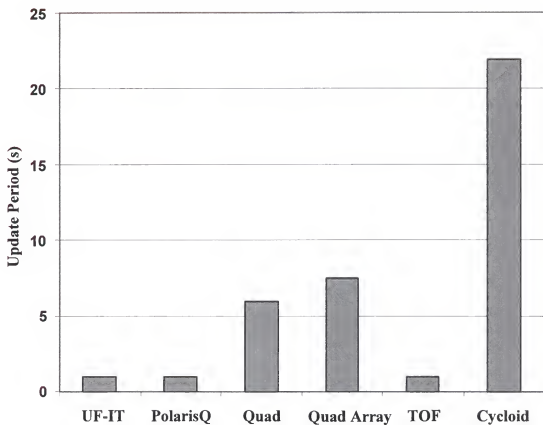


Figure 6-8. Plot of the update periods for six mass analyzers evaluated for the AHGD application. Both QITMS instruments and the TOF met the NASA requirement of a 1 Hz update rate.

linear quadrupole must continually scan. QITMS would be competitive with conventional residual gas analyzer (RGA) technology, particularly for such applications.

RGAs are commonly used in the microelectronic manufacturing industry to detect trace contaminants. Often, these species are of higher mass-to-charge than argon ions, requiring a greater high-mass cutoff than the AHGD application. Figure 6-9 shows the high-mass cutoff values for the evaluated analyzers. The linear quadrupole RGA reaches 100 Da, greater than that of the UF-IT; however, this is not a reflection of QITMS capability. The cutoff of the UF-IT was limited to 62 Da because of the poor tuning of the RF amplifier used. The drive frequency was increased for lightweight gas analysis, which forced operation of the RF amplifier out of its design specifications, which reduced the gain. An amplifier designed to operate at the new drive frequency could provide the same gain as the commercial GCQ; thus with a maximum output of 8500 V_p the high-mass cutoff would increase to 130 Da.

Conclusions

QITMS instrumentation was evaluated for the AHGD application. The use of an external ionization source was found to be counterproductive for lightweight gas analysis, but with internal ionization QITMS provided excellent performance relative to other mass analyzer technologies. The internal ionization QITMS and the linear quadrupole both delivered the best analytical performance, except the QITMS was six times faster. This QITMS was the only system to operate at the required 1 Hz update rate, and still meet the analytical requirements for detection limits, accuracy, precision, response time, and recovery time. Therefore, QITMS was well suited for the AHGD project.

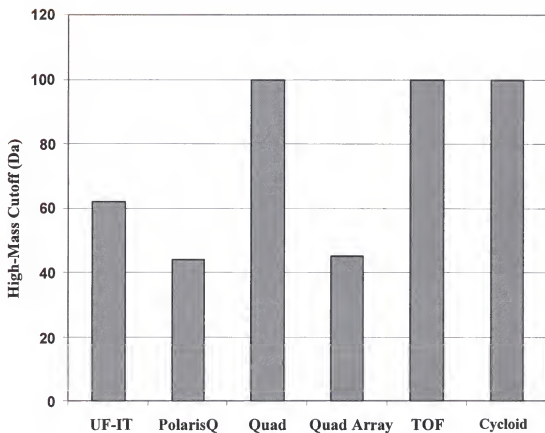


Figure 6-9. Plot of high-mass cutoffs for six mass analyzers evaluated for the AHGD application. All six instruments met the required 40+ Da cutoff of the AHGD project, though the cutoffs of the two QITMS instruments were lower than most other analyzers, limiting their applicability to other gas analysis applications.

CHAPTER 7

CONCLUSIONS AND FUTURE DIRECTIONS

The quadrupole ion trap mass spectrometer (QITMS), when it was patented nearly fifty years ago, was envisioned as a tool for trace analysis of lightweight gas mixtures. Yet it took twenty-five years before the QITMS became commercially available, at which point, with the advent of new ionization techniques (e.g., ESI and APCI) and the coupling of chromatography, QITMS became popular for complex environmental, pharmaceutical, and biological applications involving analytes of ever-increasing size. Ironically, lightweight gas mixture analysis by QITMS has been overlooked. Linear quadrupole, sector, and time-of-flight mass spectrometers have all been commercialized for such applications, which require compact, inexpensive, simple mass analyzers, often referred to as residual gas analyzers (RGAs). In this dissertation the viability of QITMS as an RGA has been explored, with a focus specifically on the analysis of hydrogen, helium, oxygen, and argon mixtures in a nitrogen matrix.

The National Aeronautics and Space Administration (NASA) manned space program depends entirely on the Space Shuttle for transportation into space. The Space Shuttle began operation in the early 1980s, and will continue to service the International Space Station for at least another ten years. The Space Shuttle main engines generate thrust by combusting 1.8 million liters of liquid hydrogen with 0.7 million liters of liquid oxygen. The spacecraft must be constantly monitored for leaks, because of the explosive nature and sheer volume of fuel. Mass spectrometers have been used for this purpose since the beginning of the Space Shuttle program, but have been remotely located because of their

large size and sensitivity to shock. Gas sampled from inside the Space Shuttle must travel long distances, delaying analysis by as much as 45 s. In addition, the number of simultaneously sampled locations is limited to two by the number of available analyzers, because of their large size. In the year 2000, NASA initiated the Advanced Hazardous Gas Detection (AHGD) project to develop a small, rugged, fast mass spectrometer to monitor the concentration of hydrogen, helium, oxygen and argon in the nitrogen-purged compartments of the Space Shuttle. The aim is to place multiple units next to the Space Shuttle, thereby reducing delays for real-time analysis with improved redundancy.

Commercial QITMS instrumentation cannot perform this application, since ion trap operating parameters have been selected to extend the upper-mass limit, which sacrifices low-mass analysis. Potential-well depth is proportional to mass-to-charge; therefore, the potential-well is energetically too low to effectively trap hydrogen and helium ions. Two QITMS instruments were modified (Chapter 3) to increase the potential-well depth by increasing the RF drive frequency and in doing so decrease the low-mass cutoff of the instrument. The first was designed for internal ionization, which for this application was determined to be superior over the external ionization source of the other QITMS. A collision gas that would interfere with analysis of lightweight gases was not required for internal ionization. This type of source was simpler, more compact, with a greater gas conductance for more rapid sample replacement.

The primary analytical advantage of QITMS is the high duty cycle afforded by storing ions. Ions of different m/z values are accumulated throughout the majority of the analysis period, while mass selection occurs during a comparatively short period. Other mass analyzers, such as the linear quadrupole, are continually scanning so that ions of a

single m/z value are sampled at a given time while all other ions are lost. The difference in duty cycle is increased for applications that require analysis of more m/z values. Therefore, QITMS provides improved performance for the AHGD application.

Ion-molecule reactions are the Achilles' heel of QITMS. At a pressure of 10^{-6} torr and with ion storage times in the milliseconds, all ions will statistically collide with a neutral at least once. If energetically favorable, a majority of these collisions will result in ion-molecule reactions. In Chapter 4, AHGD analytes were found to favorably react with the abundant nitrogen and water in the background. Reactions progressed by charge-exchange, proton transfer, and hydrogen atom transfer reaction mechanisms with high rate constants of 10^{-9} $\text{cm}^3/\text{s-molecule}$

Ion-molecule reactions adversely affect the sensitivity of QITMS. Pressure and time parameters were optimized (Chapter 5) to diminish the negative influence of ion-molecule reactions, while maximizing analytical performance. A segmented scan routine was used where the two lower-mass ions were grouped independently of the two higher-mass ions since each group required different operating conditions. This lowered the duty cycle, but greatly improved sensitivity. Compromises in pressure (7.5×10^{-6} torr) and in ionization time (5 ms) were selected, while the time spent on all post-ionization events was minimized. The optimized scan was just over 14 ms long, permitting 70 independent scans per second at the required 1 Hz update rate.

The analytical performance of the QITMS for the AHGD application was evaluated in Chapter 6. NASA requirements for detection limits, accuracy and precision of quantification, and response and recovery time to a changing gas concentration were all met. Of the other types of mass analyzers evaluated in Chapter 2, only the linear

quadrupole came close to the performance of the QITMS, but it had an update rate that was six times slower than that of the QITMS.

The amount of drift in the hydrogen ion signal was the only QITMS result which failed to meet AHGD requirements. Such drifting was observed to a greater extent (Chapter 3) until the backing pump was replaced with one having a lower base pressure. This improved the hydrogen compression; however, further improvement would require replacement of the turbo-drag high-vacuum pump with one having a greater hydrogen compression ratio.

The AHGD project requires a compact and lightweight instrument. Figures 7-1 and 7-2 compare the size and weight of the six evaluated instruments. Only the quadrupole array instrument met the size requirement of 35,000 cm³ while none of the instruments met the 10 kg weight requirement. Electronics were the bulkiest components, which can be reduced by use of surface-mount technology. This would also decrease power consumption, which will allow smaller power supplies to be used. Power demands can be further reduced by use of a better-tuned RF circuit designed for the higher RF drive frequency. The heaviest components were the vacuum pumps. Vacuum technology has come a long way in recent years, but advancements have been focused on larger pumps with increased throughput and faster speeds;¹⁷⁹ though recently, a few startup companies and governmental labs have been investigating miniature vacuum technology.^{180,181}

The prototype QITMS instruments were among the largest and heaviest instruments evaluated, since components were used from benchtop-size commercial instruments, rather than being designed for compactness. Therefore, there is ample room to reduce

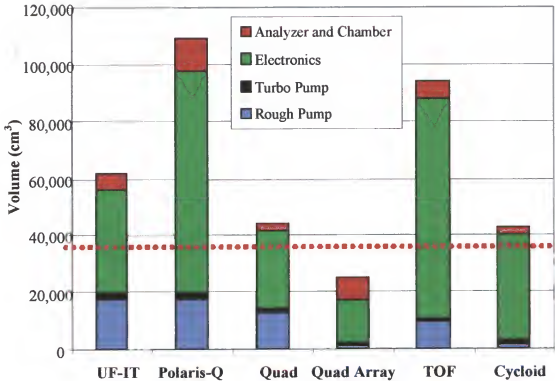


Figure 7-1. Plot of system volume for six mass spectrometer systems evaluated for the AHGD application. System volume is subdivided into four categories: the size of the vacuum chamber, which contains the source, mass analyzer, and detector; the system electronics and power supplies, which does not include a personal computer; the turbo-drag high vacuum pump and the associated controller; and the backing pump. The dotted line indicates the 35,000 cm³ AHGD required volume. (Adapted from Arkin, C. R.; Griffin, T. P.; Ottens, A. K.; Diaz, J. A.; Follistein, D. W.; Adams, F. W.; Helms, W. R. *J. Am. Soc. Mass Spectrom.* Vol. 13, 2002; Figure 9, p. 1010.)

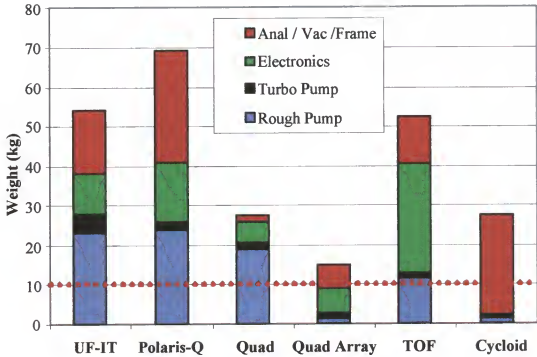


Figure 7-2. Plot of system weight for six mass spectrometer systems evaluated for the AHGD application. System weight is subdivided into four categories: mass analyzer, vacuum chamber, and chassis; electronics and power supplies; turbo-drag pump and associated controller; and backing pump. The dotted line indicates the 10 kg required weight of the NASA AHGD project. (Adapted from Arkin, C. R.; Griffin, T. P.; Ottens, A. K.; Diaz, J. A.; Follistein, D. W.; Adams, F. W.; Helms, W. R. *J. Am. Soc. Mass Spectrom.* Vol. 13, 2002; Figure 10, p. 1011.)

system size, which will be the focus for the next generation instrument. A current QITMS prototype, designed with internal ionization, is shown in Figure 7-3. The ion trap (subsection of box A) is only 0.2% of the total system volume, but it is enclosed in a vacuum chamber (box A) that is ten times larger. Reducing the internal ion trap dimensions, r_0 , and z_0 , by a factor of two will decrease the volume of the vacuum chamber by approximately a factor of eight. A smaller vacuum chamber requires less pumping; therefore, the vacuum pumps could also be reduced in size. This is particularly significant since the turbo-drag pump (box C) and the backing pump (box E) are together 28.5% of the total system volume.

A smaller ion trap requires a higher RF drive frequency, and thus the RF coil will also be reduced in size. The current 2.5-MHz RF coil (subsection of box B) is only 0.2% of the total system volume, but the coil enclosure (box B) is much larger at 6.5%, because the box was designed for a larger 1-MHz RF coil. If the box were reduced to fit the current coil, it would be reduced to 2% of total system volume, which would be further reduced for the smaller coil of a reduced-size ion trap. However, components in boxes A through E account for only 60% of the total system volume. The remaining 40% is empty space, which is required only in part to run wires and conduct air for cooling. Thus, a reduction in empty space would be a major concern for the next generation prototype.

A miniaturized QITMS with its high duty cycle would also be competitive with present day RGA technology. The instrumentation is simple, requiring only three electrodes and a single-phase scanning RF potential. A linear quadrupole in comparison requires two-phases of RF and a DC potential, while a sector instrument uses magnetic

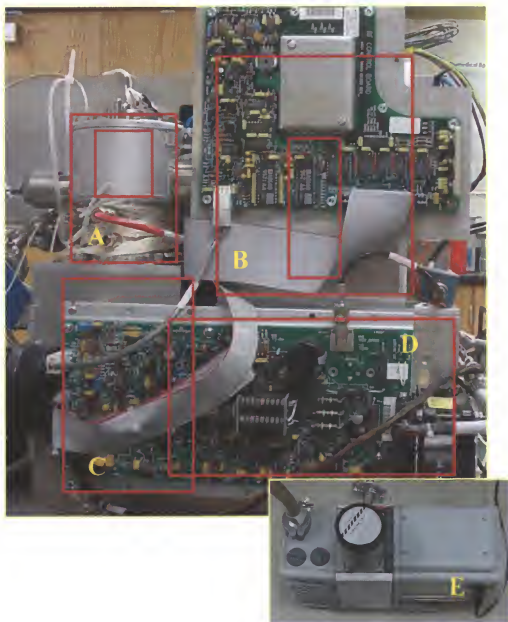


Figure 7-3. A sectioned image of the UF-IT QITMS instrument to evaluate the relative volume of different components. Components in sections A through E comprise nearly 40% of the total system volume: A) the vacuum chamber (2%) with the ion trap (0.2%) indicated as a subset; B) the RF coil box (6.5%) with the RF coil (0.2%) indicated as a subset; C) the turbo-drag pump and associated controller (5%); D) power supplies (8%); and (E) the rotary-vane backing pump (20%). Another 20% is taken up by electronics, leaving 40% of empty space that in part is used for running cables and conducting air for cooling.

in addition to electric fields. Ionization can be performed inside the ion trap, whereas other analyzers require external ion sources that increase the size and complexity of the instrumentation. Ion traps are easily sandwiched together, whereas linear quadrupoles require precision alignment to maintain a uniform field along its entire length.

The stability of the ion trap assembly also makes it rugged, another AHGD project requirement. In actuality, the components most susceptible to vibration are likely to be the high-vacuum turbo-drag pump and the electron filament, which are common to all the mass spectrometers evaluated. Future work will include shake-table tests, where instruments are exposed to vibration along each axis of motion of variable intensity and frequency. Smaller turbo pumps will likely be more susceptible to vibration, since they use faster rotational speeds and have tighter machining tolerances. Hot-filament electron sources will potentially need to be replaced with a more rugged device, such as a cold cathode discharge, a diamond emitter, or a β -emitting radiation source.

In conclusion, the effectiveness of QITMS for trace analysis of lightweight gas mixtures has been demonstrated. QITMS provides similar analytical performance, but at faster speeds compared to the best alternative mass analyzer technology evaluated. The size and ruggedness of QITMS will be addressed in the next generation prototype, which will be tested during real launch conditions. If successful, QITMS instrumentation will replace current leak detection systems, and improve the safety of Space Shuttle operations for years to come.

APPENDIX A CODE FOR MASS CALIBRATION

The following code was written in Microsoft Visual Basic, version 6 service pack 5, to perform mass calibration with user selected ions. The QITMS instrumentation used in this work were modified to operate over a mass range from approximately 2 to 50 Da, and could not use the standard per-florotributylamine calibration compound that produces ions outside of the mass range. The user picks up to five ions that the actual mass is known. Both the true mass and the apparent (uncalibrated) mass for each ion are entered into the software. (All 10 text boxes must be filled; if less than five ions are used, then values for an ion may be entered twice.) Pressing start will perform the linear fit, and the new slope and intercept will appear. These values will also be updated to the instrument, but will not be stored in the calibration file until the save button is pressed. The process may need to be repeated until an accurate calibration is achieved.

Microsoft Visual Basic 6 Code – MassCal.frm

Option Explicit

Private Sub cmdActualFC43_Click()

Dim i As Integer

txtActualMass(0) = CStr(68.9952)

txtActualMass(1) = CStr(130.992)

txtActualMass(2) = CStr(263.9871)

txtActualMass(3) = CStr(413.9775)

txtActualMass(4) = CStr(613.9647)

End Sub

Private Sub cmdActualAir_Click()

Dim i As Integer

```

txtActualMass(0) = CStr(14.003074)
txtActualMass(1) = CStr(18.010565)
txtActualMass(2) = CStr(28.006148)
txtActualMass(3) = CStr(31.98983)
txtActualMass(4) = CStr(39.962384)

```

End Sub

Private Sub cmdCalculate_Click()

```

Dim i As Integer, Count As Integer
Dim OldSlope As Double, OldIntercept As Double
Dim NewSlope As Double, NewIntercept As Double
Dim x(0 To 5) As Double, y(0 To 5) As Double

```

```

' If optMassCalibration(0).Value = True Then ' Normal scan
    OldSlope = GCQ.MassSlope
    OldIntercept = GCQ.MassIntercept
' Else ' AGC scan
    OldSlope = GCQ.AgcMassSlope
    OldIntercept = GCQ.AgcMassIntercept
' End If

```

```
Count = 0
```

```
For i = 0 To 4
```

```

    If txtObservedMass(i).Text <> CStr(0) And txtActualMass(i).Text <> vbNullString
Then

```

```

    x(Count) = CDBl(txtActualMass(i))
    y(Count) = OldSlope * CDBl(txtObservedMass(i)) + OldIntercept
    ' x1Plot 1, Count + 1, x(Count), y(Count)
    Count = Count + 1

```

```

Else
    Unload Me
    Exit Sub

```

```
End If
```

```
Next i
```

```
LinearFit x(), y(), Count, NewIntercept, NewSlope
```

```
' Display and plot new slope
```

```
lblMassSlope = CStr(Format(NewSlope, "0.0000"))
```

```
lblMassIntercept = CStr(Format(NewIntercept, "0.000"))
```

```
If chkShowGraph.Value = Checked Then
```

```
    InitializeGraph 2, "Mass Calibration", "Theoretical m/z", "RF DAC"
```

```
    For i = 0 To Count - 1
```

```
        x1Plot 2, i + 1, x(i), NewSlope * x(i) + NewIntercept
```

```
    Next i
```

```

End If

' Load new Slope Intercept values
GCQ.MassSlope = CDb1(lblMassSlope)
GCQ.MassIntercept = CDb1(lblMassIntercept)

End Sub

Private Sub cmdCloseManualCalibration_Click()

    Unload Me

End Sub

Private Sub cmdSave_Click()
    Dim CurrentTuneFile As String
    CurrentTuneFile = GetSetting("Custom Tune", "Tune Files", "Current Tune File",
"C:\GCQ\TUNE\AutoTune.tune")

    GCQ.SaveTuneFile (CurrentTuneFile) ' Save current tune file as outlined above
    GCQ.SaveCalibration &H8 ' Save Mass Calibration to INST.INI file

End Sub

Private Sub Form_Load()

    lblOldMassSlope = GCQ.MassSlope
    lblOldMassIntercept = GCQ.MassIntercept

End Sub

```

APPENDIX B CODE FOR REAL-TIME DATA PLOT

The following code was written in Microsoft Visual Basic, version 6 service pack 5, to display peak height data in a real-time plot against time. Up to eight ions can be monitored, with data refreshed at a user specified update rate. The data may also be saved to a Microsoft Excel spreadsheet for later processing. Display controls of the real-time plot are independent of data saved to Excel, and may be changed at any time.

Microsoft Visual Basic 6 Code – TableView.frm

```
Option Explicit
Dim x As Double
Dim XStep As Integer
Dim acq As Boolean

Private Sub cmdAcquireData_Click()
    If acq = False Then
        InitializeGraph txtNumIons, CStr(txtExcelTitle), "Seconds", "Ion Current
(arbitrary)"
        XStep = 0
        cmdFillTable.Enabled = True ' Was False to prevent stopping of excel acquisition
        cmdAcquireData.Caption = "STOP"
        acq = True
    Else
        acq = False
        cmdAcquireData.Caption = "Acquire"
        cmdFillTable.Enabled = True
    End If
End Sub

Private Sub cmdChartClear_Click()
    GCQGraph1.Clear
    x = 0
End Sub

Private Sub cmdFillTable_Click()
    If Timer1.Interval = (txtUpdateRate * 1000) Then
```

```

    Timer1.Interval = 0
    cmdFillTable.Caption = "GO"
    cmdAcquireData.Visible = False
Else
    Timer1.Interval = (txtUpdateRate * 1000)
    cmdFillTable.Caption = "STOP"
    cmdAcquireData.Visible = True
End If

End Sub

Private Sub cmdTableClose_Click()
    Unload Me
End Sub

Private Sub Form_Load()
    XStep = 0
    cmdAcquireData.Visible = False
End Sub

Private Sub Timer1_Timer()
    Dim i, j As Integer

    'Clear values within ioncount boxes
    For i = 0 To (txtNumIons - 1) 'Sets number of boxes to update
        txtIonCount(i) = CStr(0)
    Next i

    ' Setup graph
    GCQGraph1.Traces = txtNumIons 'Sets number of traces to plot in VB
    GCQGraph1.YMax = txtAxisValue(0)
    GCQGraph1.YMin = txtAxisValue(1)
    GCQGraph1.XMax = txtAxisValue(2)
    GCQGraph1.XMin = txtAxisValue(3)

    'Update the ioncount boxes and the graph with new data
    For i = 0 To (txtNumIons - 1) 'Sets number of data points to take
        If txtMassSlct(i) <> CStr(0) Then
            txtIonCount(i) = CStr(GCQ.Height(CDbl(txtMassSlct(i)) - 0.5,
            CDbl(txtMassSlct(i)) + 0.5))
            GCQGraph1.Plot CLng(i), x, CDbl(txtIonCount(i))
            If acq = True Then
                xlPlot i + 1, XStep + 1, XStep * txtUpdateRate, CDbl(txtIonCount(i))
            End If
        Else
            If acq = True Then

```

```
        xlPlot i + 1, XStep + 1, XStep * txtUpdateRate, CDBl(0)
    End If
End If
Next i

'Increment the X axis of the graph in seconds
x = x + txtUpdateRate
If acq = True Then
    XStep = XStep + 1
End If

End Sub
```

APPENDIX C CODE FOR POLARISQ AHGD SCAN

The following code was written in Microsoft Visual Basic, version 6 service pack 5, to control scan function parameters and display peak height data as a plot versus time, all in real time. The software first sets up a two mass range segmented scan function, which can be changed as needed for optimization. Up to eight ions can be monitored, with data refreshed at a user specified update rate. The data may also be saved to a Microsoft Excel spreadsheet later processing. The spreadsheet title is entered before acquisition, and the data must be saved after acquisition is ended. Display controls of the real-time plot are independent of data saved to Excel, and may be changed at any time.

Microsoft Visual Basic 6 Code – AHGDScan.frm

```
Option Explicit
Dim NumSeg, NumTraces As Long
Dim x, ScanRate, BackSteps, IonTime, PostIonTime, N2EjectTime As Double
Dim MultOnTime, PrePostTime, UpdateRate, qej, ResEjV, OldSamp, OldBand As Double
Dim DaValue(0 To 7) As Double
Dim InjRfDac(0 To 1) As Double
Dim Acquire, AutoResEj As Boolean
Dim t As Integer

Private Sub cmdAcquire_Click()
    Dim i As Integer

    If Acquire = False Then
        InitializeSheet
        t = 1
        xlPoint t, 1, "Time (s)"
        For i = 2 To (NumTraces + 1)
            xlPoint t, i, DaValue(i - 2)
        Next i
        t = 2
    End If
End Sub
```



```

    cmdAcquire.Caption = "STOP"
    Acquire = True
Else
    Acquire = False
    cmdAcquire.Caption = "Acquire"
End If

```

```
End Sub
```

```
Private Sub cmdClearPlot_Click()
```

```

    TrendPlot.Clear
    x = 0#
    TrendPlot.XMax = 0#

```

```
End Sub
```

```
Private Sub cmdUpdatePlot_Click()
```

```

    Update_Plot

```

```
End Sub
```

```
Private Sub Update_Plot()
```

```

    Dim i As Integer

```

```

'Update axis value of trend plot
TrendPlot.YMax = CDbI(txtAxisValue(0))
TrendPlot.YMin = CDbI(txtAxisValue(1))
TrendPlot.XMax = CDbI(txtAxisValue(2))
TrendPlot.XMin = CDbI(txtAxisValue(3))

```

```

'Count Number of m/z value to plot
NumTraces = 0@
For i = 0 To 7 ' Max number of m/z values
    If txtDaValue(i) <> vbNullString Then
        DaValue(i) = CDbI(txtDaValue(i))
        NumTraces = NumTraces + 1@
    End If
Next i
TrendPlot.Traces = NumTraces

```

```
End Sub
```

```
Private Sub Form_Load()
```

```

    ' Initialize buttons

```

```

tmrScan.Enabled = False
cmdScanStart.Enabled = True
cmdScanStart.Caption = "Start"
cmdScanApply.Enabled = True
cmdScanClose.Enabled = True
cmdAcquire.Enabled = False

```

```

' Stop instrument from scanning
GCQ.AutoScan = False

```

```

' Setup default parameters in text fields
txtFirstMass(0).Text = "0"
txtLastMass(0).Text = "5"
txtFirstMass(1).Text = "28"
txtLastMass(1).Text = "42"
txtqe.Text = "0.901643"
chkAutoResEj = False

```

```

' Backup running values
OldSamp = GCQ.Samp
OldBand = GCQ.Band

```

```

' Set number of scan ranges to examine, default 2
NumSeg = 2@
x = 0#

```

End Sub

Private Sub cmdScanStart_Click()

```

If Not tmrScan.Enabled Then ' Start scanning
    cmdScanClose.Enabled = False
    cmdScanStart.Caption = "Stop"
    cmdAcquire.Enabled = True
    Set_Mode ' Set user parameters
    Update_Plot ' Set parameters for trend plot
    tmrScan.Enabled = True ' Start scan timer to periodically take a scan

```

```

Else ' Stop scanning
    tmrScan.Enabled = False
    cmdScanClose.Enabled = True
    cmdScanStart.Caption = "Start"
    cmdAcquire.Enabled = False
End If

```

End Sub

```
Private Sub tmrScan_Timer()
```

```
    tmrScan.Enabled = False ' Disable timer while scan being taken
```

```
    ' Take a scan
```

```
    GCQ.ClearMatrix ' Clear the current scan from memory
```

```
    MatrixAHGDScan ' Load values for various devices
```

```
    GCQ.LoadMatrix 0 ' Load the scan matrix into the instrument
```

```
    GCQ.Go 0 ' Take a single scan (includes microscans) and record the mass spectrum
```

```
    UpdateGraph ' Send new data to TrendPlot
```

```
    tmrScan.Enabled = True ' Restart timer for next scan
```

```
End Sub
```

```
Private Sub UpdateGraph()
```

```
    Dim i As Integer
```

```
    Dim y As Double
```

```
    ' Loop to Update Data to each trace on trend plot
```

```
    For i = 0 To (CInt(NumTraces) - 1)
```

```
        y = GCQ.Height((DaValue(i) - 0.5), (DaValue(i) + 0.5))
```

```
        TrendPlot.Plot CLng(i), x, y
```

```
        If Acquire = True Then
```

```
            xlPoint t, (i + 2), y
```

```
        End If
```

```
    Next i
```

```
    If Acquire = True Then
```

```
        xlPoint t, 1, ((t - 1) * UpdateRate)
```

```
        t = t + 1
```

```
    End If
```

```
    x = x + 1
```

```
End Sub
```

```
Private Sub cmdScanApply_Click()
```

```
    Set_Mode
```

```
End Sub
```

```
Private Sub Set_Mode()
```

```
    Dim j, k As Long
```

```
    Dim ScanTime As Double
```

```
    Dim MicroScans As Integer
```

```

' Set user parameters
GCQ.Mode = 0
GCQ.NumSeg = NumSeg
For j = 0 To NumSeg - 1
    GCQ.SegFirstMass(j) = CLng(txtFirstMass(j))
    GCQ.SegLastMass(j) = CLng(txtLastMass(j))
    GCQ.SegScale(j) = 1@
Next j
qej = CDbI(txtqej)
GCQ.Mode = 4
InjRfDac(0) = CDbI(txtIonRF(0))
InjRfDac(1) = CDbI(txtIonRF(1))
ScanRate = CDbI(txtScanRate)
BackSteps = CDbI(txtBackSteps)
IonTime = CDbI(txtIonTime)
PostIonTime = CDbI(txtPostIonTime)
N2EjectTime = CDbI(txtEjectTime)
MultOnTime = CDbI(txtMultOnTime)
PrePostTime = CDbI(txtPrePostTime)
UpdateRate = CDbI(txtUpdateRate)
AutoResEj = chkAutoResEj
ResEjV = CDbI(txtResEjV)

' Determine number of microscans
ScanTime = 2 * ((2 * PrePostTime) + IonTime + PostIonTime + N2EjectTime +
MultOnTime + (BackSteps * ScanRate))
For k = 0 To NumSeg - 1
    ScanTime = ScanTime + ((CDbI(GCQ.SegLastMass(k)) -
CDbI(GCQ.SegFirstMass(k))) * ScanRate)
Next k
MicroScans = CInt(((UpdateRate * 1000#) - 130) / Int(ScanTime))
GCQ.MicroScans = CLng(MicroScans)
tmrScan.Interval = 1 * ((UpdateRate * 1000) - ((MicroScans * ScanTime) + 130))

'Adjust Acquisition parameters based on the Scan Rate value
GCQ.Samp = (ScanRate * 100)
GCQ.Band = ((-62500) * ScanRate) + 18750 ' Based on a band of 7500 Hz at 0.18
ms/Da and 15000 Hz at 0.06 ms/Da

' Calculate waveforms
'CalcWvfrmCustomFullScan

End Sub

Private Sub cmdScanClose_Click()

```

```
' Return to normal instrument scanning
FullScan 10, 42
GCQ.Samp = OldSamp
GCQ.Band = OldBand
GCQ.AutoScan = True
Unload Me
```

End Sub

Private Sub MatrixAHGDScan()

' Loads scan matrix with device values for each scan table

Dim j, k As Integer

GCQ.SyncMaster gcqlib.Devices.RfDac ' Set RFDAC as master device

' Calculate resonant ejection frequency

Dim ResEjFreq As Double

ResEjFreq = GCQ.qtofreq(qej)

j = 0 ' Interval of matrix events

For k = 0 To (CInt(NumSeg) - 1) ' Interval for k number of scan segments

' Preiontime

GCQ.Matrix(gcqlib.Devices.RfDac, j, 2) = PrePostTime ' Length of scan table

GCQ.Matrix(gcqlib.Devices.RfDac, j, 0) = InjRfDac(k)

GCQ.Matrix(gcqlib.Devices.AuxFreq, j, 0) = ResEjFreq

GCQ.Matrix(gcqlib.Devices.AUXAMP, j, 0) = 0

GCQ.Matrix(gcqlib.Devices.GATELENS, j, 0) = GCQ.GateLensOff

GCQ.Matrix(gcqlib.Devices.ELECLENS, j, 0) = GCQ.ElecLensOn

GCQ.Matrix(gcqlib.Devices.EE, j, 0) = GCQ.ElecEnergyOn

GCQ.Matrix(gcqlib.Devices.Dout2, j, 0) = GCQ.Dout2

GCQ.Matrix(gcqlib.Devices.ACQU, j, 0) = 0

j = j + 1

' First ion injection step

GCQ.Matrix(gcqlib.Devices.RfDac, j, 2) = IonTime ' Length of scan table

GCQ.Matrix(gcqlib.Devices.RfDac, j, 5) = 0

GCQ.Matrix(gcqlib.Devices.RfDac, j, 0) = InjRfDac(k)

GCQ.Matrix(gcqlib.Devices.AuxFreq, j, 0) = ResEjFreq

GCQ.Matrix(gcqlib.Devices.AUXAMP, j, 0) = 0

GCQ.Matrix(gcqlib.Devices.GATELENS, j, 0) = GCQ.GateLensOn ' Gate on value

GCQ.Matrix(gcqlib.Devices.GATELENS, j, 1) = GCQ.GateLensOff ' Gate off

value

GCQ.Matrix(gcqlib.Devices.GATELENS, j, 3) = IonTime ' Time to keep gate open, not used if AGC on

GCQ.Matrix(gcqlib.Devices.ELECLENS, j, 0) = GCQ.ElecLensOn

GCQ.Matrix(gcqlib.Devices.EE, j, 0) = GCQ.ElecEnergyOn

GCQ.Matrix(gcqlib.Devices.Dout2, j, 0) = GCQ.Dout2

GCQ.Matrix(gcqlib.Devices.ACQU, j, 0) = 0

j = j + 1

' Postiontime

GCQ.Matrix(gcqlib.Devices.RfDac, j, 2) = PostIonTime ' Length of scan table

GCQ.Matrix(gcqlib.Devices.RfDac, j, 0) = InjRfDac(k)

GCQ.Matrix(gcqlib.Devices.AuxFreq, j, 0) = ResEjFreq

GCQ.Matrix(gcqlib.Devices.AUXAMP, j, 0) = 0

GCQ.Matrix(gcqlib.Devices.GATELENS, j, 0) = GCQ.GateLensOff

GCQ.Matrix(gcqlib.Devices.ELECLENS, j, 0) = GCQ.ElecLensOn

GCQ.Matrix(gcqlib.Devices.EE, j, 0) = GCQ.ElecEnergyOn

GCQ.Matrix(gcqlib.Devices.Dout2, j, 0) = GCQ.Dout2

GCQ.Matrix(gcqlib.Devices.ACQU, j, 0) = 0

j = j + 1

' Ramp to starting mass

GCQ.Matrix(gcqlib.Devices.RfDac, j, 2) = N2EjectTime ' Length of scan table

GCQ.Matrix(gcqlib.Devices.RfDac, j, 0) = InjRfDac(k)

GCQ.Matrix(gcqlib.Devices.RfDac, j, 1) =

GCQ.MassToDac(CDb1(GCQ.SegFirstMass(k)) - BackSteps)

GCQ.Matrix(gcqlib.Devices.AuxFreq, j, 0) = ResEjFreq

GCQ.Matrix(gcqlib.Devices.AUXAMP, j, 0) = 0

GCQ.Matrix(gcqlib.Devices.GATELENS, j, 0) = GCQ.GateLensOff

GCQ.Matrix(gcqlib.Devices.ELECLENS, j, 0) = GCQ.ElecLensOn

GCQ.Matrix(gcqlib.Devices.EE, j, 0) = GCQ.ElecEnergyOn

GCQ.Matrix(gcqlib.Devices.Dout2, j, 0) = GCQ.Dout2

GCQ.Matrix(gcqlib.Devices.ACQU, j, 0) = 0

j = j + 1

' Turn on multiplier

GCQ.Matrix(gcqlib.Devices.RfDac, j, 2) = MultOnTime ' Length of scan table

GCQ.Matrix(gcqlib.Devices.RfDac, j, 0) =

GCQ.MassToDac(CDb1(GCQ.SegFirstMass(k)) - BackSteps)

GCQ.Matrix(gcqlib.Devices.AuxFreq, j, 0) = ResEjFreq

If AutoResEj = True Then

GCQ.Matrix(gcqlib.Devices.AUXAMP, j, 0) =

GCQ.MassToResEjectionAmp(CDb1(GCQ.SegFirstMass(k)) - BackSteps)

Else

GCQ.Matrix(gcqlib.Devices.AUXAMP, j, 0) = ResEjV

End If

GCQ.Matrix(gcqlib.Devices.GATELENS, j, 0) = GCQ.GateLensOff

```

GCQ.Matrix(gcqlib.Devices.ELECLENS, j, 0) = GCQ.ElecLensOn
GCQ.Matrix(gcqlib.Devices.ELECLENS, j, 1) = GCQ.ElecLensOff
GCQ.Matrix(gcqlib.Devices.EE, j, 0) = GCQ.ElecEnergyOn
GCQ.Matrix(gcqlib.Devices.EE, j, 1) = GCQ.ElecEnergyOff
GCQ.Matrix(gcqlib.Devices.Dout2, j, 0) = GCQ.Dout2 Or
gcqlib.DOUT2_Bits.multonbit ' Turn on multiplier
GCQ.Matrix(gcqlib.Devices.ACQU, j, 0) = 0
j = j + 1

' Ramp to firstmass
GCQ.Matrix(gcqlib.Devices.RfDac, j, 2) = (BackSteps * ScanRate) ' Length of scan
table
GCQ.Matrix(gcqlib.Devices.RfDac, j, 0) =
GCQ.MassToDac(CDb1(GCQ.SegFirstMass(k)) - BackSteps)
GCQ.Matrix(gcqlib.Devices.RfDac, j, 1) =
GCQ.MassToDac(CDb1(GCQ.SegFirstMass(k)))
GCQ.Matrix(gcqlib.Devices.AuxFreq, j, 0) = ResEjFreq
If AutoResEj = True Then
GCQ.Matrix(gcqlib.Devices.AUXAMP, j, 0) =
GCQ.MassToResEjectionAmp(CDb1(GCQ.SegFirstMass(k)) - BackSteps)
GCQ.Matrix(gcqlib.Devices.AUXAMP, j, 1) =
GCQ.MassToResEjectionAmp(CDb1(GCQ.SegFirstMass(k)))
Else
GCQ.Matrix(gcqlib.Devices.AUXAMP, j, 0) = ResEjV
End If
GCQ.Matrix(gcqlib.Devices.GATELENS, j, 0) = GCQ.GateLensOff
GCQ.Matrix(gcqlib.Devices.ELECLENS, j, 0) = GCQ.ElecLensOff
GCQ.Matrix(gcqlib.Devices.EE, j, 0) = GCQ.ElecEnergyOff
GCQ.Matrix(gcqlib.Devices.Dout2, j, 0) = GCQ.Dout2 Or
gcqlib.DOUT2_Bits.multonbit ' Turn on multiplier
GCQ.Matrix(gcqlib.Devices.ACQU, j, 0) = 0
j = j + 1

' Mass scan
GCQ.Matrix(gcqlib.Devices.RfDac, j, 2) = ((CDb1(GCQ.SegLastMass(k)) -
CDb1(GCQ.SegFirstMass(k))) * ScanRate) ' Length of scan table
GCQ.Matrix(gcqlib.Devices.RfDac, j, 0) =
GCQ.MassToDac(CDb1(GCQ.SegFirstMass(k)))
GCQ.Matrix(gcqlib.Devices.RfDac, j, 1) =
GCQ.MassToDac(CDb1(GCQ.SegLastMass(k)))
GCQ.Matrix(gcqlib.Devices.AuxFreq, j, 0) = ResEjFreq
If AutoResEj = True Then
GCQ.Matrix(gcqlib.Devices.AUXAMP, j, 0) =
GCQ.MassToResEjectionAmp(CDb1(GCQ.SegFirstMass(k)))
GCQ.Matrix(gcqlib.Devices.AUXAMP, j, 1) =
GCQ.MassToResEjectionAmp(CDb1(GCQ.SegLastMass(k)))

```

```

Else
  GCQ.Matrix(gcqlib.Devices.AUXAMP, j, 0) = ResEjV
End If
GCQ.Matrix(gcqlib.Devices.GATELENS, j, 0) = GCQ.GateLensOff
GCQ.Matrix(gcqlib.Devices.ELECLENS, j, 0) = GCQ.ElecLensOff
GCQ.Matrix(gcqlib.Devices.EE, j, 0) = GCQ.ElecEnergyOff
GCQ.Matrix(gcqlib.Devices.Dout2, j, 0) = GCQ.Dout2 Or
gcqlib.DOUT2_Bits.multonbit ' Turn on multiplier
GCQ.Matrix(gcqlib.Devices.ACQU, j, 0) = CDb1(GCQ.SegFirstMass(k))
GCQ.Matrix(gcqlib.Devices.ACQU, j, 1) = CDb1(GCQ.SegLastMass(k))
GCQ.Matrix(gcqlib.Devices.ACQU, j, 5) = 4 ' Normal acquisition
j = j + 1

' Postscantime
GCQ.Matrix(gcqlib.Devices.RfDac, j, 2) = PrePostTime ' Length of scan table
GCQ.Matrix(gcqlib.Devices.RfDac, j, 0) = 0
GCQ.Matrix(gcqlib.Devices.AuxFreq, j, 0) = ResEjFreq
GCQ.Matrix(gcqlib.Devices.AUXAMP, j, 0) = 0
GCQ.Matrix(gcqlib.Devices.GATELENS, j, 0) = GCQ.GateLensOff
GCQ.Matrix(gcqlib.Devices.ELECLENS, j, 0) = GCQ.ElecLensOff
GCQ.Matrix(gcqlib.Devices.ELECLENS, j, 1) = GCQ.ElecLensOn
GCQ.Matrix(gcqlib.Devices.EE, j, 0) = GCQ.ElecEnergyOff
GCQ.Matrix(gcqlib.Devices.EE, j, 1) = GCQ.ElecEnergyOn
GCQ.Matrix(gcqlib.Devices.Dout2, j, 0) = GCQ.Dout2 ' Turn off multiplier
GCQ.Matrix(gcqlib.Devices.ACQU, j, 0) = 0
j = j + 1

Next k

End Sub

Private Sub CalcWvfrmCustomFullScan()
' Calculate waveforms

' No waveforms to calculate

End Sub

```


APPENDIX D

CODE FOR AHGD OPTIMIZED UF-IT SCAN MATRIX

The following code was written in Microsoft Visual C++ to program an AHGD application optimized scan matrix for the UF-IT. Each section sets the behavior of a different QITMS parameter, and is comprised of ten events performed in series to form the complete scan function. All sections are synchronized to the timing of the RF DAC. The scan matrix was repeated for the two scan segments, and was used with the following variable assignments:

```
lowrfdac = 1900 (the equivalent of 90 Vp)
highrfdac = 3200 (the equivalent of 335 Vp)
eeon = eeff = -97 V
fmseg1 = 1 Da
lmseg1 = 5 Da
fmseg2 = 30 Da
lmseg2 = 42 Da
backsteps = 7.3 Da
Preiontime = 0.25 ms
Iontime = 5 ms
Postiontime = 0.3 ms
Multitime = 0.4 ms
Scanrate = 0.06 ms/Da
Postscantime = 0.25 ms
Gatelensoff = -130 V
Gatelenon = +130 V
```

Microsoft Visual C++ Code – MassCal.frm

```
for (segcounter = 0; segcounter < 2; segcounter++){

// Specify IonRf Dac value for segment.
if (segcounter < 1) {
ionrfdac = lowrfdac;
eevalue = eeon;
fm = fmseg1;
lm = lmseg1;
```

```

    }
else {
ionrfdac = highrfdac;
eevalue = eeff;
fm = fmseg2;
lm = lmseg2;
}

/***** RFDAC Value *****/

int j = initcount;

// Event 0 -- Pre-ion time
MATRIX(RFDAC,j,0, ionrfdac);
MATRIX(RFDAC,j,2, preiontime);
j ++;

// Event 1 -- Ionization RF
MATRIX(RFDAC,j,0, ionrfdac);
MATRIX(RFDAC,j,2, iontime);
MATRIX(RFDAC,j,5, 0);
j ++;

// Event 2 -- Post-ionization time
MATRIX(RFDAC,j,0, ionrfdac);
MATRIX(RFDAC,j,2, 0);
j ++;

// Event 3 -- Backstep ramp
MATRIX(RFDAC,j,0, ionrfdac);
MATRIX(RFDAC,j,1, mtod(fm - backsteps));
MATRIX(RFDAC,j,2, postiontime);
j ++;

// Event 4 -- Cool time
MATRIX(RFDAC,j,0, mtod(fm - backsteps));
MATRIX(RFDAC,j,2, multitime);
j ++;

// Event 5 -- Pre-Scan out
MATRIX(RFDAC,j,0, mtod(fm - backsteps));
MATRIX(RFDAC,j,1, mtod(fm));
MATRIX(RFDAC,j,2, backsteps * scanrate);
j ++;

// Event 6 -- Scan out

```

```

MATRIX(RFDAC,j,0, mtod(fm));
MATRIX(RFDAC,j,1, mtod(lm));
MATRIX(RFDAC,j,2, (lm - fm) * scanrate);
j ++;

// Event 7 -- Post Scan (RF off)
MATRIX(RFDAC,j,0, 0);
MATRIX(RFDAC,j,2, postscantime);

/***** Gate lens Potential *****/

j = initcount;

// Event 0 -- Pre-ion time
MATRIX(GATELENS,j,0, gatelensoff);
j ++;

// Event 1 -- Ionization RF
MATRIX(GATELENS,j,0, gatelenson);
j ++;

// Event 2 -- Post-ionization time
MATRIX(GATELENS,j,0, gatelensoff);
j ++;

// Event 3 -- Backstep ramp
MATRIX(GATELENS,j,0, gatelensoff);
j ++;

// Event 4 -- Cool time
MATRIX(GATELENS,j,0, gatelensoff);
j ++;

// Event 5 -- Pre-Scan out
MATRIX(GATELENS,j,0, gatelensoff);
j ++;

// Event 6 -- Scan out
MATRIX(GATELENS,j,0, gatelensoff);
j ++;

// Event 7 -- Post Scan (RF off)
MATRIX(GATELENS,j,0, gatelensoff);

/***** Electron Energy *****/

```

```

j = initcount;

// Event 0 -- Pre-ion time
MATRIX(EEj,0, eevalue);
j ++;

// Event 1 -- Ionization RF
MATRIX(EEj,0, eevalue);
j ++;

// Event 2 -- Post-ionization time
MATRIX(EEj,0, eevalue);
j ++;

// Event 3 -- Backstep ramp
MATRIX(EEj,0, eevalue);
j ++;

// Event 4 -- Cool time
MATRIX(EEj,0, eevalue);
j ++;

// Event 5 -- Pre-Scan out
MATRIX(EEj,0, eevalue);
j ++;

// Event 6 -- Scan out
MATRIX(EEj,0, eevalue);
j ++;

// Event 7 -- Post Scan (RF off)
MATRIX(EEj,0, eevalue);

/***** Trigger for Electron Multiplier *****/

j = initcount;

// Event 0 -- Pre-ion time
MATRIX(DOUT2j,0, dout2);
j ++;

// Event 1 -- Ionization RF
MATRIX(DOUT2j,0, dout2);
j ++;

// Event 2 -- Post-ionization time

```

```

MATRIX(DOUT2,j,0, dout2 );
j ++;

// Event 3 -- Backstep ramp
MATRIX(DOUT2,j,0, dout2 );
j ++;

// Event 4 -- Cool time
MATRIX(DOUT2,j,0, dout2 | multonbit); // Multiplier turned on
j ++;

// Event 5 -- Pre-Scan out
MATRIX(DOUT2,j,0, dout2 | multonbit); // Multiplier turned on
j ++;

// Event 6 -- Scan out
MATRIX(DOUT2,j,0, dout2 | multonbit); // Multiplier turned on
j ++;

// Event 7 -- Post Scan (RF off)
MATRIX(DOUT2,j,0, dout2);

/***** Trigger for Acquisition Device *****/

j = initcount;

// Event 0 -- Pre-ion time
MATRIX(ACQU,j,0, 0);
j ++;

// Event 1 -- Ionization RF
MATRIX(ACQU,j,0, 0);
j ++;

// Event 2 -- Post-ionization time
MATRIX(ACQU,j,0, 0);
j ++;

// Event 3 -- Backstep ramp
MATRIX(ACQU,j,0, 0);
j ++;

// Event 4 -- Cool time
MATRIX(ACQU,j,0, 0);
j ++;

```

```
// Event 5 -- Pre-Scan out
MATRIX(ACQUj,0, 0);
j ++;

// Event 6 -- Scan out
MATRIX(ACQUj,0, fm); // Acquisition started
MATRIX(ACQUj,1, lm); // Acquisition ended
MATRIX(ACQUj,5, A_NORM);
j ++;

// Event 7 -- Post Scan (RF off)
MATRIX(ACQUj,0, 0);
j ++;

initcount = j;
}
```

APPENDIX E
LIST OF ACRONYMS AND ABBREVIATIONS

ADC:	Analogue-to-digital converter
ADO:	Average dipole orientation theory
AHGD:	Advanced Hazardous Gas Detection Project
APCI:	Atmospheric pressure chemical ionization
BG:	Background gas
CI:	Chemical ionization
Da:	Daltons
DAC:	Digital-to-analogue converter
DC:	Direct current
EI:	Electron impact ionization
ESI:	Electrospray ionization
ET:	External tank (of the Space Shuttle)
FT-ICRMS:	Fourier transform ion cyclotron resonance mass spectrometry
FWHM:	Full-width half-maximum
GB:	Gas-phase basicity
GC:	Gas chromatography
GDS:	Gas dilution system
HGDS:	Hazardous Gas Detection System
IE:	Ionization energy
i.d.:	Inner diameter

LPF:	Low-pass filter
m/z:	Mass-to-charge ratio
MALDI:	Matrix assisted laser desorption ionization
MFC:	Mass flow controller
MLP:	Mobile launch platform
MS ⁿ :	Multiple-stage mass spectrometry
NASA:	National Aeronautics and Space Administration
o.d.:	Outer diameter
PA:	Proton affinity
ppm:	Part-per-million
QIT:	Quadrupole ion trap
QITMS:	Quadrupole ion trap mass spectrometer (or spectrometry)
Quad:	Linear quadrupole
QuadArray:	Quadrupole array
RE:	Recombination energy
RF:	Radio frequency
RGA:	Residual gas analyzer
S/N:	Signal-to-noise ratio
sccm:	Standard cubic centimeters per minute
SG:	Span gas (gas standard)
SGS:	Smoothed general solution
SIM:	Selective ion monitoring
SRB:	Solid rocket booster (of the Space Shuttle)

SRM:	Selective reaction monitoring
SRS:	Stanford Research Systems
SSME:	Space Shuttle main engine
TIC:	Total ion current
TG:	Test gas (gas standard)
TOF:	Time-of-flight
UF-IT:	University of Florida Ion Trap (customized QITMS)
XDK:	Xcalibur Development Kit
ZG:	Zero gas (gas standard)

LIST OF REFERENCES

1. Paul, W.; Steinwedel, H. *German Patent* 1956, DE944900.
2. Peng, Y.; Plass, W. R.; Cooks, R. G. *J. Am. Soc. Mass Spectrom.* **2002**, 13, 623-629.
3. Brodbelt, J. S.; Glish, G. L. *J. Am. Soc. Mass Spectrom.* **2002**, 13, 587-588.
4. Stafford, G., Jr. *J. Am. Soc. Mass Spectrom.* **2002**, 13, 589-596.
5. Todd, J. F. J.; Penman, A. D. *Int. J. Mass Spectrom. Ion Processes* **1991**, 106, 1-20.
6. Glish, G. L.; McLuckey, S. A. *Int. J. Mass Spectrom. Ion Processes* **1991**, 106, vii-viii.
7. March, R. E.; Hughes, R. J.; Todd, J. F. *Quadrupole Storage Mass Spectrometry*; Wiley-Interscience: New York, NY, 1989.
8. Stafford, G. C., Jr.; Kelley, P. E.; Syka, J. E. P.; Reynolds, W. E.; Todd, J. F. *J. Int. J. Mass Spectrom. Ion Processes* **1984**, 60, 85-98.
9. Stafford, G. C.; Kelley, P. E.; Stephens, D. R. *U.S. Patent* 1985, 4,540,884.
10. Paul, W.; Steinwedel, H. *U.S. Patent* 1960, 2939952.
11. Fenn, J. B. *Int. J. Mass Spectrom.* **2000**, 200, 459-478.
12. Ghosh, P. K. *Ion Traps*; Oxford University: New York, 1995.
13. March, R. E. in *Encyclopedia of Analytical Chemistry*; Meyers, R. A., Ed.; John Wiley & Sons: Chichester, UK, 2000; Vol 13, pp. 11848-11872.
14. March, R. E.; Londry, F. A. Chapter 2 in *Practical Aspects of Ion Trap Mass Spectrometry*; March, R. E., Todd, J. F. J., Eds.; CRC Press: Boca Raton, FL, 1995; Vol 1, pp. 25-48.
15. Louris, J. N.; Cooks, R. G.; Syka, J. E. P.; Kelley, P. E.; Stafford, G. C., Jr.; Todd, J. F. *J. Anal. Chem.* **1987**, 59, 1677-1685.
16. Mathieu, E. *J. Math. Pure Appl.* **1868**, 13, 137.
17. Knight, R. D. *Int. J. Mass Spectrom. Ion Phys.* **1983**, 51, 127-131.

18. Syka, J. E. P. Chapter 4 in *Practical Aspects of Ion Trap Mass Spectrometry*; March, R. E., Todd, J. F. J., Eds.; CRC Press: Boca Raton, FL, 1995; Vol 1, pp. 169-205.
19. Ince, E. Researches into the Characteristic Numbers of the Mathieu Equation. *Proceedings of the Royal Society of Edinburgh*; Neiland Co. Ltd.: Edinburgh, 1925-1926; XLVI, 20-29.
20. McLachlan, N. W. *Theory and Applications of Mathieu Functions*; Clarendon: Oxford, 1947.
21. Forbes, M. W.; Sharifi, M.; Croley, T.; Lausevic, Z.; March, R. E. *J. Mass Spectrom.* **1999**, 34, 1219-1239.
22. Dehmelt, H. G. Chapter 2 in *Advances in Atomic and Molecular Physics*; Bates, D. R., Ed.; Academic Press: New York, NY, 1967; Vol 3, pp. 53-72.
23. Major, F. G.; Dehmelt, H. G. *Phys. Rev.* **1968**, 170, 91-107.
24. Todd, J. F. J.; Lawson, G. Chapter 8 in *Quadrupole Mass Spectrometry and Its Applications*; Dawson, P. H., Ed.; Elsevier Scientific: Amsterdam, 1976; pp. 181-224.
25. Todd, J. F. J.; Waldren, R. M.; Mather, R. E. *Int. J. Mass Spectrom. Ion Phys.* **1980**, 34, 325-349.
26. Kononkov, N. V.; Sudakov, M.; Douglas, D. J. *J. Am. Soc. Mass Spectrom.* **2002**, 13, 597-613.
27. Dawson, P. H. Chapter 2 in *Quadrupole Mass Spectrometry and Its Applications*; Dawson, P. H., Ed.; Elsevier Scientific: Amsterdam, 1976; pp. 9-64.
28. Todd, J. F. J.; March, R. E. *Int. J. Mass Spectrom.* **1999**, 190/191, 9-35.
29. Fischer, E. Z. *Phys.* **1959**, 156, 1-26.
30. Rettinghaus, V. G. Z. *Angew. Phys.* **1967**, 22, 321-326.
31. Syka, J. E. P.; Fies, W. J., Jr. *US Patent*, 1988, 4755670.
32. Dawson, P. H.; Whetten, N. R. *J. Vac. Sci. Technol.* **1968**, 5, 1-10.
33. Dawson, P. H.; Whetten, N. R. *J. Vac. Sci. Technol.* **1968**, 5, 11-18.
34. G. Lawson, J. F. J. Todd, British Mass Spectroscopy Group Meeting, Bristol, **1971**, Abstract No. 44.
35. Bonner, R. F.; Lawson, G.; Todd, J. F. J. *Int. J. Mass Spectrom. Ion Phys.* **1972/73**, 10, 197-203.

36. March, R. E.; Hughes, R. J.; Todd, J. F. J. Chapter 4 in *Quadrupole Storage Mass Spectrometry*; Wiley Interscience: New York, 1989; pp. 209-270.
37. Baldeschweiler, J. D. *Science* **1968**, 159, 263-273.
38. McIver, R. T., Jr. *Rev. Sci. Instrum.* **1970**, 41, 555-558.
39. Comisarow, M. B.; Marshall, A. G. *Chem. Phys. Lett.* **1974**, 25, 282-283.
40. Brodbelt, J. S. Chapter 5 in *Practical Aspects of Ion Trap Mass Spectrometry*; March, R. E., Todd, J. F. J., Eds.; CRC Press: Boca Raton, FL, 1995; Vol 1, pp. 209-220.
41. Louris, J. N.; Amy, J. W.; Ridley, T. Y.; Cooks, R. G. *Int. J. Mass Spectrom. Ion Processes* **1989**, 88, 97-111.
42. Steiner, V.; Beaugrand, C.; Liere, P.; Tabet, J. C. *J. Mass Spectrom.* **1999**, 34, 511-520.
43. Ziegler, Z. *Anal. Chem.* **2002**, 74, 489A-492A.
44. Information Summaries. *Countdown! NASA Launch Vehicles and Facilities*; IS-1997-10-03-KSC, NASA, Kennedy Space Center, FL, **1997**; pp. 1,5.
45. Information Summaries. *Space Shuttle*; PMS 013-B (KSC), NASA, Kennedy Space Center, FL, **1995**.
46. Naylor, G. R.; Hritz, R.; Greenfield, T.; Lampkin, C.; Lorenzo-Luaces, F.; Lingvay, L.; Floyd, D.; Adams, F.; Breznik, G.; Davis, B.; Schwalb, A.; Curley, C.; McKinney, G. *Nasa Tech Briefs*, May 2001, KSC1210906.
47. Helms, W. R.; Starr, S. O. Advanced Development of Ground Instrumentation as a Key Strategy in Improving the Safety and Efficiency of Space Shuttle Checkout and Launch. *The 33rd Space Congress*, Cocoa Beach, FL, **1996**.
48. Adams, F. W.; Griffin, T. P. Advanced Hazardous Gas Detection Miniature Mass Spectrometer, *KSC/JPL Joint Concept Paper/White Paper*, Kennedy Space Center, FL, **2000**.
49. Dumoulin, J. *STS-93 (95)*, 1999, NASA: Kennedy Space Center, FL, <http://science.ksc.nasa.gov/shuttle/missions/sts-93/mission-sts-93.html>, accessed January 2003.
50. Humphries, K. *STS-93: Nozzle Collant Tube Leak Photos*, 1999, PSINet: Kennedy Space Center, FL, <http://spaceflight.nasa.gov/Shuttle/archives/sts-93/leak.html>, accessed January, 2003.

51. Griffin, T. P.; Breznik, G. S.; Mizell, C. A.; Helms, W. R.; Naylor, G. R.; Haskell, W. D. *Trends in Anal. Chem.* **2002**, 21, 488-497.
52. Badman, E. R.; Cooks, R. G. *J. Mass Spectrom.* **2000**, 35, 659-671.
53. *Performance, Design, Fabrication, and Certification of the Space Shuttle Hazardous Gas Detection System (U72-1186), Specification For*; Helms, W. R., Ed.; Kennedy Space Center, FL, 1977; 79K07981.
54. Griffin, T.; Young, D. *Requirements for Performance, Design, Fabrication and Certification of HGDS 2000*; Diorio, K.; Fish, T.; Breznik, G.; Mizell, C., Eds.; Kennedy Space Center, FL, 2000; KSC-DL-3376.
55. Griffin, T. P. *Advanced Hazardous Gas Detection System Requirements Document*; Diorio, K. A.; Adams, F. W.; Breznik, G. S.; Helms, W. R., Eds.; Kennedy Space Center, FL, 2000; KSC-MM-4864.
56. Taylor, S.; Tunstall, J. J.; Leck, J. H.; Tindall, R. F.; Jullien, J. P.; Batey, J.; Syms, R. R. A.; Tate, T.; Ahmad, M. M. *Vacuum* **1999**, 53, 203-206.
57. Holkeboer, D. H.; Karandy, T. L.; Currier, F. C.; Frees, L. C.; Ellefson, R. E. *J. Vac. Sci. Technol. A* **1998**, 16, 1157-1162.
58. Freidhoff, C. B.; Young, R. M.; Sriram, S.; Braggins, T. T.; O'Keefe, T. W.; Adam, J. D.; Nathanson, H. C.; Syms, R. R. A.; Tate, T. J.; Ahmad, M. M.; Taylor, S.; Tunstall, J. *J. Vac. Sci. Technol. A* **1999**, 17, 2300-2307.
59. Orient, O. J.; Chutjian, A.; Garkanian, V. *Rev. Sci. Instrum.* **1997**, 68, 1393-1397.
60. Syms, R. R. A.; Tate, T. J.; Ahmad, M. M.; Taylor, S. *Electron. Lett.* **1996**, 32, 2094-2095.
61. Sillon, N.; Baptist, R. *Sensor Actuat. B-Chem.* **2002**, 83, 129-137.
62. Taylor, S.; Tindall, R. F.; Syms, R. R. A. *J. Vac. Sci. Technol. B* **2001**, 19, 557-562.
63. Orient, O. J.; Chutjian, A.; Garkanian, V. *Rev. Sci. Instrum.* **1997**, 68, 1393-1397.
64. Ferran, R. J.; Boumsellek, S. *J. Vac. Sci. Technol. A* **1996**, 14, 1258-1265.
65. Stalder, R. E.; Boumsellek, S.; Zandt, T. R.; Kenny, T. W.; Hecht, M. H.; Grunthamer, F. E. *J. Vac. Sci. Technol.* **1994**, A12, 2554-2558.
66. Boumsellek, S.; Ferran, R. J. *J. Am. Soc. Mass Spectrom.* **2001**, 12, 633-640.
67. Prestage, J. D. *Nasa Tech Brief* **1999**, 23, 1-68.
68. Badman, E. R.; Cooks, R. G. *Anal. Chem.* **2000**, 72, 5079-5086.

69. Badman, E. R.; Cooks, R. G. *Anal. Chem.* **2000**, *72*, 3291-3297.
70. Badman, E. R.; Johnson, R. C.; Plass, W. R.; Cooks, R. G. *Anal. Chem.* **1998**, *70*, 4896-4901.
71. Kaiser, R. E.; Cooks, R. G.; Stafford, G. C.; Syka, J. E. P.; Hemberger, P. H. *Int. J. Mass Spectrom. Ion Processes* **1991**, *106*, 79-86.
72. Kornienko, O.; Reilly, P. T. A.; Whitten, W. B.; Ramsey, J. M. *Rapid Commun. Mass Spectrom.* **1999**, *13*, 50-53.
73. Kornienko, O.; Reilly, P. T. A.; Whitten, W. B.; Ramsey, J. M. *Rev. Sci. Instrum.* **1999**, *70*, 3907-3909.
74. Cornish, T. J.; Ecelberger, S.; Brinckerhoff, W. *Rapid Commun. Mass Spectrom.* **2000**, *14*, 2408-2411.
75. Cotter, R. J.; Fancher, C.; Cornish, T. J. *J. Mass Spectrom.* **1999**, *34*, 1368-1372.
76. Anderson, C. W.; Carlson, M. A. *Johns Hopkins APL Tech. Dig.* **1999**, *20*, 352-362.
77. Cornish, T. J.; Bryden, W. A. *Johns Hopkins APL Tech. Dig.* **1999**, *20*, 335-342.
78. McLoughlin, M. P.; Allmon, W. R.; Anderson, C. W.; Carlson, M. A.; DeCicco, D. J.; Evancich, N. H. *Johns Hopkins APL Tech. Dig.* **1999**, *20*, 326-334.
79. Cornish, T. J.; Cotter, R. J. *Anal. Chem.* **1997**, *69*, 4615-4618.
80. White, A. J.; Blamire, M. G.; Corlett, C. A.; Griffiths, B. W.; Martin, D. M.; Spencer, S. B.; Mullock, S. J. *Rev. Sci. Instrum.* **1998**, *69*, 565-571.
81. Matsuo, T.; Ishihara, M.; Toyoda, M.; Ito, H.; Yamaguchi, S.; Roll, R.; Rosenbauer, H. *Adv. Space Res.* **1999**, *23*, 341-348.
82. Sinha, M. P.; Langstaff, D. P.; Narayan, D.G.; Birkinshaw, K. *Int. J. Mass Spectrom.* **1998**, *176*, 99-102.
83. Sinha, M. P.; Tomassian, A.D. *Rev. Sci. Instrum.* **1991**, *62*, 2618-2620.
84. Sinha, M. P.; Gutnikov, G. *Anal. Chem.* **1991**, *63*, 2012-2016.
85. Burgoyne, T.W.; Hieftje, G. M.; Hites, R. A. *J. Am. Soc. Mass. Spectrom.* **1997**, *8*, 307-318.
86. Kogan, V. T.; Pavlov, A. K.; Chichagov, Y. V.; Tubol'tsev, Y. V.; Gladkov, G. Y.; Kazanskii, A. D.; Nikolaev, V. A.; Pavlichkova, R. *Field Anal. Chem. Technol.* **1997**, *1*, 331-342.
87. Tuszewski, M. *Rev. Sci. Instrum.* **1996**, *67*, 2215-2220.

88. Diaz, J. A.; Vargas, A. E. M.; Diaz, F. C.; Squire, J. P.; Jacobson, V.; McCaskill, G.; Rohrs, H.; Chhatwal, R. *Trend Anal. Chem.* **2002**, 21, 515-525.
89. Diaz, J. A.; Giese, C. F.; Gentry, W. R. *Field Anal. Chem. Tech.* **2001**, 5, 156-167.
90. Diaz, J. A.; Giese, C. F.; Gentry, W. R. *J. Am. Soc. Mass Spectrom.* **2001**, 12, 619-632.
91. Griffin, T.; *Preliminary Gas Detection Standard (Metrology and Procedures)*; Adams, R.; Breznik, G.; Helms, W., Eds.; Kennedy Space Center, FL, 2000; KSC-MM-4865.
92. Gonin, M.; Fuhrer, K.; Schultz, A. A New Concept to Increase Dynamic Range Using Multi-Anode Detectors. *Proceedings of the 48th ASMS Conference on Mass Spectrometry and Allied Topics*. Long beach, CA, 2000; pp 326-327.
93. Dehmelt, H. G.; Jefferts, K. B. *Phys. Rev.* **1962**, 125, 1318-1322.
94. Dehmel, H. G.; Major, F. G. *Phys. Rev. Lett.* **1962**, 8, 213-214.
95. Fulford, J. E.; March, R. E. *Int. J. Mass Spectrom. Ion Phys.* **1978**, 155-162.
96. Alheit, R.; Henning, C.; Morgenstern, R.; Vedel, F.; Werth, G. *Appl. Phys. B* **1995**, 61, 277-283.
97. Alheit, R.; Kleineidam, S.; Vedel, F.; Vedel, M.; Werth, G. *Int. J. Mass Spectrom. Ion Proc.* **1996**, 154, 155-169.
98. Alheit, R.; Chu, X. Z.; Hoefer, M.; Holzki, M.; Werth, G. *Phys. Rev. A* **1997**, 56, 4023-4031.
99. Dawson, P. H.; Whetten, N. R. *Air Force Cambridge Research Laboratories* **1969**, AFCRL-69-0185.
100. Dawson, P. H.; Whetten, N. R. *US Patent*, 1970, 3527939.
101. Schwartz, J. C.; Senko, M. W.; Syka, J. E. P. *J. Am. Soc. Mass Spectrom.* **2002**, 13, 659-669.
102. Sheretov, E. P.; Rozhkov, O. W.; Kiryushin, D. W.; Malutin, A. E. *Int. J. Mass Spectrom.* **1999**, 190/191, 103-111.
103. Kofel, P. Chapter 2 in *Practical Aspects of Ion Trap Mass Spectrometry*; March, R. E.; Todd, J. F. J., Eds.; CRC Press: Boca Raton, FL, 1995; Vol. 2, pp. 51-87.
104. Quarmby, S. T.; Yost, R. A. *Int. J. Mass Spectrom.* **1999**, 190/191, 81-102.
105. Appelhans, A. D.; Dahl, D. A. *Int. J. Mass Spectrom.* **2002**, 216, 269-284.

106. Quarmby, S. T.; Guckenberger, G. B. *Introduction to the PolarisQ*. Vender Expose Pittconn 2000, New Orleans, LA, March 12-17.
107. McHale, K. J. Ph.D. Dissertation, University of Florida, Gainesville, 2002.
108. Hirohata, Y.; Mutoh, A.; Hino, T.; Yamashina, T.; Kikuchi, T.; Ohsako, N. *Vacuum* **1996**, 47, 727-731.
109. Louris, J. N.; Taylor, D. M. *US Patent*, 1994, 5324939.
110. Harrison, A. G. Chapter 2 in *Chemical Ionization Mass Spectrometry*; CRC Press: Boca Raton, FL, 1992; pp. 7-47.
111. Liere, P.; Steiner, V.; Jennings, K. R.; March, R. E.; Tabet, J. C. *Int. J. Mass Spectrom. Ion Process.* **1997**, 167/168, 735-751.
112. Nourse, B. D.; Cooks, R. G. *Anal. Chim. Act.* **1990**, 228, 1-21.
113. Harrison, A. G. Chapter 1 in *Chemical Ionization Mass Spectrometry*; CRC Press: Boca Raton, FL, 1992; pp. 1-6.
114. Märk, T. D. Chapter 3 in *Gaseous Ion Chemistry and Mass Spectrometry*; Futrell, J. H., Ed.; Wiley-Interscience Publications: New York, NY, 1986; pp. 61-94.
115. Eckenrode, B. A.; McLuckey, S. A.; Glish, G. L. *Int. J. Mass Spectrom. Ion Process.* **1991**, 106, 137-157.
116. Weglein, A. B.; Rapp, D. Chapter 16 in *Gas Phase Ion Chemistry*; Bowers, M. T., Ed.; Academic Press: New York, NY, 1979; Vol. 2, pp. 300-342.
117. Harrison, A. G. Chapter 4 in *Chemical Ionization Mass Spectrometry*; CRC Press: Boca Raton, FL, 1992; pp. 71-112.
118. Lindholm, E. Chapter 1 in *Ion-Molecule Reactions in the Gas Phase*; Ausloos, P. J., Ed.; American Chemical Society: Washington, DC, 1966; pp. 1-19.
119. Lindholm, E. Chapter 10 in *Ion-Molecule Reactions*, Franklin, J. L., Ed.; Plenum Press: New York, NY, 1972; Vol. 2, pp. 457-484.
120. CRC Handbook of Chemistry and Physics: 71st Edition, Lide, D. R., Ed.; CRC press: Boca Raton, FL, 1990.
121. Aue, D. H.; Bowers, M. T. Chapter 9 in *Gas Phase Ion Chemistry*; Bowers, M. T., Ed.; Academic Press: New York, NY, 1979; Vol. 2, pp. 1-52.
122. Franklin, J. L.; Haney, M. A. Chapter 26 in *Ion-Molecule Reactions, Part II: Evaluated Pressures and Long Reaction Times*; Franklin, J. L., Ed.; Dowden, Hutchinson & Ross: Stroudsburg, PA, 1979; pp. 233-236.

123. de Gouw, J. A.; Ding, L. N.; Frost, M. J.; Kato, S.; Bierbaum, V. M.; Leone, S. R. *Chem. Phys. Lett.* **1995**, 240, 362-368.
124. Knott, W. J.; Proch, D.; Kompa, K. L.; Rose-Petruck, C. *J. Chem. Phys.* **1995**, 102, 214-225.
125. Snyder, E. M.; Castleman, A. W., Jr. *J. Chem. Phys.* **1997**, 107, 744-750.
126. Knott, W. J.; Proch, D.; Kompa, K. L. *J. Chem. Phys.* **1998**, 108, 527-533.
127. Hunter, E. J.; Homyak, A. R.; Ketkar, S. N. *J. Vac. Sci. Technol. A* **1998**, 16, 3127-3130.
128. Basic, C. Ph.D. Dissertation, University of Florida, Gainesville, 1992.
129. McLuckey, S. A.; Glish, G. L.; Asano, K. G.; Van Berkel, G. J. *Anal. Chem.* **1988**, 60, 2312-2314.
130. Ketkar, S. N.; Scott, A. D., Jr.; Hunter, E. J. *Int. J. Mass Spectrom.* **2001**, 206, 7-12.
131. Su, T.; Bowers, M. T. Chapter 3 in *Gas Phase Ion Chemistry*; Bowers, M. T., Ed.; Academic Press: New York, NY, 1979; Vol 1, pp. 83-118.
132. Lindinger, W. Chapter 11 in *Gaseous Ion Chemistry and Mass Spectrometry*; Futrell, J. H., Ed.; Wiley-Interscience: New York, NY, 1986; pp. 237-257.
133. Ikezoe, Y.; Matsuo, S.; Takebe, M.; Viggiano, A. *Gas Phase Ion-Molecule Reaction Rate Constants Through 1986*; Maruzen Company: Tokyo, Japan, 1987.
134. *Basic Vacuum Practice, Third Edition*; Varian Associates: Lexington, MA, 1992.
135. Pedder, R. E.; Johnson, J. V.; Yost, R. A. Electron Energy in a Quadrupole Ion Trap Mass Spectrometer. *Proceedings of the 40th ASMS Conference on Mass Spectrometry and Allied Topics*. Washington, DC, 1992; pp 1761-1762.
136. Pedder, R. E. Dissertation, University of Florida, Gainesville, 1992.
137. Vedel, F. *Int. J. Mass Spectrom. Ion Process.* **1991**, 106, 33-61.
138. Sevugarajan, S.; Menon, A. G. *Int. J. Mass Spectrom.* **2000**, 197, 263-278.
139. Cox, K. A.; Cleven, C. D.; Cooks, R. G. *Int. J. Mass Spectrom. Ion Process.* **1995**, 144, 47-65.
140. Lammert, S. A.; Plass, W. R.; Thompson, C. V.; Wise, M. B. *Int. J. Mass Spectrom.* **2001**, 212, 25-40.
141. Schwartz, J. C.; Senko, M. W.; Syka, J. E. P. *J. Am. Soc. Mass Spectrom.* **2002**, 13, 659-669.

142. Johnson, J. V.; Basic, C.; Pedder, R. E.; Kleintop, B. L.; Yost, R. A. Chapter 8 in *Practical Aspects of Ion Trap Mass Spectrometry*; March, R. E.; Todd, J. F. J., Eds.; CRC Press: Boca Raton, FL, 1995; Vol. 3, pp. 257-312.
143. Wehmeyer, K. R.; Knight, P. M.; Parry, R. C. *J Chrom. B* **1996**, 676, 53-59.
144. Tiller, P. R.; Cuniff, J. B.; Land, A. P. *Rapid Commun. Mass Spectrom.* **1997**, 11, 1151-1153.
145. Zemaitis, M. A.; Kroboth, P. D. *J. Chromatogr. B* **1998**, 716, 19-26.
146. Gaspari, M.; Guček, M.; Walhagen, K.; Vreeken, R. J.; Verheij, E. R.; Tjaden, U. R.; van der Greef, J. *J. Micro. Sep.* **2001**, 13, 243-249.
147. Syka, J. E. P.; Louris, J. N.; Kelley, P. E.; Stafford, G. C.; Reynolds, W. E. *U.S. Patent*, 1988, 4736101.
148. Johnson, J. V.; Yost, R. A.; Kelley, P. E.; Bradford, D. C. *Anal. Chem.* **1990**, 62, 2162-2172.
149. March, R. E.; Strife, R. J.; Creaser, C. S. Chapter 2 in *Practical Aspects of Ion Trap Mass Spectrometry*, March, R. E.; Todd, J. F. J., Eds.; CRC Press: Boca Raton, FL, 1995; Vol. 3, pp. 27-88.
150. Franklin, A. M.; Todd, J. F. J. Chapter 11 in *Practical Aspects of Ion Trap Mass Spectrometry*, March, R. E.; Todd, J. F. J., Eds.; CRC Press: Boca Raton, FL, 1995; Vol. 3, pp. 403-425.
151. Von Busch, F.; Paul, W. Z. *Phys.* **1961**, 164, 588-594.
152. Dawson, P. H.; Whetten, N. R. *Int. J. Mass Spectrom. Ion Phys.* **1969**, 2, 45-59.
153. Whetten, N. R.; Dawson, P. H. *J. Vac. Sci. Technol.* **1969**, 6, 100-103.
154. Franzen, J.; Gabling, R. H.; Schubert, M.; Wang, Y. Chapter 3 in *Practical Aspects of Ion Trap Mass Spectrometry*, March, R. E.; Todd, J. F. J., Eds.; CRC Press: Boca Raton, FL, 1995; Vol. 1, pp. 49-167.
155. Alheit, R.; Gudjons, Th.; Kleineidam, S.; Werth, G. *Rapid Commun. Mass Spectrom.* **1996**, 10, 585-590.
156. Eades, D. M.; Johnson, J. V.; Yost, R. A. *J. Am. Soc. Mass Spectrom.* **1993**, 4, 917-929.
157. March, R. E. *J. Mass Spectrom.* **1997**, 32, 352-369.
158. Cleven, C. D.; Cooks, R. G.; Garrett, A. W.; Nogar, N. S.; Hemberger, P. H. *J. Phys. Chem.* **1996**, 100, 40-46.

159. Peng, Y.; Plass, W. R.; Cooks, R. G. *J. Am. Soc. Mass Spectrom.* **2002**, 13, 623-629.
160. Sudakov, M. *Int. J. Mass Spectrom.* **2001**, 206, 27-43.
161. March, R. E. *Rapid Commun. Mass Spectrom.* **1998**, 12, 1543-1554.
162. Gill, L. A.; Wells, J. M.; Patterson, G. E.; Amy, J. W.; Cooks, R. G. *Anal. Chem.* **1998**, 70, 4448-4452.
163. Wells, J. M.; Plass, W. R.; Patterson, G. E.; Ouyang, Z.; Badman, E. R.; Cooks, R. G. *Anal. Chem.* **1999**, 71, 3405-3415.
164. Dawson, P. H.; Whetten, N. R. *J. Vac. Sci. Technol.* **1968**, 5, 1-10.
165. Dawson, P. H.; Whetten, N. R. *J. Vac. Sci. Technol.* **1968**, 5, 11-18.
166. Schwartz, J. C.; Syka, J. E. P.; Jardine, I. *J. Am. Soc. Mass Spectrom.* **1991**, 2, 198-204.
167. Schwartz, J. C.; Syka, J. E. P.; Louris, J. N. *U.S. Patent*, 1993, 5182451.
168. Williams, J. D.; Cox, K. A.; Schwartz, J. C.; Cooks, R. G. Chapter 1 in *Practical Aspects of Ion Trap Mass Spectrometry*, March, R. E.; Todd, J. F. J., Eds.; CRC Press: Boca Raton, FL, 1995; Vol. 2, pp. 3-47.
169. Creaser, C. S.; Mitchell, D. S.; O'Neill, K. E. *Int. J. Mass Spectrom. Ion Process.* **1991**, 106, 21-31.
170. Fies, W. J., Jr.; Kelley, P. E.; Reynolds, W. E.; Stafford, G. C., Jr.; Syka, J. E. P. *U.S. Patent*, 1987, 4650999.
171. Abbott, P. J. J.; Kendall, B. R. F.; Trout, K. P. *J. Vac. Sci. Technol. A* **1991**, 9, 1996-2000.
172. Basford, J. A. *J. Vac. Sci. Technol. A* **1991**, 9, 1991-1995.
173. Long, G. L.; Winefordner, J. D. *Anal. Chem.* **1983**, 55, 712A-724A.
174. Ottens, A. K.; Harrison, W. W.; Griffin, T. P.; Helms, W. R. *J. Am. Soc. Mass Spectrom.* **2002**, 13, 1120-1128.
175. Arkin, C. R.; Griffin, T. P.; Ottens, A. K.; Diaz, J. A.; Follistein, D. W.; Adams, F. W.; Helms, W. R. *J. Am. Soc. Mass Spectrom.* **2002**, 13, 1004-1012.
176. Alkemade, C. J.; Snelleman, W.; Boutilier, G. D.; Pollard, B. D.; Winefordner, J. D.; Chester, T. L.; Omenetto, N. *Spectrochim. Acta* **1978**, 33B, 383-399.
177. Casaro, F.; Levi, G. *J. Vac. Sci. Technol. A*, **1991**, 9, 1058-2061.

178. Reich, G. J. *Vac. Sci. Technol. A*, **1989**, 7, 2365-2368.
179. Kardok, P. The Issues Limiting Large-Scale Commercialization of Miniature Vacuum Systems. *The Second NASA/JPL Miniature Vacuum Pumps Workshop*, Pasadena, CA, March 25-28 2002.
180. Rowan, R.; Johnson, M. Miniature Turbo-Molecular Pump. *The Second NASA/JPL Miniature Vacuum Pumps Workshop*, Pasadena, CA, March 25-28 2002.
181. Kenton, M. Development of Turbomolecular Pumps for Demanding Environments. *The Second NASA/JPL Miniature Vacuum Pumps Workshop*, Pasadena, CA, March 25-28 2002.

BIOGRAPHICAL SKETCH

Andrew was born to Paul and Ann Ottens on March 23, 1976 in Edison, New Jersey. Early interests included mechanical construction, drawing and drafting, computers, and science, all of which he excelled at in Morris Knolls High School, where he also became interested in public speaking. Andrew, having an interest in scientific fields in general, completed all offered advanced science class. However, after graduating in 1994, he chose to major in chemistry at The College of New Jersey, because of the offered opportunities.

Andrew continued with his involvement in the arts, computers, and science while at college. He performed musically (training in voice and violin) and theatrically (as an actor and as a director). In 1997, he studied in France, later completed a minor in French studies. That same year, Andrew interned as a computer specialist at Public Service Electric and Gas Company of New Jersey, where he continued working until entering graduate school in the fall of 1998.

Andrew's undergraduate research involved analytical instrumentation, particularly mass spectrometry, which combined his interest in mechanics, computers, and science. His curiosity about mass spectrometry led him to the University of Florida where he began his doctoral studies in the analytical division. In May 2000, Andrew was accepted as an intern at NASA's Kennedy Space Center where he began working on ways to use mass spectrometry to improve the safety of Space Shuttle operations, forming the basis of his doctoral research.

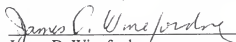
While at the University of Florida, he received the Linton E. Grinter Fellowship for exceptional graduate candidates and the Roger G. and Jo Bates Fellowship for outstanding progress in analytical chemistry. After completing his Ph.D. studies under the guidance of Dr. W. W. Harrison, Andrew will shift to the area of bioanalytical mass spectrometry as a postdoctoral fellow for the Center of Biotechnology at the University of Florida under the guidance of Dr. Nancy Denslow.

I certify that I have read this study and that in my opinion it conforms to acceptable standards of scholarly presentation and is fully adequate, in scope and quality, as a dissertation for the degree of Doctor of Philosophy.



Willard W. Harrison, Chairman
Professor of Chemistry

I certify that I have read this study and that in my opinion it conforms to acceptable standards of scholarly presentation and is fully adequate, in scope and quality, as a dissertation for the degree of Doctor of Philosophy.



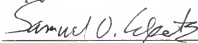
James D. Winefordner
Graduate Research Professor of
Chemistry

I certify that I have read this study and that in my opinion it conforms to acceptable standards of scholarly presentation and is fully adequate, in scope and quality, as a dissertation for the degree of Doctor of Philosophy.



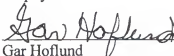
David H. Powell
Scientist of Chemistry

I certify that I have read this study and that in my opinion it conforms to acceptable standards of scholarly presentation and is fully adequate, in scope and quality, as a dissertation for the degree of Doctor of Philosophy.



Samuel O. Colgate
Professor of Chemistry

I certify that I have read this study and that in my opinion it conforms to acceptable standards of scholarly presentation and is fully adequate, in scope and quality, as a dissertation for the degree of Doctor of Philosophy.



Gar Hoflund
Professor of Chemical Engineering

This dissertation was submitted to the Graduate Faculty of the Department of Chemistry in the College of Liberal Arts and Sciences and to the Graduate School and was accepted as partial fulfillment of the requirements for the degree of Doctor of Philosophy.

May 2003

Dean, Graduate School

LD
1780
20 03

,089